UNIVERSIDAD DE CHILE
FACULTAD DE CIENCIAS FÍSICAS Y MATEMÁTICAS
DEPARTAMENTO DE INGENIERÍA ELÉCTRICA

TOWARDS BATTERY HEALTH MANAGEMENT FOR LITHIUM POLYMER BATTERY-POWERED SMALL-SIZE ROTARY-WING UNMANNED AERIAL VEHICLES

TESIS PARA OPTAR AL GRADO DE DOCTORA EN INGENIERÍA ELÉCTRICA

GINA KATHERINE SIERRA PÁEZ

PROFESOR GUÍA:
DR. MARCOS ORCHARD CONCHA

CO-GUÍA:
DR. KAI GOEBEL

MIEMBROS DE LA COMISIÓN:
DR. JORGE SILVA SÁNCHEZ
DR. FERNANDO AUAT CHEEIN
DR. EDUARDO CERPA JERIA

Este trabajo ha sido parcialmente financiado por CONICYT bajo la beca
CONICYT-PCHA/Doctorado Nacional/2014-63140178

SANTIAGO DE CHILE
2018

THESIS ABSTRACT FOR THE
DOCTORAL DEGREE IN ELECTRICAL ENGINEERING
BY: GINA KATHERINE SIERRA PÁEZ
DATE: 2018
SUPERVISOR: DR. MARCOS ORCHARD CONCHA
CO-SUPERVISOR: DR. KAI GOEBEL

TOWARDS BATTERY HEALTH MANAGEMENT FOR LITHIUM POLYMER BATTERY-POWERED SMALL-SIZE ROTARY-WING UNMANNED AERIAL VEHICLES

Little work has been done on Battery Health Management (BHM) for rotary-wing Unmanned Aerial Vehicles (UAVs) despite the fact that they have become increasingly popular. They are highly maneuverable and enable both safe and low-cost experimentation in mapping, navigation, and testing of control algorithms in three dimensions. Also, they can perform maneuvers that cannot be achieved by their fixed-wing counterparts (e.g., hover in place, and take off and land vertically (VTOL)). However, small-size aircraft typically have weight, size and cost constraints. Thus, as small-size UAVs become more prevalent, the need for computationally efficient software will increase.

This thesis proposes a holistic framework for the design, implementation and experimental validation of Battery Health Management (BHM) systems in small-size rotatory-wing Unmanned Aerial Vehicles (UAVs) that allows to accurately (i) estimate the State of Charge (SOC), and (ii) predict the End of Discharge (EOD) time of lithium-polymer batteries in small-size multirotors by using a model-based prognosis architecture that is efficient and feasible to implement in low-cost hardware. The proposed framework includes a simplified battery model that incorporate the electric load dependence, temperature dependence and SOC dependence by using the concept of Artificial Evolution to estimate some of its parameters, along with a novel Outer Feedback Correction Loop (OFCL) during the estimation stage which adjusts the variance of the process noise to diminish bias in Bayesian state estimation and helps to compensate problems associated with incorrect initial conditions in a non-observable dynamic system. Also, it provides an aerodynamic-based characterization of future power consumption profiles and utilizes a new definition of probability of failure to mitigate the risk. A quadrotor has been used as validation platform. This thesis is the first research effort towards BHM for small-size rotary-wing UAVs validated beyond numerical simulations, and that addresses the problem from an efficient approach for constrained computing platforms.

A proper prognosis of the EOD time is not only necessary to verify if the mission goal(s) can be accomplished but also essential to aid in online decision-making activities such as fault mitigation and mission replanning. Therefore, the results of this work will allow making decisions about the flight and having enough confidence in those decisions so that the mission objectives can be optimally achieved. Given that: (*i*) the flight times in battery-powered UAVs are indeed short, (*ii*) most flight plans are highly conservatives due to they suffer from uncertainties in estimating the remaining charge, (*iii*) applications in urban zones are limited due to the risk associated with accidental battery run-down during the flight, and (*iv*) UAVs are ideally suited for long endurance applications; it hopes the results of this research become a significant contribution to the battery-powered rotary-wing UAVs field.

RESUMEN DE TESIS PARA OPTAR AL TÍTULO
DE DOCTORA EN INGENIERÍA ELÉCTRICA
POR: GINA KATHERINE SIERRA PÁEZ
FECHA: 2018
PROF. GUÍA: DR. MARCOS ORCHARD CONCHA
CO-GUÍA: DR. KAI GOEBEL

HACIA LA GESTIÓN DE LA SALUD DE LA BATERÍA PARA VEHÍCULOS AÉREOS NO TRIPULADOS DE ALA ROTATORIA Y PEQUEÑA ESCALA CON BATERÍAS DE POLÍMERO DE LITIO COMO FUENTE DE ALIMENTACIÓN PRIMARIA

Se ha trabajado poco en gestión de la salud de las baterías (BHM del Inglés Battery Health Management) para vehículos aéreos no tripulados (UAV del inglés Unmanned Aerial Vehicle) de alas rotatorias, a pesar de que son los más populares porque son altamente maniobrables y permiten una experimentación segura y de bajo costo en mapeo, navegación y algoritmos de control en tres dimensiones. Además, pueden realizar maniobras que no se pueden lograr con sus contrapartes de ala fija (por ejemplo, flotar en su lugar, despegar y aterrizar verticalmente (VTOL de inglés Vertical Take-Off and Landing)). Sin embargo, los aviones de pequeña escala generalmente tienen limitaciones de peso, tamaño y costo. Por lo tanto, a medida que los vehículos aéreos no tripulados de pequeña escala prevalezcan, aumentará la necesidad de software computacionalmente eficiente.

Esta tesis propone un marco holístico para el diseño, implementación y validación experimental de sistemas de gestión de la salud de las bateras (BHM) en vehículos areos no tripulados (UAV) de ala rotatoria de pequeña escala que permite (i) estimar con precisin el estado de carga (SOC del inglés State of Charge) y (ii) predecir el tiempo de fin de descarga (EOD del inglés End of Discharge) de las baterías de polímero de litio en multirotores de pequeña escala mediante el uso de una arquitectura de pronóstico basada en modelo que es eficiente y factible de implementar en hardware de bajo costo. El marco propuesto incluye un modelo de batería simplificado que incorpora la dependencia de la carga eléctrica, la dependencia de la temperatura y la dependencia del SOC mediante el uso del concepto de Evolución Artificial para estimar algunos de sus parámetros, junto con un novedoso lazo de corrección de retroalimentación exterior (OFCL del Inglés Outer Feedback Correction Loop) durante la etapa de estimación que ajusta la varianza del ruido del proceso para disminuir el sesgo en la estimación del estado bayesiano y ayuda a compensar los problemas asociados con condiciones iniciales incorrectas en un sistema dinámico no observable. Además, proporciona una caracterización aerodinámica de los perfiles de consumo de energía en el futuro y utiliza una nueva definición de probabilidad de falla para mitigar el riesgo. Un cuadrotor ha sido utilizado como plataforma de validación. Esta tesis es el primer esfuerzo de investigación hacia BHM para vehículos aéreos no tripulados de ala rotativa de pequeña escala, validado más allá de las simulaciones numéricas y que aborda el problema desde un enfoque eficiente para plataformas de computación restringidas.

Un pronóstico adecuado del tiempo de EOD no sólo es necesario para verificar si se pueden cumplir los objetivos de la misión, sino también para ayudar en las actividades de toma de decisiones en línea, como mitigación de fallas, re-planificación de misiones, etc. Por lo tanto, los resultados de este trabajo permitirán tomar decisiones sobre el vuelo y tener

suficiente confianza en esas decisiones para que los objetivos de la misión se puedan alcanzar de manera óptima. Dado que: (*i*) los tiempos de vuelo en vehculos aéreos no tripulados de batería son cortos, (*ii*) la mayoría de los planes de vuelo son muy conservadores debido a sufren incertidumbres al estimar la carga restante, (*iii*) las aplicaciones en zonas urbanas son limitadas debido al riesgo asociado con el agotamiento accidental de la batería durante el vuelo, y (*iv*) los UAV son ideales para aplicaciones de larga duración, se espera que los resultados de esta investigación se conviertan en una contribución significativa al campo de vehículos aéreos no tripulados de ala giratoria a batería.

Acknowledgements

Firstly, I would like to express my sincere gratitude to my advisor, Prof. Marcos Orchard, for giving me the opportunity of working with him, for his supervision, and especially for allowing to develop myself scientifically during these years working together.

I have also greatly appreciated and benefited from the cooperation with and the feedback from researchers from the Prognostics Center of Excellence (PCoE) at NASA Ames Research Center. In particular, I thank Dr. Kai Goebel and Dr. Chetan Kulkarni for their cooperation, their feedback, and for giving me the opportunity to work with them in their research group as a visiting scientist.

Last but not the least, I would like to thank my family: my parents and to my sisters for supporting me spiritually throughout writing this thesis and my my life in general.

Contents

List of Tables

List of Figures

List of Algorithms

Acronyms

BHM	Battery Health Management.
EKF	Extended Kalman Filter.
EOD	End of Discharge.
ESC	Electric Speed Controller.
HIL	Hardware-In-the-Loop.
JITP	Just-In-Time Point.
KF	Kalman Filtering.
MC	Monte Carlo.
OCV	Open Circuit Voltage.
OFCL	Outer Feedback Correction Loop.
PDF	Probability Density Function.
PF	Particle Filter.
PMF	Probability Mass Function.
PoF	Probability of Failure.
RUL	Remaining Useful Life.
SMC	Sequential Monte Carlo.
SOC	State of Health.
SOH	State of Charge.
UAV	Unmanned Aerial Vehicle.
UKF	Unscented Kalman Filtering.
VTOL	Vertical Take-Off and Landing.
WP	WayPoint.

Notations

E_{crit}	Maximum nominal energy delivered by the energy storage device.
$v_{oc}(k)$	Open circuit voltage at time k.
Z_p	Internal battery impedance.
Δt	Sampling time, measured in seconds.
D_{k+p}	Square root of the empirical covariance matrix for predicted state vector at $k+p$.
η	Measurement noise.
$q(\tilde{x}_{0:k}\|x_{0:k-1})$	Importance sampling distribution for state vector transition in time.
$\mathrm{i}(k)$	Battery discharge current, measured in amperes at time k.
$K(\cdot)$	Kernel density function.
$\pi_k(x_{0:k})$	True state vector probability density function.
φ^k	π_k-integrable function.
$p(x_{0:k}\|y_{1:k})$	Posterior density function of the state vector, conditional to noisy measurements.
v_o	Open circuit voltage when the battery is fully charged.
$v(k)$	Battery voltage, measured in volts at time k.
w_1	Process noise (state transition equation).
w_2	Process noise (state transition equation).
$w_k^{(\mathrm{i})}$	Weight associated with the ith particle at time k.
$x_{0:k}^{(\mathrm{i})}$	Realization of the state vector trajectory, associated with the ith particle at time time k.
$x_1(k)$	Internal impedance estimate at time k.
$x_2(k)$	State of charge estimate at time k.
$y_{1:k}$	Measurements collected up to time k.

Chapter 1

Introduction

This chapter states the problem that leads to the research question addressed in this thesis. Then it is sketched out how the thesis is structured to answer the research question, and lastly, the contributions from the development of this thesis are summarized. In Section 1.1 the problem and the research question are introduced. The objectives of this study are established in Section 1.2 and the hypotheses in Section 1.3. Finally, Section 1.4 presents the thesis outline and the main contributions.

1.1 Statement of the Problem

Unmanned Aerial Vehicles (UAVs) have received much attention in recent years due to their wide range of military and civilian applications since they can perform complex missions without human intervention.

UAVs, also known as "drones", refers to aircraft without a pilot on board, although it can be steered by remote control. By its wing type, UAVs can be categorized into the following types: fixed-wing, rotary-wing, and flapping-wing. Multicopters, a type of rotary-wing aircraft with at least three independent rotors and propellers, have recently emerged as the platform of choice for research in micro aerial vehicles since they are mechanically simple, highly maneuverable and enable safe and low-cost experimentation in mapping, navigation, and control algorithms in three dimensions. Besides, they can hover in place, and take off and land vertically, unlike their fixed-wing counterparts (Valavanis and Vachtsevanos, 2015a).

UAVs have been considered for a broad range of applications that include but are not limited to power line inspection; pipeline inspection; ship inspection; mine inspection; dam inspection; anomaly detection/prevention; early fire detection and forest protection; hazard monitoring; traffic monitoring; environmental monitoring; search and rescue operations; emergency response; border patrol; harbor patrol; police surveillance; aerial photography; SWAT support; imaging and mapping; intelligence, surveillance, and reconnaissance (ISR); chemical spraying; crop dusting; night vision; and entertainment industry and filming (Valavanis and Vachtsevanos, 2015b; Asari, 2014; Diaz, 2015; Martinez, 2015; Amazon, Inc, 2015;

Editec, 2015).

Since the flight endurance is in direct relationship to the total weight of the craft, Lithium Polymer (Li-Po) batteries are usually used as the primary power source on account of its high-density energy. Li-Po batteries do not need any metal for its construction, which reduces the weight and increases the energy density of Li-Po batteries to over 20% higher than that of the traditional Li-ion batteries (Meyer et al., 2009).

Nevertheless, applications in urban areas are currently limited by the local regulations. These rules are stringent because a catastrophe can occur as the result of obstacle avoidance system failures, propulsion system failures, or power system failures (e.g., battery charge depletion). This situation is more dangerous when occurs in urban areas since people could be seriously injured.

As a representative example of this latter, Amazon is making their future delivery system, called *Prime Air*. This system is designed to deliver packages safely to customers in 30 minutes or less using small unmanned aerial vehicles (Amazon, Inc, 2015); however, the rules of the Federal Aviation Administration (FAA) only allow drones to fly within the user's line of sight. In this regard, Amazon expressed its disagreement with this restriction and has said: *"Putting Prime Air into service will take some time, but we will deploy when we have the regulatory support needed to realize our vision."* (Stelter, 2015).

On the other hand, UAVs are ideally suited for long endurance applications; however, in most cases, battery-powered UAVs have flight times short even when the battery capacity is optimal (Gatti et al., 2015). Moreover, battery-powered UAVs experience problems and risks associated with the use of batteries as the primary Energy Storage Devices (ESD). Namely, aging effects and abuse. The battery capacity decreases over time and use. Factors such as the room temperature of storage and usage, the State of Charge (SOC) in which the battery is stored, the discharge rate, overcharges or over-discharges affect its capacity (Mikolajczak et al., 2011). Also, battery performance is strongly determined by characteristics such as the current discharge rate, depth of discharge, or the internal temperature.

To use the energy stored in the batteries in a better way and to provide real-time diagnosis information for the benefit of the operator of the craft, a Battery Health Management (BHM) system becomes necessary. BHM systems are mainly aimed at reducing battery charging times, maximizing the number of operating cycles, maximizing the usage time associated with the discharge cycle, maintaining the operation of all cells within their rated limits, and compensate for cell imbalance, among others. BHM systems have to use information about the battery's SOC and its Remaining Useful Life (RUL) to accomplish these tasks (Pola et al., 2015). The knowledge of these state variables is not only necessary to verify if the mission goal(s) can be achieved but also essential to aid in online decision-making activities such as fault mitigation and mission replanning.

State of Charge (SOC) estimation and prognostic strategies are fundamental for the characterization of the End of Discharge (EOD) time. However, as in many other state estimation problems, the SOC is not observable; namely, it can not be directly measured, and it has to be inferred from indirect but statistically related measurements (e.g., battery voltage, discharge current, or temperature) (Pola et al., 2015). Furthermore, since it is not known the

real value of the SOC with complete certainty, battery-powered electric UAVs suffer from uncertainties in estimating the remaining charge, and therefore most flight plans are highly conservative, which means flight times are even shorter than what the battery capacity can reach.

The development of BHM systems for battery-powered electric UAVs has focused on Bayesian-based tools (Saha et al., 2011b, 2012; Cuong et al., 2013; Bole et al., 2014a; de Souza Candido et al., 2014; Hogge et al., 2015) due to they have achieved better results in estimation and prognosis problems. Unlike other methods, Bayesian-based methods can adjust the SOC in real time for different load conditions, (Chang, 2013) and they can assess the estimate's confidence by a Probability Density Function (PDF) (Goebel et al., 2008). Besides, along with the concept of *artificial evolution* provides the mechanism for generating new parameter (e.g., battery internal impedance) values at each time step, which has proved to be efficient because it incorporates the effect of environmental factors (e.g., temperature, or battery degradation and age). The implementation of this concept is by extending the dimension of the state vector (Liu and West, 2001; Orchard and Vachtsevanos, 2009).

In (Saha et al., 2011b, 2012; de Souza Candido et al., 2014), authors have carried out SOC estimation and EOD time prognosis based on Particle Filter (PF). In contrast, (Cuong et al., 2013; Bole et al., 2014a; Hogge et al., 2015) used Unscented Kalman Filter (UKF) for the same purpose. Both methods gave satisfactory results; however, PF is emerging as the preferred method because it appears to exhibit somewhat better performance than UKF (Walker et al., 2015).

To use Bayesian estimation techniques, the relationship between SOC and other measurable units, such as voltage, current or temperature, should be first established. Namely, a battery model as a function of SOC should be used. In particular, under Bayesian-based BHM framework for UAVs, battery models in a high level of granularity have been explored and evaluated regarding their performance in the estimation and prognosis process. The results showed that higher granularity and lower levels of abstraction might give more accurate predictions, but that also results in larger parameter sets which may not have good convergence properties if included in the state vector (Saha et al., 2011b). For such models, it is necessary to estimate most of the parameters from training data and choose just a few for online adaptation to avoid convergence difficulties.

In the case of prognosis, in addition to the battery model, the future consumption profile has to be defined because the amount of useful remaining charge depends not only on the initial SOC but also on other factors such as the state of health and the profile of charge or discharge. A proper future load profile characterization leads to EOD predictions more accurate and more stable as well (Cuong et al., 2013). As for an electric car, the future consumption of energy can be inferred from the flight plan, namely, from the length and speed of the aircraft in each stage of the flight (e.g., climb, descent and forward flight). Besides, any factor that affects engine and rotor efficiency affects aircraft performance and power consumption. The three broad factors that affect performance are density altitude (air density regarding altitude, pressure and, temperature), weight, and wind direction and velocity (Federal Aviation Administration, 2013). The air becomes thinner with altitude and heat, which significantly reduces the propellers ability to generate lift.

In (Saha et al., 2011b), the future consumption is outlined in two ways: (*i*) assuming the mean current of a typical flight and (*ii*) assuming that the consumption during flight path is fully known. The latter threw more accurate and precise predictions, although it is an idealist scenario since in practice the future consumption is subject to the uncertainty associated with environmental conditions, such as the wind speed and wind direction.

In (Saha et al., 2012), Gaussian kernels for each maneuver are adjusted from flight data. In (Cuong et al., 2013), the future consumption is based on the knowledge of a flight plan previously defined. The current mean is determined for each flight stage, and its uncertainty is characterized as a uniform distribution around ±30% of the mean. In (Bole et al., 2014a), the future power consumption is modeled for each type of maneuver based on aerodynamic equations. In this case, instead of defining a current mean, the aerodynamic model is used for estimate the future load in each stage of the flight plan. Also, an upper and lower limit around ±30% of the expected load represent the uncertainty in the prediction of the future consumption.

In brief, the future load profile characterization has been addressed by establishing a mean current for each flight maneuver based on either historical data of typical flights (Saha et al., 2011b) or aerodynamic models (Bole et al., 2014a). A PDF is defined around the current mean to characterize the uncertainty associated with unmodeled phenomena (e.g., temperature) (Saha et al., 2012; Cuong et al., 2013).

All studies mentioned above are aimed at fixed-wing UAVs except for (de Souza Candido et al., 2014) which is aimed at rotary-wing UAVs, although it is limited to numerical simulations and does not provide details about future consumption profiles used during the prediction. Also, the model used for the DC motors of the multirotor is insufficient to represent the energy consumption accurately during the different stages of flight since it only characterizes the torque experienced by the motors in hovering flight without considering the stages of climb, descent and forward flight. The torque on the motors for each one of these stages is different and thus the power consumption as well. During most of the path, the multirotor is in forward flight. Hence, presuming that the multirotor is in hovering during the full path is inaccurate and might cause a bias in the estimation of the remaining flight time.

Although multirotors are the most popular and used in diverse applications, little work has been done concerning the BHM for rotary-wing UAVs. Since rotary-wing and fixed-wing aerodynamics are different, their performances and power consumptions in each flight maneuver are different as well. Therefore, BHM systems for rotary-wing UAVs should consider the characterization of the power consumption in rotary-wing aircraft to properly define the future load profiles used in prognostic.

Also, small-size aircraft usually have weight, size and cost constraints. Consequently, as small-size UAVs become more prevalent, the need for computationally efficient software will increase. The improvement of efficiency in software for drones and mobile devices is arising as a new research topic as companies explore the use of drones for delivering and other complex tasks (Banerjee and Roychoudhury, 2017). Therefore, there is an emerging need to accurately (i) estimate the State of Charge (SOC), and (ii) predict the End of Discharge (EOD) time of Li-Po batteries in small-size multirotors that can operate in constrained environments.

There are not research efforts about BHM for small-size rotary-wing UAVs validated beyond numerical simulations. This latter along with the difficulties and constraints presented by small-size multirotors, leads to the question that aims to resolve this work: *Is it possible to accurately and efficiently characterize the risk of the mission concerning battery energy remaining in small-size multirotors?*

1.2 Objetives

1.2.1 Main Objective

To develop a Bayesian framework to probabilistically characterize the risk of the mission associated with the remaining battery energy in small-size electric multirotors.

1.2.2 Specific Objectives

1. To develop and evaluate a battery model suitable for battery SOC estimation and EOD time prediction in small-size electric multirotors.
2. To develop and evaluate estimation and prognosis algorithms suitable for battery SOC estimation and EOD time predictions in small-size electric multirotors.
3. To establish and validate a model for the generation of future discharge profiles of an electric multirotor given a flight plan under moderate wind conditions.
4. To validate the proposed solutions through SOC estimation and EOD time predictions for Li-Po battery discharge cycles of a small-size multirotor.
5. To assess prediction results in terms of EOD expectations, the Just-In-Time Point value, and the $\alpha - \lambda$ metric.

1.3 Hypotheses

In the case of small-size electric multirotors under moderate wind conditions and assuming that the battery state of health is assessed periodically, the following hypotheses are established:

1. The development of an equivalent circuit battery model that simplifies the structure of the observation equation by Pola et al. (2015), and use the concept of artificial evolution to estimate some of its parameters, may allow improving the efficiency in battery prognostic concerning other battery models used for prognostic.
2. A particle filter-based estimation and prognosis algorithm more sophisticated; namely, an algorithm that enhances the effectiveness of filtering stage by a novel Outer Feedback Correction Loop (OFCL), may allow performing more accurate EOD time predictions regarding a particle filter-based estimation and prognosis framework without OFCL.

3. It is proposed that the determination of an aerodynamic-based model that approximately characterizes the future power consumption for each flight stage may provide an improvement to the accuracy and precision of the EOD time prediction regarding other methods to characterize the future power consumption, such as the use of the equation for the power required in hovering flight.
4. It is proposed that the use of the definition of Probability of Failure (PoF) by Acuña and Orchard (2017) applied to EOD time prognostics in UAVs may provide EOD time characterizations more conservatives when the uncertainty involved in the mission is higher, which might mitigate the risk of suffering a catastrophe since the predicted EOD time is used as a basis for making decisions about the flight plan and ensure that the mission ends before the actual EOD time.

1.4 Overview of this Thesis

1.4.1 Thesis Outline

The remaining of this thesis is organized as follows:

- In Chapter 2, the state of art related to BHM for rotary-wing electric UAVs is presented. With this purpose:
  1. A literature review about BHM for electric UAVs and rotary-wing electric UAV is made. From this literature review, BHM for rotary-wing UAVs arose as a little-explored research topic. Also, there were identified the main components of the problem that affects the accuracy of the EOD prediction results, namely, battery model, estimation and prognosis algorithms, and future power consumption profiles.
  2. Considering the above, a review about models and SOC estimation and prognosis methods for batteries was made.
  3. Also, in order to identify the main factors that affect the power consumption on rotary-wing electric UAVs, considerations on the performance of electric multirotors were reviewed.

  From this literature review, there were identified the most relevant factors and insights to address the problem we are dealing with here. The above allowed outlining the prognostics framework described in Chapter 3.
- In Chapter 3, a proposed prognostic framework for BHM systems in small-size electric multirotor is presented. Aiming this goal:
  1. It is described the model-based prognostics architecture which has been adopted as the base for the development of this study.
  2. Then, considering the literature review in Chapter 2, each of the proposed adjustments to the prognostics architecture are described in detail, that is:
     - A simplified battery model that allows improving efficiency in prognostics.
     - A novel Outer Feedback Correction Loop that diminishes bias in recursive

Bayesian estimation, and thus allows performing more accurate EOD time predictions.

- A practical aerodynamic-based model to characterize the future power consumption profiles used during the prediction stage, which lead to predictions more accurate and stable.
- The use of the definition of probability of failure by Acuña and Orchard (2017) as a method to mitigate the risk of the mission.

Altogether, these proposals aim to reduce computational resources without losing accuracy in prognostics results. It is also intended to incorporate the risk involved in the mission into the prognosis results to mitigate the risk of a catastrophe.

- In Chapter 4, delivery missions are presented as a case study. In this Chapter:
  1. The proposed prognostic framework was used to estimate the SOC and predict the EOD time of a 3S 5100mAh Li-Po battery used by a 3DR IRIS+ quadcopter that performs delivery missions.
  2. To validate hypothesis 1, average estimation and prediction processing times using the simplified battery model and an electrochemistry-based model were measured and compared.
  3. To validate hypothesis 2, SOC estimation and EOD predictions were performed without the novel OFCL and with the novel OFCL. Results were evaluated and discussed.
  4. To validate hypothesis 3, SOC estimation and EOD predictions were performed without and with the use of the proposed aerodynamic-based model for the generation of future power consumption profiles. Results were evaluated and discussed.
  5. To validate hypothesis 4, the probability of failure was computed using the conventional definition and the definition by Acuña and Orchard (2017) for different levels of uncertainty on future power consumption profiles. Results were evaluated and discussed.
- Finally, Chapter 5 gathers the concluding remarks and future work.

1.4.2 Main Contributions

From the development of this thesis the following contributions have been made:

1. A simplified equivalent circuit battery model that allows improving efficiency in prognostics. Such improvement of efficiency constitutes an advantage when it deals with constrained processing power that may encounter on small UAVs. In particular:
   - This simplified battery model is an empirical state-space model, inspired by the battery phenomenology which allows the implementation of Bayesian filtering methods that efficiently estimates the SOC and predicts the EOD in real-time.
   - Regarding previous research efforts (Pola et al., 2015), the model offers a simplification to the observation equation that incorporates an improved version of the OCV curve for batteries of more than one cell. Also, it includes most of the nonlinearities found in Li-ion open-voltage discharge curves, while simultane-

ously reduce computational resources and enabling the implementation of reliable off-line estimation procedures for the estimation of all of its parameters.

- Also, the model takes advantage of the artificial evolution concept as mechanism for generating new values at each step time of the battery internal resistance and the total energy delivered by the battery, which has proved to be efficient because it incorporates battery performance dependencies (e.g., electric load dependence, temperature dependence, and SOC dependence).

2. A novel Outer Feedback Correction Loop (OFCL) during the estimation stage that adjusts the variance of the process noise to diminish the bias in Bayesian state estimation which allows providing more accurate EOD time predictions. In particular:
   - This proposed OFCL is based on long-term results, but unlike previous OFCLs (Tampier et al., 2015), it implements a basic digital filter on the observation error instead of using the accumulated error to determine whether to increase or decrease the variance of the process noise.
   - This OFCL does not require additional memory space, nor a minimum time to start operating.
   - This OFCL avoids falling into unnecessary increases of the standard deviation of the process noise and overreacting to large instantaneous observation errors.
   - With this OFCL, the more extended the period where the observation error is above the threshold, the higher the increase in the process noise. This latter seeks that the effective increase of the deviation is sufficient to ensure convergence.
   - Finally, with the proposed OFCL, its decision threshold can be defined to be equal to or less than the standard deviation of the observation noise.
3. An aerodynamic-based model of the power consumption in multirotors is proposed and validated to define future power consumption profiles used during the prediction stage and provide improved prediction results. In particular:
   - Unlike previous works (Gatti et al., 2015) that addressing the flight time estimation problem assuming that the aircraft is in hovering flight condition during the entire flight, the proposed model characterizes the power consumption in each stage of flight, that is, climb, hovering, horizontal flight and descent.
   - This power consumption model is an approximate model that provides a practical way to calculate the required power consumption for a flight plan previously known as a function of the weight, disc actuator area, air density, translational speed and the type of maneuver.
   - This aerodynamic-based model allows defining the future power profiles without the need to use a significant amount of flight data or flight simulations which are not always available.
4. The use of the definition of probability of failure by Acuña and Orchard (2017) applied to EOD time prognostics is proposed as a method to mitigate the risk of suffering a catastrophe. In particular:
   - Although the new PoF definition and its foundation were recently reported in (Acuña and Orchard, 2017), its effects on prediction results have not been evaluated nor incorporated as a method to mitigate the risk in the context of battery prognostic for UAVs. Therefore, this thesis evaluates the impact on prediction results of the use of the new definition of PoF regarding the conventional definition.

- In light of results of the above evaluation, using the new definition of PoF, the EOD Probability Mass Function (PMF) experiences a shift to the left (i.e., to an earlier time) that is related to the uncertainty in the prediction. The higher the uncertainty on the predicted EOD, the larger the shift to the left. Namely, EOD characterization is more conservative when the risk is higher. Therefore, taking advantage of the effects of the new PoF on prediction results, this thesis proposes the use of the new expression for the computation of the PoF as a method to incorporate the risk involved in the mission into the prognosis results.

Chapter 2

State of the Art

2.1 Introduction

This chapter presents and identifies the important features of the most recent works related to the research question of this thesis. Among them, approaches that addressed the BHM problem for electric UAVs and in particular for rotary-wing electric UAVs, and SOC estimation and prognosis methods for batteries. Section 2.2 introduces the concept of UAV, its categorizations, and applications. Section 2.3 describes previous works on BHM for electric UAVs and rotary-wing electric UAVs. Also, considerations of the performance of rotary-wing UAVs are presented in this section. In Section 2.4, a review of the methods for SOC estimation and prognosis for batteries is made. In the context of Bayesian methods, some battery models for prognosis, and other techniques such as artificial evolution an Outer Feedback Correction Loops are described. Section 2.5 describes Particle Filter algorithm and a Particle-filtering-based prognosis scheme. Finally, Section 2.6 presents a summary of the most important contents included in this chapter.

2.2 UAV Definition and Applications

An Unmanned Aerial Vehicle (UAV), also known as "drone", refers to an aircraft without pilot or human passengers on board. As such, "unmanned" means the total absence of a human on board that pilots the aircraft. However, it can be piloted remotely by a human being. The control functions of the UAVs can be on board or outside the vehicle (remote control) (Dalamagkidis, 2015). Current Unmanned Aerial Vehicles are in general remote controlled while some can fly autonomously based on pre-programmed flight plans.

An aerial robot is the ultimate of Unmanned Aerial Vehicles. Aerial robots are unmanned aerial vehicles capable of performing complex missions without human intervention. The field of aerial robotics is a field in constant evolution and expansion, experiencing remarkable progress in the last decade due to technological advances. Aerial robots often mimic existing

(a) (b) (c)

Figure 2.1: Categorization of the UAVs. (a) fixed-wing (b) rotary-wing and (c) flapping-wing

airborne vehicles such as airplanes, helicopters, and airships, or natural airborne animals such as birds or insects. Thus, aerial robots may be categorized into different types: fixed, rotary and flapping wing vehicle (Sebbane, 2014). See Fig.2.1.

Multirotors, a type of rotary-wing UAV, are the most popular since they are mechanically simple, highly maneuverable and enable safe and low-cost experimentation, navigation, and control algorithms in three dimensions. Besides, they can hover in place, and take off and land vertically, unlike their fixed-wing counterparts. Multirotors have at least three independent rotors and propellers; although the number of rotors generally ranges from four to eight, depending on the load to be carried and the amount of redundancy desired. A small computer onboard controls the power distribution to the different rotors, that is the way in which most multirotors are directed through the air (Valavanis and Vachtsevanos, 2015a).

Thanks to their versatility, flexibility, easy installation and relatively small expenses, usage of UAVs promise new ways for both military and civilian reconnaissance and surveillance applications. For the last two decades, in military areas, UAVs are being used for real-time surveillance, reconnaissance, intelligence, and warfare operations. On the other hand, for civilian areas, UAVs are well suited for situations that are too harsh or dangerous for direct human monitoring (Asari, 2014).

UAVs have been considered for a wide range of applications that include but are not limited to power line inspection; pipeline inspection; ship inspection; mine inspection; dam inspection; anomaly detection/prevention; early fire detection and forest protection; hazard monitoring; traffic monitoring; environmental monitoring; search and rescue operations; emergency response; border patrol; harbor patrol; police surveillance; aerial photography; SWAT support; imaging and mapping; intelligence, surveillance, and reconnaissance (ISR); chemical spraying; crop dusting; night vision; and entertainment industry and filming (Valavanis and Vachtsevanos, 2015b; Asari, 2014; Diaz, 2015; Martinez, 2015; Editec, 2015).

Already in Europe, green-power producers fly drones to inspect the blades of wind turbines, farmers use them to survey crops, and oil companies inspect their installations with them. One U.K. company has even used a drone of this kind for close inspection of a tower used to burn off combustible gaseseven as the flames rose just meters away (Diaz, 2015).

The latest addition to the drones line of the DJI company is designed for the agricultural sector. The powerful propulsion system enables an octocopter to carry up to 10kg of liquid payloads, including pesticide and fertilizer. The combination of speed and power means that

an area of $4,000 - 6,000m^2$ can be covered in just 10 minutes, or 40 to 60 times faster than manual spraying operations (Martinez, 2015).

Likewise, Google and Amazon are making their future delivery system designed to safely get packages to customers in 30 minutes or less using small unmanned aerial vehicles. Amazon recently presented what could be the final design of its delivery drone. This can deliver a package of up to 2 kg weight in half an hour or less, flying at an altitude of 120 meters with a range of about 15 km (Amazon, Inc, 2015).

On a larger scale and for other purposes, Google and Facebook also evaluate the use of drones to connect areas that lack the infrastructure to offer the Internet. To do this, Google acquired Titan Aerospace, a maker of UAVs; an operation that was also replicated by Facebook with the purchase of the firm Ascenta.

At a more local level, in Chile, besides to use drones in the mining sector, the government recently decided to toughen the fight against water theft by incorporating UAVs that will strengthen the work of monitoring complaints in natural riverbeds and so, support the work of inspection, construction and approval of hydraulic works (Editec, 2015). Chile also presented the first regulations for civil use of drones in Latin America. The regulations specify the places where the drones can fly and prohibits that they are to less than two kilometers of airports or airfields, and forbidden areas for safety reasons (EFE, 2015).

2.3 Battery Health Management for Electric UAVs

A Battery Health Management (BHM) system is necessary for using the energy stored in the batteries in a better way and provide real-time diagnosis information for the benefit of the operator of the aircraft. Unfortunately, the internal states of the battery such as the SOC, are not available for direct supervision. Therefore, it is important the development of battery monitoring systems that accurately estimate the internal states from external measurements available, such as voltage, current, and temperature. This concept of "Battery Health Management" has a wide variety of connotations, ranging from intermittent manual measurements of voltage and other variables to fully automated online supervision of various measured and estimated battery parameters.

Failure prognosis is also one of the critical components in BHM, especially in electric aircraft and vehicles. Accurate prognosis of RUL and EOD time is desired for such applications. However, a useful prognostic is not only an accurate remaining life estimate but also an assessment of the estimate's confidence. The latter is often expressed through a probability density function that envelopes the prediction, by allowing the computation of confidence bounds around it and implementing of making decisions strategies based on the concept of Just-In-Time Point. The latter incorporates the concept of risk, specifying the operating cycle of the system where the failure probability reaches a specified threshold. It is the uncertainty estimate that poses particular challenges to the prediction since it should account for various sources stemming from measurements, state estimation, model inaccuracies, and future load uncertainty (Goebel et al., 2008).

RUL and EOD prognosis requires of information of the SOC, but as mentioned previously, this internal parameter is not observable. Therefore, several methods for SOC estimation have been studied, and their performances have been compared each other. Bayesian methods have shown better results, and unlike other methods, they can adjust the SOC in real time for different discharging conditions (Chang, 2013). However, to use any of the Bayesian methods: Kalman Filter (EKF), Extended Kalman filter (EKF), Unscented Kalman Filter (UKF), or Particle Filter (PF), the relationship between the SOC and other measurable quantities such as voltage and current should be established. Several known relationships between the voltage at the terminals and the SOC are used to form a battery model where the current is considered as input. Nevertheless, regardless of the battery model used, methods based on Particle Filter have proven to be more accurate for predicting the RUL and EOD time (Goebel et al., 2008; Walker et al., 2015).

For purposes of BHM for electric UAVs, there have been proposed different battery models, and the future consumption, i.e., future model inputs, has been characterized in various ways. Below are some of them.

Battery Models

In Saha et al. (2011b), it is addressed the problem of Battery Health Management from the point of view of the battery model design in state-space. The effects of different choices in the model design space are explored in the context of prediction performance in an electric UAV application with emulated flight profiles. Although several models exist in literature at various levels of granularity and abstraction (Gao et al., 2002; Santhanagopalan et al., 2008; Hartmann, 2008), such models are complex and need identification of several parameters, which might be impractical in real-time applications. Therefore, for the purposes of the electric UAV BHM, they explore the model design space at a high level of abstraction of the underlying physics in order to predict the EOD event using a Bayesian framework, such as in (Saha et al., 2009), where utilizing the most basic implementation of the particle filter. Three models are proposed:

Model 1 The output voltage $E(t_k)$ of the cell is expressed in terms of the effects of the changes in the internal parameters, as shown below:

$$E(t_k) = E^\circ - \Delta E_{IR}(t_k) - \Delta E_{AP}(t_k) - \Delta E_{CP}(t_k), \tag{2.1}$$

where E° is the Gibb's free energy of the cell, ΔE_{IR} is the Ohmic drop (the diffusion process through which Li-ions migrate to the cathode via the electrolytic medium), ΔE_{AP} is the drop due to activation polarization (the dynamics of this process is described by the ButlerVolmer equation) and ΔE_{CP} denotes the voltage drop due to concentration polarization (the voltage loss due to spatial variations in reactant concentration at the electrodes). These individual effects are modeled as:

$$\Delta E_{IR} = \Delta I_k \cdot R - \alpha_{1,k} \cdot t_k, \tag{2.2}$$

$$\Delta E_{AP} = \alpha_{2,k} \cdot \exp(-\alpha_{3,k}/t_k), \tag{2.3}$$

$$\Delta E_{CP} = \alpha_{4,k} \cdot \exp(\alpha_{5,k} \cdot t_k), \tag{2.4}$$

where ΔI_k is the change in current that flows through the internal resistance R of the cell, and $\alpha_k = \{\alpha_{j,k}; j = 1, \ldots, 5\}$ represents the set of model parameters to be estimated.

Model 2 The model 1 does not represent the activation polarization process well. This is because the structure of the Butler Volmer equation is better approximated by a log function rather than a negative exponential. Hence for Model 2, Eq. 2.3 is changed to the following:

$$\Delta E_{AP}(t_k) = \alpha_{2,k} \ln(1 + \alpha_{3,k} \cdot t_k). \tag{2.5}$$

Model 3 It should be noted that for most batteries, the voltage as well as the charge delivered varies considerably with changes in I. This can be better represented by making two changes to the battery model described so far. Firstly, the parameters of the model should be load dependent. This is modeled by making α_3 and α_5 proportional to the load current I. Secondly, when there are step changes in the load, a higher load level followed by a lower one, the battery presents a period of relaxation. During this period the voltage does not immediately jump up, but gradually rises which can be modeled by an exponential function. A similar effect can also be observed for a step increase in current level. These effects can be reconciled by considering the battery impedance as an RC equivalent circuit. Thus Eq. 2.2 is replaced by:

$$\Delta E_{IRC}(t_k) = \Delta I_k \cdot \alpha_6 \cdot (1 - \exp(-\alpha_7(t_k - t_{\Delta I_k}))) - \alpha_1 \cdot t_k, \tag{2.6}$$

where ΔI_k is the step change in current at time $t_{\Delta I_k}$. The other processes are represented as:

$$\Delta E_{AP}(t_k) = \alpha_{2,k} \ln(1 + \alpha_{3,k} \cdot I_k \cdot t_k), \tag{2.7}$$

$$\Delta E_{CP}(t_k) = \alpha_{4,k} \cdot \exp(\alpha_{5,k} \cdot I_k \cdot t_k). \tag{2.8}$$

The test UAV platform for this research was a COTS 33% scale model of the Zivko Edge 540T (see Fig. 2.2). The gas engine in the original kit specification was replaced by two electric outrunner motors which are mounted in tandem to power a single drive shaft. The motors are powered by a set of four 5S 6000mAh Li-Po rechargeable batteries. The aircraft powertrain is illustrated in Fig. 2.3.

Testing on the Edge 540 UAV platform ware carried out with the airframe restrained on the ground (Hardware-In-the-Loop (HIL)). The propeller was run through various RPM (revolutions per minute) regimes indicative of the intended flight profile (takeoff, climb, multiple cruises, turn and glide segments, descent, and landing).

In addition, the consumption profile in the prognosis stage was assumed as the average value of the load current. According to EOD prognosis results, model 1 showed the worst performance, while model 3 was the best as was expected from the model choices. In general, higher granularity and lower levels of abstraction might give more accurate models, but that also results in larger parameter sets which may not have good convergence properties if included in the state vector. To manage such models, it would be needed to estimate most of the parameters from training data and choose only a few for online adaptation.

Subsequently, using the same scale model of the Zivko Edge 540T, in (Cuong et al., 2013) is presented a research that endeavors to produce and validate a technology for predicting the

remaining time until end-of-discharge of the batteries on an electric aircraft as a function of an expected future flight, and online estimates of the charge contained in the batteries. In this work, the original particle filter-based implementation (Saha et al., 2011b) is compared with a new Unscented Kalman Filter-based implementation that takes advantage of an improved battery model in order to improve health state estimation and end-of-discharge prediction performance. The results show a considerable improvement regarding previous particle filter based implementations of battery EOD prognosis; however, the improvements obtained are not attributed to the model or algorithm, but mainly to the use of a specific load profile in the prognosis stage instead of using the average of battery current. According to Cuong et al. (2013), a proper characterization of the future consumption not only leads to predictions more accurate, but they are more stable as well.

Fig. 2.4 shows the equivalent circuit battery model that makes use of three resistor and three capacitor components that are each tuned to match the observed current-voltage dynamics of the batteries used to power the propeller motors on the Edge-540T.

Battery charge is stored in the capacitor, C_b, in the equivalent circuit battery model. The R_s, C_s and R_{cp}, C_{cp} circuit element pairs capture battery internal resistance drops and concentration polarization effects, respectively. The resistor R_p is a large parasitic resistance that accounts for the slow battery self-discharge that is seen to occur over weeks or months

Figure 2.2: 33% Edge 540 test aircraft (Saha et al., 2011a).

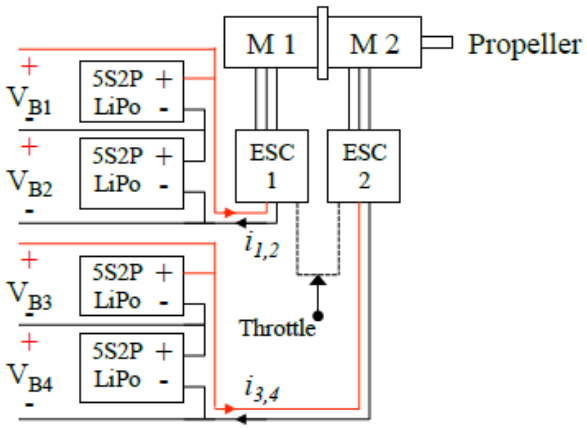

Figure 2.3: Motor System Diagram (Bole et al., 2014a).

of storage. Because battery current-voltage dynamics are known to vary as a function of battery SOC, some of the resistive and capacitive (RC) components in the equivalent circuit model should be parameterized as functions of battery SOC. Thus, battery SOC is defined as:

$$SOC = 1 - \frac{q_{max} - q_b}{C_{max}}, \tag{2.9}$$

where q_b is the charge stored in the battery, q_{max} is the maximum charge that the battery can hold, and C_{max} is the maximum charge that can be drawn from the battery. C_b, C_{cp}, and R_{cp} are parameterized as:

$$C_b = C_{Cb0} + C_{Cb1} \cdot SOC + C_{Cb2} \cdot SOC^2 + C_{Cb3} \cdot SOC^3, \tag{2.10}$$

$$C_{cp} = C_{cp0} + C_{cp1} \cdot \exp(C_{cp2} \cdot (SOC)), \tag{2.11}$$

$$R_{cp} = R_{cp0} + R_{cp1} \cdot \exp(R_{cp2} \cdot (SOC)), \tag{2.12}$$

where C_{Cb0}, C_{Cb1}, C_{Cb2}, C_{Cb3}, R_{cp0}, R_{cp1}, and R_{cp2} are empirical coefficients that are tuned based on observed current-voltage battery data over a range of SOC. The current and voltage dynamics of the equivalent circuit model are defined as:

$$x^B = \begin{bmatrix} q_b & q_{cp} & q_{cs} \end{bmatrix}^T \tag{2.13}$$

$$\dot{x}^B = \begin{bmatrix} -\frac{1}{C_b R_p} & \frac{1}{C_{cp} R_p} & \frac{1}{C_s R_p} \\ \frac{1}{C_b R_p} & -\frac{1}{C_{cp} R_p R_{cp}} & \frac{1}{C_s R_p} \\ \frac{1}{C_b R_p} & \frac{1}{C_{cp} R_p} & \frac{1}{C_s R_p} \end{bmatrix} x^B + \begin{bmatrix} \mathrm{i} \\ \mathrm{i} \\ \mathrm{i} \end{bmatrix} + \xi \tag{2.14}$$

$$y^B = V_p = \begin{bmatrix} \frac{1}{C_b} & \frac{1}{C_{cp}} & \frac{1}{C_s} \end{bmatrix} \cdot x^B \tag{2.15}$$

where q_b, q_{cp}, and q_{cs} represent the charge stored in C_b, C_{cp}, and C_{cs} respectively, and the voltage drop across the battery terminals is equal to the sum of the voltage drops across each of the three capacitors.

Future Consumption Profiles

The amount of available charge of a battery for a given discharge profile is not only dependent on the starting SOC, but also other factors like battery health and the discharge or load profile

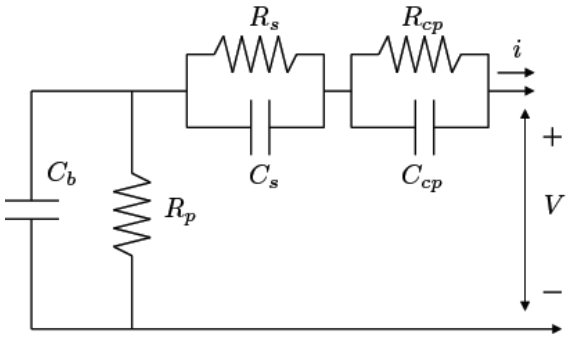

Figure 2.4: Equivalent circuit battery model (Cuong et al., 2013).

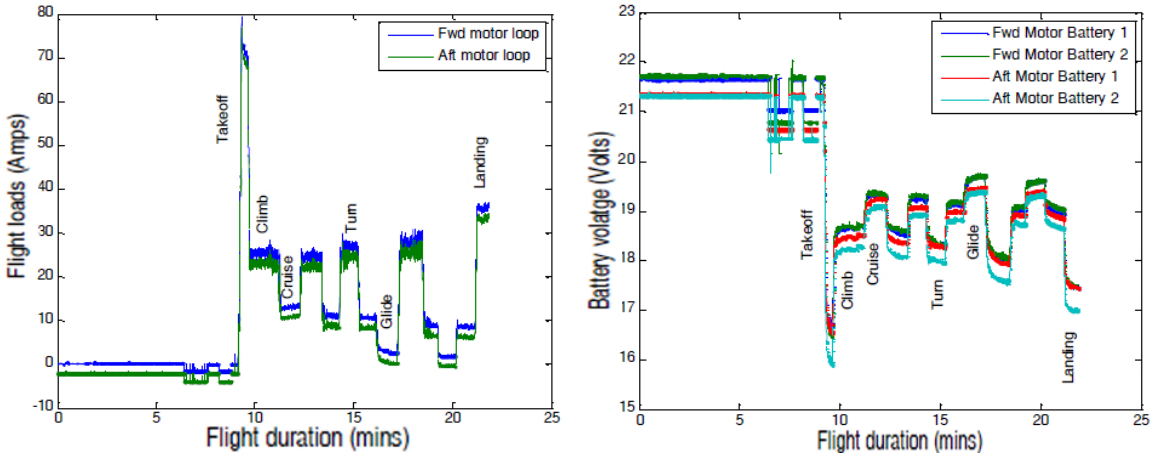

(a) (b)

Figure 2.5: Consumption profile during a typical flight (Saha et al., 2011b). (a) Load currents during a typical flight profile. (b) Battery voltages during a typical flight profile.

imposed. Just as for an electric car the future power draw may be inferred from the intended route, speed, and terrain data, the variables of interest for a pilot controlled UAV include wind speed and wind direction, air temperature and density, as well as the duration and velocity of different flight segments like climb, cruise, turns and descent.

For electric UAVs the variation in the load profile can be very unpredictable. For this reason, it is preferable that the system operator not only receive prognosis information based on expected load induced on the system, but also information about a range of load levels, including the extreme load levels (i.e. the maximum and minimum loads). Hence, the work in (Saha et al., 2011b) is expanded in (Saha et al., 2012). In this latter, Gaussian kernels are fitted to the load (I) distribution for different flight maneuvers. Table 2.1 shows a list of the mean, standard deviation, minimum and maximum values (rounded off to the nearest integer) for the load current (I_μ, I_σ, $I>$, $I<$, respectively) and duration (τ_μ, τ_σ, $\tau>$, $\tau<$) corresponding to each maneuver. Fig. 2.5 shows the currents and voltages during a typical flight profile.

Testing on the Edge 540 UAV platform was carried out with the airframe restrained on the ground. To validate the prognostic model, several flight tests were conducted using the UAV with randomized flight profiles using the Table 2.1. The prediction performance was

Table 2.1: Manoeuvre characterisation (I's in Amps; τ's in secs).

	I_μ	I_σ	$I>$	$I<$	τ_μ	τ_σ	$\tau>$	$\tau<$
M1:Takeoff	80	7	70	100	60	10	50	75
M2:Climb	30	5	22	40	120	10	90	140
M3:Cruise	15	3	10	22	90	10	70	115
M4:Turn	35	5	25	47	120	10	100	145
M5:Glide	5	1	2	8	90	10	75	120
M6:Landing	40	5	30	53	60	10	40	80

accurate to within 2 minutes, over multiple flights of durations between 15 to 25 minutes.

On the other hand, in (Cuong et al., 2013), the future loading on the batteries and the corresponding uncertainty is based on the knowledge of a flight plan previously defined. The plan is composed of the following phases:

1. Takeoff and climb to $\sim$ 200 meters (duration = 60 secs).
2. Maintain altitude, set throttle to 75% (duration = 275 secs).
3. Maintain altitude, set throttle to 85% (duration = 228 secs).
4. Maintain altitude, set throttle to 75% (duration = 142 secs).
5. Land and taxi down the runway (duration = 193 secs).
6. Fully deplete batteries by spinning the propeller at similar RPMs those observed in phase 4.

The purpose of spinning the propeller at similar RPMs to that observed during 75% throttle flight is to safely obtain an approximate measurement for the amount of flight time that would have been supported by the battery pack if the aircraft had continued to be flown at the approximately the same speed as it was going in phase 4. This measurement allows comparison between battery EOD predictions made at various points over the sample mission, and the EOD time observed experimentally.

Fig. 2.6 shows measured and predicted net battery power consumption over the sample flight. A uniform probability distribution ranging $\pm 30\%$ from the mean battery load estimate is added to future load estimates, denoted by the green band in Fig. 2.6, to account for unmodeled system dynamics.

In (Bole et al., 2014b), the power consumption is modeled based on aircraft aerodynamics and energy conservation equations. The equations below are developed using the following assumptions: (*i*) the propeller is mounted on the aircraft nose; (*ii*) the angle between the thrust vector generated by the propeller and the velocity vector of the aircraft is small; (*iii*) turning forces are small in comparison to thrust and drag forces in the direction of travel.

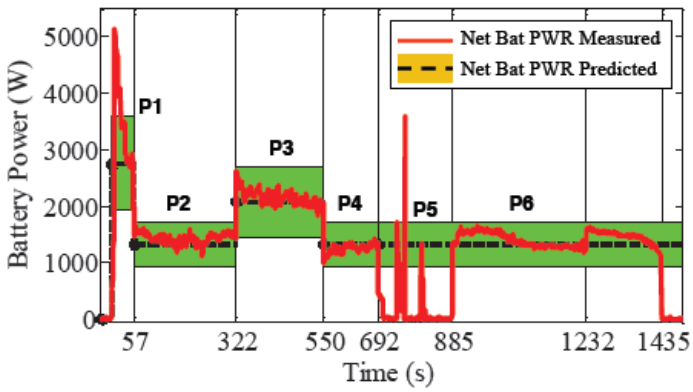

Figure 2.6: Measured and predicted net battery power consumption over sample flight. The six phases of the sample flight are annotated P1-P6 (Cuong et al., 2013).

The sum of the forces acting in the aircraft direction of travel is given by:

$$T_{x_w} = D(v) + m \cdot g \cdot \sin(\alpha) + m \cdot \dot{v}, \tag{2.16}$$

where T_{x_w} is the net force on the aircraft in the direction of travel, D is the drag force acting in the opposite direction of aircraft motion, v is the aircraft speed, $\dot{v}$ is acceleration, α is angle of climb, m is the vehicle mass, and g is total acceleration due to gravity.

The drag force on the airframe is represented by the following polynomial function of airspeed and angle of climb:

$$D(v, \alpha) = c_1 + c_2 \cdot v + c_3 \cdot v^2 + c_4 \cdot \alpha \text{ para } v \geq 15m/s. \tag{2.17}$$

During take-off and landing maneuvers when the aircraft speed is less than the stall speed of the aircraft the drag force is approximated as $D = 3$.

The product of thrust and airspeed gives the motive power exerted by the aircraft. A proportional relationship is used to model the ratio between the power output of the propeller and the resulting motive power:

$$P_p = \frac{1}{\eta_p} \cdot T_{x_w} \cdot v, \tag{2.18}$$

where P_p represents propeller output power, which is the product of its torque and speed, and η_p represents the approximate propeller output power conversion efficiency.

A fixed power conversion efficiency is assumed for the aircraft motors and other power electronics, such as the Electric Speed Controller (ESC),

$$P_{ESC} = \eta_{\mathrm{e}} \cdot P_p, \tag{2.19}$$

where P_{ESC} represents a power conversion efficiency factor and P_{ESC} represents net power at the input to the aircraft's two ESCs. The net ESC input power is equal to the sum of the power outputs from the two series connected battery strings,

$$P_{ESC} = P_{B1,2} + P_{B3,4}, \tag{2.20}$$

where $P_{B1,2}$ and $P_{B3,4}$ represent the battery power output for batteries $B1, B2$ and $B3, B4$ as denoted in Fig. 2.3. Although both ESCs receive the same throttle input command, their individual power draw is known to have a proportional relationship:

$$P_{B1,2} = \lambda \cdot P_{B3,4}, \tag{2.21}$$

where λ is constant of proportionality. Substitution of Eqs. 2.16-2.19 yields an expression for the approximate ESC input power required to fly at a particular airspeed and angle of climb,

$$\begin{aligned} P_{ESC} &= \frac{1}{\eta_{\mathrm{e}}\eta_p} \cdot T_{x_w} \cdot v \\ &= \frac{v}{\eta_{\mathrm{e}}\eta_p} \cdot (D(v, \alpha) + m \cdot g \cdot \sin(\alpha) + m \cdot \dot{v}). \end{aligned} \tag{2.22}$$

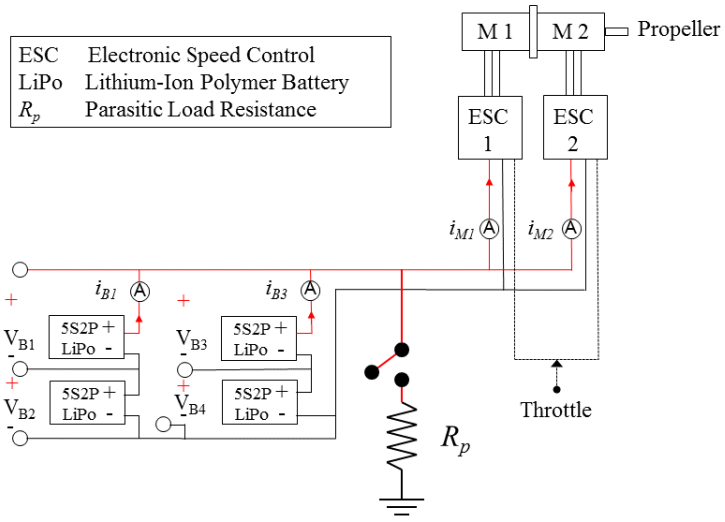

Figure 2.7: Schematic of electric Powertrain (Hogge et al., 2015).

The power demands on battery strings $B_{1,2}$ and $B_{3,4}$ are then estimated as,

$$P_{B_{1,2}} = \frac{\lambda}{1+\lambda} \cdot P_{ESC}, \tag{2.23}$$

$$P_{B_{3,4}} = \frac{1}{1+\lambda} \cdot P_{ESC}. \tag{2.24}$$

In (Bole et al., 2014a), authors use the aerodynamic and aircraft powertrain models described above to estimate future battery power demand as a function of a flight plan, and they extend the previous work published in (Cuong et al., 2013) on battery discharge prediction for electric vehicles. In (Cuong et al., 2013), the prediction of remaining flying time given a flight plan with no fixed termination time is considered. That approach is supplemented in (Bole et al., 2014a) by introducing new prognostic metrics that are used to evaluate the feasibility of completing a fixed duration mission. Also, the work in (Bole et al., 2014a) describes the incorporation of parasitic resistance faults into prognostic predictions (see Fig. 2.7).

Uncertainty in future load prediction is represented by defining a median future demand prediction with an upper and lower uncertainty bound. The upper and lower uncertainty bounds shown in Fig. 2.8 correspond to $\pm 30\%$ deviation from the future battery power estimated using Eq. 2.22 and Eq. 2.23.

The inputs to the prognostic estimator are (*i*) a set of sigma points representing battery state estimates; (*ii*) estimated $\pm 30\%$ uncertainty bounds on motor system power demands over a planned set of aircraft maneuvers; and (*iii*) online estimates of parasitic load faults. Prognostic estimates were reported in terms of two metrics; (*i*) the predicted battery SOC at the end of a flight plan, and (*iii*) the predicted time to reach either the battery low-voltage cut-off threshold or the end of a flight plan. Fig. 2.9 and Fig. 2.10 show the results.

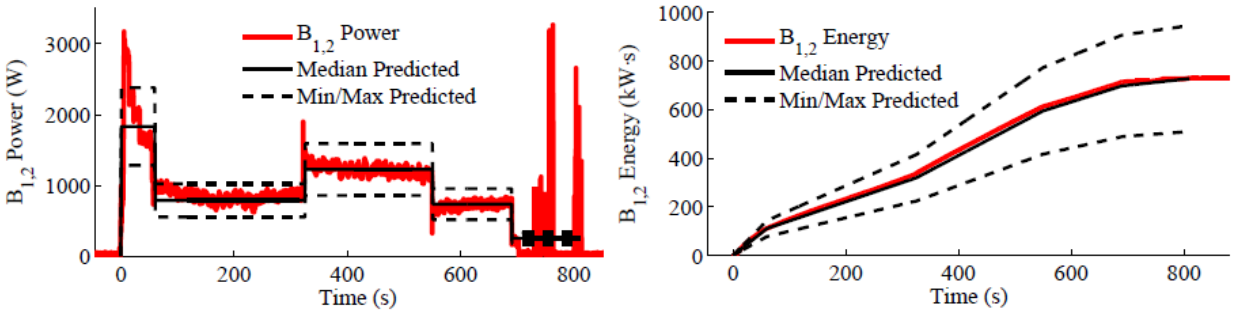

Figure 2.8: Plots of measured and predicted $B_{1,2}$ output power and energy over a sample flight (Bole et al., 2014a).

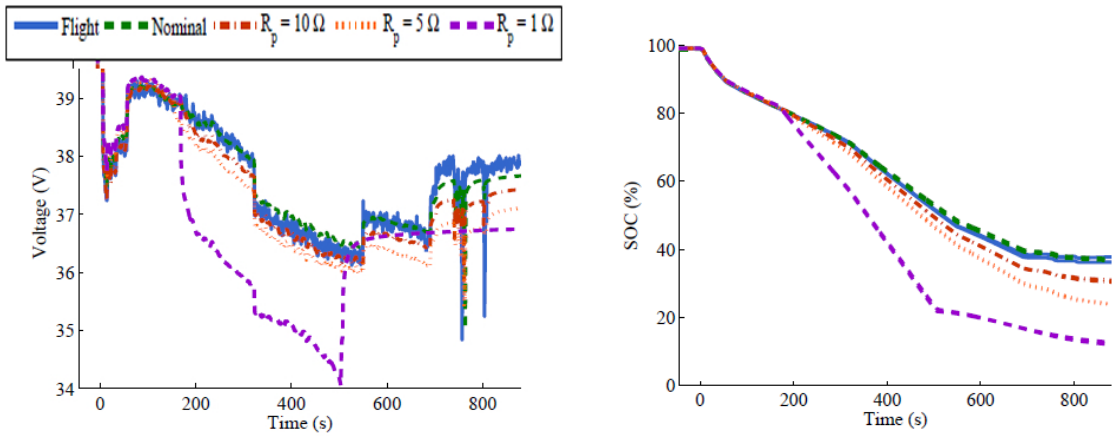

Figure 2.9: Comparison of (a) voltage measurements and (b) SOC estimates for batteries B_1 and B_2 over a sample flight and four test cases that include injected parasitic resistances of various magnitudes (Bole et al., 2014a).

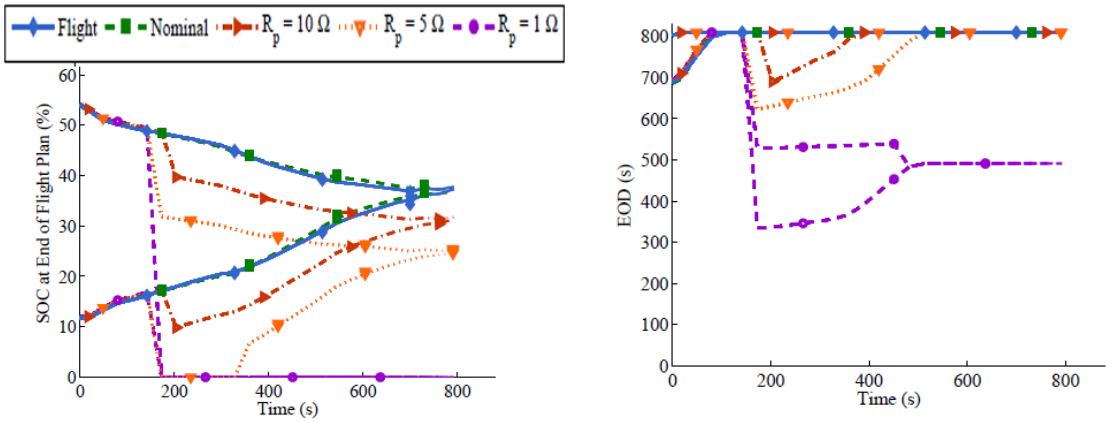

(a) (b)

Figure 2.10: Prediction uncertainty bounds for two prognostic metrics plotted at 30 second time intervals over five battery discharge data sets (Bole et al., 2014a). (a) Predicted battery SOC at the end of a flight plan. (b) Predicted time to reach a battery EOD threshold.

Other Aspects about BHM for UAVs

Continuing with the work by Bole et al. (2014a), Hogge et al. (2015) introduce a verification testing procedure that is intended to build trust in predictions of remaining flying time. The philosophy behind the testing procedure described there is to translate system performance and safety goals into requirements for an alarm that warns system operators when the estimated remaining flying time falls below a certain threshold. Again, testing on the Edge 540 UAV platform was carried out with the airframe restrained on the ground. This vehicle has been actively used by researchers at NASA Langley Research Center (NASA LaRC) to facilitate the rapid deployment and evaluation of remaining flying time prediction algorithms for electric aircraft.

Remaining flying time prediction algorithms focus on the prediction of battery charge depletion over an electric UAV flight. A lower-bound on the battery SOC that is considered safe for flight is set at 30% in this work. Flying the vehicle with batteries below 30% SOC is considered to be a high-risk mode of operation that violates the vehicle's safe operating guidelines. Such violations of operating guidelines are known as a functional failure of the vehicle's mission.

The accuracy of onboard remaining flying time estimation algorithms is tested in this work, by conducting a series of controlled run-to-functional-failure experiments on the ground. The predictive element to be tested in this work is an alarm that warns system operators when the powertrain batteries are two minutes from reaching 30% SOC under normal operations. Fig. 2.11 shows the difference between the time at which the two minutes remaining alarm was raised and the time at which the lowest battery SOC estimate crosses 30% for 26 runs.

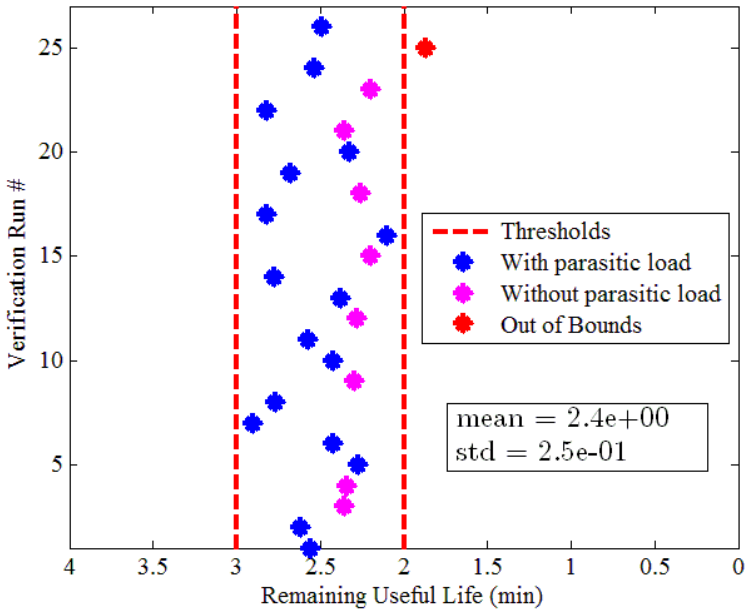

Figure 2.11: Two-minute alarms for 26 runs (Hogge et al., 2015).

2.3.1 BHM for Rotary-wing UAVs

(de Souza Candido et al., 2014) is the only work reported in the literature that addresses the problem of BHM for rotary-wing UAVs. The main contribution of (de Souza Candido et al., 2014) is the use of the EOD time predictions for intelligent flight plan reconfiguration. Particle filter was used to predict the EOD time. Information about future consumption profiles used during the prognosis stage is not provided.

The proposed method was evaluated by numerical simulation to evaluate its performance, in a context of limited battery energy source. The simulations were based on the Omni-directional Stationary Flying OUtstretched Robot – OS4 Mini-VTOL (previously used in (Bouabdallah, 2007)). The OS4 is powered by a Li-Po $3Cell$, $11.1V$, $3300mAh$ battery, which takes almost one-half of the total mass of the multirotor. It was considered that the EOD is reached when the output voltage hits the minimum safe voltage threshold of $3.0V$ per single cell, i.e., the discharge cutoff voltage is $9V$.

A set of 11 waypoints are defined for plotting the flight plan, including the start waypoint, and the end waypoint. When it is identified that with the present power demand it will not be possible to complete the original mission, then it is solved a Mixed Integer Linear Programming (MILP) optimization problem to select a new set of waypoints from the original mission that can be completed.

However, the model used for the DC motors is inadequate to accurately represent the energy consumption of the quadrotor over different flight stages. Such model characterizes the torque on the motor only for the state of hovering, without considering the other stages: climb, descent, and forward flight. The magnitude of the torque on the motors for each one of these stages is different and therefore the energy consumption is different as well. During most of the flight, the multirotor is in forward flight. Hence, to presume that the multirotor is in hovering flight during the full path might result in significant errors.

(Gatti et al., 2015) is another research efforts related to the flight endurance for battery-powered rotary-wing aircraft, although it is not exactly working on BHM for UAVs. Such work presents an analytical study of battery-powered rotary-wing aircraft endurance in hovering flight condition, and its experimental validation is carried out by using a multi-rotor platform.

The results show that by increasing the capacity from 10 to 20 Ah, one gains about 10 min of hovering time, for the considered platform, which largely increases the initial endurance. A further increase of 10Ah increases endurance by less than 5 min. A further increase from 30 to 40 Ah provides only 2 min of additional hovering capability. These data represent a further proof for the importance of correctly addressing the issue of preliminary sizing of the battery-powered aircraft, especially for multirotor platforms. Trying to increase the endurance of an already existing platform by simply adding batteries may not be an effective solution, as propeller operates at higher motor regimes, where the decreasing slope of the endurance vs. capacity plot provides only a marginal improvement.

Similarly to work in (de Souza Candido et al., 2014), in (Gatti et al., 2015) only is con-

sidered the hovering flight condition without including the other flight stages. In addition, the uncertainty on the power consumption associated with changes in the strength of the wind, or to other environmental conditions, is not considered. The battery dynamics has not been included, and a constant voltage is assumed instead. Moreover, a SOC threshold or a discharge cutoff voltage is not established.

2.3.2 Considerations on the Performance of Rotary-wing UAVs

A multirotor's performance is dependent on the power output of the engine and the lift produced by the rotors. Any factor that affects engine and rotor efficiency affects performance. The three major factors that affect performance are density altitude (air density in relation to altitude), weight, and wind (Federal Aviation Administration, 2013; Habis, 2015). Remember that the pressure, temperature, and density are inversely proportional to the height. To greater height, lower pressure, lower temperature, and lower density. The density is also inversely proportional to the temperature. Higher temperatures, lower density.

2.3.2.1 Density Altitude

Air gets thinner with altitude and heat; manned aviation uses the concept of density altitude to predict the performance of aircraft based on altitude, non-standard pressure, and temperature. Flying at 1800 meters in the mountains or on a $32°C$ summer day will greatly decrease the ability of the multirotor's propellers to generate lift, which will affect maximum allowable payload and flight time.

2.3.2.2 Winds

Everyone who has flown a multirotor under non-calm winds understands that high winds can make it harder and sometimes impossible to control. What is less obvious is how much faster a battery will drain while holding in windy conditions or flying into a headwind.

Wind direction and velocity also affect hovering, takeoff, and climb performance. Translational lift (a transitional state that occurs after a multirotor has moved from hover to forward flight. This state provides extra lift.) occurs any time there is relative airflow over the rotor disk. This occurs whether the relative airflow is caused by helicopter movement or by the wind. As wind speed increases, translational lift increases, resulting in less power required to hover. The wind direction is also an important consideration. Headwinds are the most desirable as they contribute to the greatest increase in performance.

Similarly, as higher wind speeds lead to better lift, and lower power required, the forward motion provides airflow over the blades which enhances the lift on the multicopter. As such, forward flight is much better for motor life and to increase battery flight time. That is, the power consumption is lower in forward flight than in hovering flight. However, there is a

limit speed that if you exceed the aerodynamic drag on the multirotor will start to kick in, requiring extra power to overcome (Quadcopter Flight School, 2014).

2.3.2.3 Moisture (Humidity)

Moisture in the form of fog, mist or rain can short drone electronics that are not well protected. Relative humidity, when too close to 100 percent is an early warning of moisture. There are no rules of thumb used to compute the effects of humidity on density altitude, but some manufacturers include charts with 80 percent relative humidity columns as additional information. There appears to be an approximately 3-4 percent reduction in performance compared to dry air at the same altitude and temperature, so expect a decrease in hovering and takeoff performance in high humidity conditions. Although 3-4 percent seems insignificant, it can be the cause of a mishap when already operating at the limits of the multirotor. This brings-up something known as the "human weather test": if the weather is not pleasant enough for the human operator to stand outside during the duration of the flight, then a visual-line-of-sight mission should be postponed.

2.3.2.4 Temperature

Temperature operating ranges for small-size multirotors range between $0°C$ and $40°C$ (DJI, 2016), due to temperatures below $0°C$ can cause structural icing on propeller blades which can significantly reduce their ability to generate lift, and even can have catastrophic consequences. The icing is one of the top killers of manned aviation and could very well become a top drone killer.

Nevertheless, operate at low temperatures, but above $0°C$, leads to better aerodynamic performance because air is denser and usually drier. Therefore, rotors will increase its ability to generate lift, and will not have to work so hard (Habis, 2015). Thus, the required power is smaller at low temperatures. To illustrate, the power required in hovering condition is given by (Gatti et al., 2015):

$$P_h = \frac{W^{3/2}}{f \cdot \sqrt{2\rho A_t}}, \tag{2.25}$$

where W is the total aircraft weight, f is the figure of merit of the rotor, ρ is air density, and A_t is the total disc area. The power required is inversely proportional to the square root of the air density; so at lower temperatures, lower power consumption, and as a result, longer flight time (Elsen, 2014; Mueller, 2016). See Table 2.2.

Temperature also affects the battery performance; however, there are no substantial changes in the operating range of the UAV, namely, between $0°C$ and $40°C$ (Zang et al., 2014; Cessford and Barwood, 2015). The battery performance is affected mostly below $-10°C$ and during first 5 minutes of the discharge. Therefore, Cessford and Barwood (2015) conclude and suggest to operate the UAV between $0°C$ and $20°C$ degrees. However, temperatures above $20°C$ are not a problem for the performance of the battery during discharge, partly because the wind and air flow induced by the helices lead to the cooling of the battery.

Table 2.2: Hover Time vs. Air Temperature for 3DR IRIS+ Quadcopter Elsen (2014).

Cells	Capacity (mAh)	Air temperature ($°C$)	Hover time (min)
3S	3500	5	8.3
3S	3500	10	8.2
3S	3500	15	8.1
3S	3500	20	8.1
3S	3500	25	8.0
3S	3500	30	7.9
3S	3500	35	7.9
4S	3000	5	9.1
4S	3000	10	9.0
4S	3000	15	9.0
4S	3000	20	8.9
4S	3000	25	8.8
4S	3000	30	8.7
4S	3000	35	8.7

Recent research efforts seek to include other materials in the building of Li-ion batteries; in order enhance the performance at temperatures below $0°C$ (Zhu et al., 2015; Wang et al., 2016), and so, enable the usage of fixed-wing UAVs in applications of high altitude or space missions. The problem can be mitigated by adding external heaters and insulating material to the battery, but with a severe weight penalty. Therefore, researchers at Pennsylvania State University and the software company EC Power have developed an all-climate battery (a new lithium-ion battery that can self-heat if the temperature is lower than $0°C$) by adding a metal sheet inside the conventional battery (Wang et al., 2016). At low temperatures, the current is diverted through the sheet and heat is produced due to its electrical resistance. When the internal temperature of the battery rises to above $0°C$, a switch is activated in such a way the battery come back to its normal operation. Just it is necessary to negotiate a small amount of the battery capacity, to achieve an increase in the available power regarding conventional batteries.

2.3.2.5 Weight

Such as was mentioned above, the flight time is directly related to the weight of the UAV. At greater weight, greater will be the power required (see Eq. 2.25). For example, according to the specifications of the 3DR IRIS+ quadcopter, the flight time without additional load is 22 minutes, and the flight time with the maximum allowed load is 16 minutes. In this case, this also means that the battery is operating with discharge rates between 2.72 and 3.75 times the nominal discharge rate (*C-rate*). Although generally, UAVs with batteries as main power source operate between $3C$ and $4C$. Hence also, that the flight times are usually short.

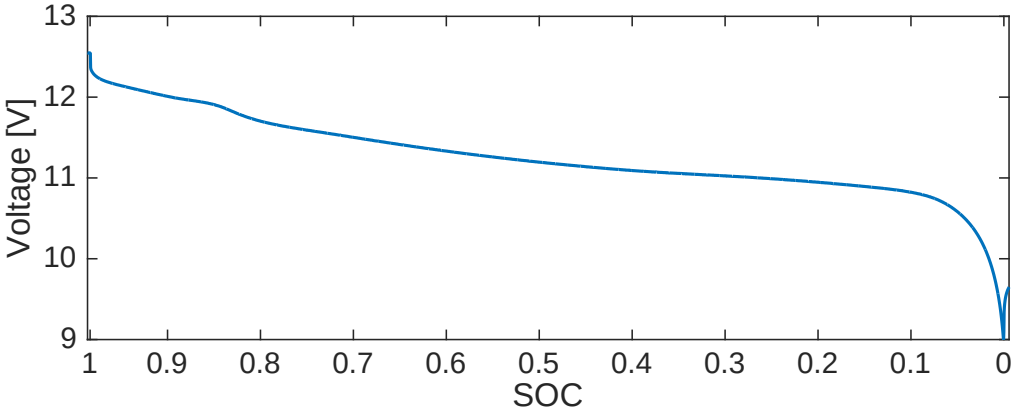

Figure 2.12: A typical relationship between SOC and OCV in Li-ion batteries.

2.4 SOC Estimation and Prognosis Methods for Batteries

The SOC of a battery is used to describe its remaining capacity; however, a battery is a chemical energy storage source, and this chemical energy cannot be directly accessed. Accurate estimation of the SOC remains very complex and is difficult to implement because battery models are limited and there are parametric uncertainties. Some SOC estimation methods are presented below (Chang, 2013):

2.4.1 Direct Measurement

Direct measurement methods refer to some physical battery properties such as the terminal voltage and impedance. Many different direct methods have been employed: open circuit voltage method, terminal voltage method, impedance measurement method, and electrochemical impedance spectroscopy method.

2.4.1.1 Open Circuit Voltage Method

There is approximately a linear relationship between the SOC of the lead-acid battery and its Open Circuit Voltage (OCV). In that case, the OCV method based on the OCV of batteries is proportional to the SOC when they are disconnected from the loads for a period longer than two hours. However, such a disconnection time may be too long to be implemented in real-time applications (Ng et al., 2008).

Also, Unlike the lead-acid battery, the Li-ion battery does not have a linear relationship between the OCV and SOC. A typical relationship of Li-ion battery between SOC and OCV is shown in Fig. 2.12. Therefore, the relationship between the OCV and SOC cannot be the same for all batteries (Lee et al., 2008).

2.4.1.2 Impedance Spectroscopy Method

The impedance measurement provides information on various parameters related to the SOC. This method measures battery impedances over a wide range of AC frequencies at different charge and discharge currents. The values of the model impedances are found by least-squares fitting to measured impedance values. SOC may be indirectly inferred by measuring present battery impedances and correlating them with known impedances at various SOC levels (Bundy et al., 1998; Ran et al., 2010). However, this method requires expensive equipment that usually found only in laboratories, restricting their application in practice.

2.4.2 Book-keeping Estimation

This method uses discharging current as the input and integrates the discharging current over time to calculate the SOC.

2.4.2.1 Coulomb Counting Method

The Coulomb counting method measures the discharging current of a battery and integrates the discharging current over time in order to estimate SOC. Coulomb counting method is done to estimate the $SOC(t)$, which is estimated from the discharging current, $I(t)$, and previously estimated SOC values, $SOC(t-1)$. SOC is calculated by the following equation:

$$SOC(t) = SOC(t-1) + \frac{I(t)}{Q_n} \cdot \Delta t \tag{2.26}$$

This method is easy to implement and can be used in online applications; but there are several factors that affect the accuracy of Coulomb counting method including temperature, battery history, discharge current, cycle life, among others (Ng et al., 2009).

2.4.3 Adaptive Systems

Recently, with the development of artificial intelligence, various new adaptive systems for SOC estimation have been developed. The developed methods include Back Propagation (BP) neural network, radial basis function (RBF) neural network, fuzzy logic methods, support vector machine, fuzzy neural network, and Bayesian methods, among others. The adaptive systems are self-designing ones that can be automatically adjusted in changing systems. As batteries have been affected by many chemical factors and have nonlinear SOC, adaptive systems offer a good solution for SOC estimation.

2.4.3.1 BP Neural Network

The BP neural network is applied in SOC estimation due to their good ability of nonlinear mapping, self-organization, and self-learning. The artificial neural network based SOC indicator predicts the current SOC using the recent history of voltage, current, and the ambient temperature of a battery (Charkhgard and Farrokhi, 2010; Chang, 2012; Weigert et al., 2011). For example, The architecture of the SOC estimating BP neural network by (Chang, 2013) contains an input layer, an output layer, and a hidden layer. The input layer has three neurons for terminal voltage, discharge current, and temperature, the hidden layer has g neurons, and the output layer has only one neuron for SOC.

This method requires training and validation data to generate and adjust the model, which can be used for estimation or prognostic purposes. However, these models can present overadjustment to the training and validation data, and the results may correspond to local optima.

2.4.3.2 Fuzzy Logic Systems

Fuzzy logic method provides a powerful means of modeling nonlinear and complex systems. The method involves the use of fuzzy logic models to analyze data obtained by impedance spectroscopy, Coulomb counting methods, or measurements of voltage, current or temperature. The output of the fuzzy model is the estimated SOC (Salkind et al., 1999; Singh et al., 2006). This approach represents a reasonable way for online SOC estimation and uncertainty characterization, but even so, the SOC prediction is still unresolved and mainly treated as a curve regression problem which is insufficient for purposes of risk characterization.

2.4.3.3 Bayesian Methods

In recent years there has been a growing interest in the use of stochastic filtering techniques to estimate the SOC and parameter degradation of a Li-Ion battery under randomly varying loading conditions, due to they can perform real-time estimations using online measurements.

Among these methods are those based on Extended Kalman Filter (EKF) (Hu et al., 2012; Barbarisi et al., 2006). The EKF relies on a non-linear battery model, like an equivalent circuit, and approximates the covariance error matrix associated to the state estimation using both the non-linear and linearization of the dynamic system that represents the battery discharge process. During the estimation process the EKF adjust the parameters and model states as new measurements are available, but for prognostics for n-step ahead, linearization errors are overly important to be neglected.

Unscented Kalman Filter (UKF) is a Kalman filter based on sampling that has shown better performance than the EKF, in particular, in SOC estimation for Li-ion batteries (Zhang and Xia, 2011; Sun et al., 2011). UKF chooses samples from the states by using the covariance matrix. Samples are passed through the model equations and then, are re-

evaluated by the mean and variance without linearization of model equations. However, UKF assumes the states have a gaussian distribution.

Recently the Particle Filter (PF) is emerging as the preferred method due to it has shown a good performance in estimation and prediction processes with non-linear and non-necessary Gaussian noises (Walker et al., 2015; Goebel et al., 2008). These methods also provide a concrete characterization of uncertainty sources both in the filtering and the prediction stage, a piece of information that is required for the generation of a risk measure associated with SOC prognosis.

A Particle Filter (PF) is a sequential Monte Carlo method that approximates the state probability density function (PDF) using a weighted set of samples, called particles. The value of each particle describes a possible system state, and its weight denotes the likelihood of the observed measurements given this particle's value. As more observations are obtained, the value of each particle in the next time step is predicted by stochastically moving each particle to a new state using a non-linear process model describing the evolution in time of the system under analysis, a measurement model, a set of available measurements, and an a priori estimate of the state PDF. Then, the weight of each particle is updated to reflect the likelihood of that observation given the particle's new state. For prognostics, the PF is used only to predict the future values of particles based on future operating loading profiles, and not update them for future operating loading profiles, since future measurements are not available (Saxena et al., 2012).

Battery Models for Bayesian Prognostics Framework To use Bayesian techniques the relationship between SOC and other measurable units, such as voltage, current or temperature, should be established, namely, a model that describes how the system evolves in time in response to its inputs. Whit this purpose, an electrochemistry-based model of lithium-ion batteries that capture the significant electrochemical processes is developed in (Daigle and Kulkarni, 2013).

In this model, the voltage terms of the battery are expressed as functions of the amount of charge in the electrodes (the states of the model). Each electrode, positive (subscript p) and negative (subscript n), is split into two volumes, a surface layer (subscript s) and a bulk layer (subscript b). The differential equations for the battery describe how charge moves through these volumes. The charge (q) variables are described using:

$$\dot{q}_{s,p} = \mathrm{i}_{app} + \dot{q}_{bs,p} \tag{2.27}$$
$$\dot{q}_{b,p} = -\dot{q}_{bs,p} + \mathrm{i}_{app} - \mathrm{i}_{app} \tag{2.28}$$
$$\dot{q}_{b,n} = -\dot{q}_{bs,n} + \mathrm{i}_{app} - \mathrm{i}_{app} \tag{2.29}$$
$$\dot{q}_{s,n} = -\mathrm{i}_{app} + \dot{q}_{bs,n}, \tag{2.30}$$

where i_{app} is the applied electric current. The term $\dot{q}_{bs,\mathrm{i}}$ describes diffusion from the bulk to surface layer for electrode i, where $\mathrm{i} = n$ or $\mathrm{i} = p$.

$$\dot{q}_{bs,\mathrm{i}} = \frac{1}{D}(c_{b,\mathrm{i}} - c_{s,\mathrm{i}}) \tag{2.31}$$

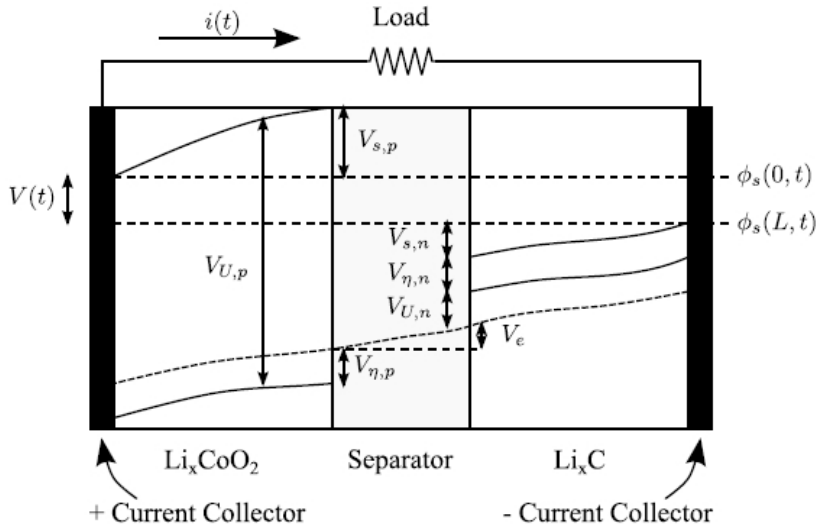

Figure 2.13: Battery voltages (Daigle and Kulkarni, 2013).

where D is the diffusion constant. The c terms are lithium ion concentrations:

$$c_{b,\mathrm{i}} = \frac{q_{b,\mathrm{i}}}{v_{b,\mathrm{i}}} \tag{2.32}$$

$$c_{s,\mathrm{i}} = \frac{q_{s,\mathrm{i}}}{v_{s,\mathrm{i}}} \tag{2.33}$$

Here, $c_{v,\mathrm{i}}$ is the concentration of charge in electrode i, and $v_{v,\mathrm{i}}$ is the total volume of charge storage capability. We define $v_{\mathrm{i}} = v_{b,\mathrm{i}} + v_{s,\mathrm{i}}$. Note now that the following relations hold:

$$q_p = q_{s,p} + q_{b,p} \tag{2.34}$$

$$q_n = q_{s,n} + q_{b,n} \tag{2.35}$$

$$q^{max} = q_{s,p} + q_{b,p} + q_{s,n} + q_{b,n} \tag{2.36}$$

It can also express mole fractions (x) based on the q variables:

$$x_{\mathrm{i}} = \frac{q_{\mathrm{i}}}{q^{max}}, \tag{2.37}$$

$$x_{s,\mathrm{i}} = \frac{q_{s,\mathrm{i}}}{q^{max}_{s,\mathrm{i}}}, \tag{2.38}$$

$$x_{b,\mathrm{i}} = \frac{q_{b,\mathrm{i}}}{q^{max}_{b,\mathrm{i}}}, \tag{2.39}$$

where $q^{max} = q_p + q_n$ refers to the total amount of available Li-ions. It follows that $x_p + x_n = 1$. For Li-ion batteries, when fully charged, $x_p = 0.4$ and $x_n = 0.6$. When fully discharged, $x_p = 1$ and $x_n = 0$.

The different potentials are summarized in Fig. 2.13. The overall battery voltage $V(t)$ is the difference between the potential at the positive current collector, $\phi_s(0,t)$, and the negative current collector, $\phi_s(L,t)$, minus resistance losses at the current collectors (not shown in the diagram). At the positive current collector is the equilibrium potential $V_{U,p}$.

This voltage is then reduced by $V_{s,p}$, due to the solid-phase ohmic resistance, and $V_{\eta,p}$, the surface overpotential. The electrolyte ohmic resistance then causes another drop V_{e}. At the negative electrode, there is a drop $V_{\eta,n}$ due to the surface overpotential, and a drop $V_{s,n}$ due to the solid-phase resistance. The voltage drops again due to the equilibrium potential at the negative current collector $V_{U,n}$. These voltages are described by the following set of equations:

$$V_{U,\mathrm{i}} = U_o + \frac{RT}{nF}\ln(\frac{1-x_{s,\mathrm{i}}}{x_{s,\mathrm{i}}}) + V_{INT,\mathrm{i}} \tag{2.40}$$

$$V_{INT,\mathrm{i}} = \frac{1}{nF}\left(\sum_{k=0}^{N_{\mathrm{i}}} A_{\mathrm{i},k}\left((2x_{\mathrm{i}}-1)^{k+1} - \frac{2x_{\mathrm{i}}k(1-x_{\mathrm{i}})}{(2x_{\mathrm{i}}-1)^{1-k}}\right)\right) \tag{2.41}$$

$$V_o = \mathrm{i}_{app}R_o \tag{2.42}$$

$$V_{\eta,\mathrm{i}} = \frac{RT}{F\alpha}arc\sinh\left(\frac{J_{\mathrm{i}}}{2J_{\mathrm{i}0}}\right) \tag{2.43}$$

$$J_{\mathrm{i}} = \frac{\mathrm{i}}{S_{\mathrm{i}}} \tag{2.44}$$

$$J_{\mathrm{i},0} = k_{\mathrm{i}}(1-x_{s,\mathrm{i}})^{\alpha}(x_{s,\mathrm{i}})^{1-\alpha} \tag{2.45}$$

$$V = V_{U,p} - V_{U,n} - V'_o - V'_{\eta,p} - V'_{\eta,n} \tag{2.46}$$

$$\dot{V}'_o = \frac{V_o - V'_o}{\tau_o} \tag{2.47}$$

$$\dot{V}'_{\eta,p} = \frac{V_{\eta,p} - V'_{\eta,p}}{\tau_{\eta,p}} \tag{2.48}$$

$$\dot{V}'_{\eta,n} = \frac{V_{\eta,n} - V'_{\eta,n}}{\tau_{\eta,n}} \tag{2.49}$$

Here, U_0 is a reference potential, R is the universal gas constant, T is the electrode temperature (in K), n is the number of electrons transferred in the reaction ($n = 1$ for Li-ion), F is Faraday's constant, J_{i} is the current density, and $J_{\mathrm{i}0}$ is the exchange current density, k_{i} is a lumped parameter of several constants including a rate coefficient, electrolyte concentration, and maximum ion concentration. $V_{INT,\mathrm{i}}$ is the activity correction term (0 in the ideal condition). The τ parameters are empirical time constants(used since the voltages do not change instantaneously). This model contains as states $q_{s,p}$, $q_{b,p}$, $q_{b,n}$, $q_{s,n}$, V'_o, $V'_{\eta,p}$, and $V'_{\eta,n}$. The single model output is V .

The above model has shown very accurate prognostics results for EOD, with the uncertainty associated with the model remaining very small. However, the literature also reported less complex battery models for prognostic that has shown reasonable prognostics results for EOD. For example, (Pola et al., 2015) proposed an empirical state space model, inspired by battery phenomenology that assumes a discrete-time characterization for the battery dynamics, and the availability (real-time) of voltage and discharge current measurements (Eq.2.50-Eq.2.52). The structure of the proposed state-space model offers a modification to the observation equation that incorporates most of the nonlinearities found in Li-Ion open-voltage discharge curves.

State transition model:

$$x_1(k+1) = x_1(k) + w_1(k) \tag{2.50}$$
$$x_2(k+1) = x_2(k) - v(k) \cdot \mathrm{i}(k) \cdot \Delta t \cdot E_{crit}^{-1} + w_2(k) \tag{2.51}$$

Measurement equation:

$$\begin{aligned} v(k) = v_L + (v_0 - v_L) \cdot \mathrm{e}^{\gamma(x_2(k)-1)} + \alpha \cdot v_L(x_2(k) - 1) + \ldots \\ \ldots + (1-\alpha)v_L(\mathrm{e}^{-\beta} - \mathrm{e}^{-\beta\sqrt{x_2(k)}}) - \mathrm{i}(k) \cdot x_1(k) + \eta(k) \end{aligned} \tag{2.52}$$

The discharge current $\mathrm{i}(k)$ (measured in amperes), and the sample time Δt (measured in seconds) are input variables, and the battery voltage $v(k)$ (measured in volts) is the system output. The quantities v_L, α, β, and γ are model parameters to be estimated off-line. The states are defined as $x_1(k)$ (unknown model parameter), and $x_2(k)$ (SOC, remnant battery energy normalized by the parameter E_{crit}). E_{crit} is the expected total energy delivered by the ESD (that could be inferred from the nominal capacity or discharge curves included in datasheets). Process (w_1 and w_2) and measurement (η) noises are assumed Gaussian. It is important to mention that process noise w_2 is correlated with η, the measurement noise because the evolution in time of state x_2 depends on voltage measurements.

The concept of artificial evolution has been applied to estimate the instantaneous absolute value of the battery internal impedance. This concept is implemented by extending the dimension of the state vector, and associating its first component with the value of this time-varying parameter.

Artificial Evolution and Outer Feedback Correction Loops Artificial evolution (Orchard and Vachtsevanos, 2009) is a method used for unknown model parameter estimation that proposes the augmentation of the state vector of the system. The state equations related to unknown model parameters assume random walk models to implement learning procedures that allow simultaneous estimation of parameters and state variables of the system. Outer Feedback Correction Loops (OFCL) (Marcos E. Orchard, 2009) are a class of algorithms that propose to manipulate the hyper-parameters that characterize the aforementioned random walk models. Given the system:

$$x_{k+1} = g(x_k, \theta, w_k) \tag{2.53}$$

where x_k is the state vector, θ is the parameter vector and w_k is process noise. If $\theta = \begin{pmatrix} \theta^c \\ \theta^{uc} \end{pmatrix}$, where θ^{uc} is a vector of uncertain parameters, artificial evolution proposes to consider the system

$$x_{k+1} = g(x_k, \theta_k, w_k) \tag{2.54}$$
$$\theta_{k+1}^{uc} = \theta_k^{uc} + w_k^{\theta} \tag{2.55}$$

where w_k^{θ} is a random variable. OFCL can modify hyper-parameters of w_k^{θ} to gradually reduce or increase the uncertainty associated to θ^{uc} in order to diminish the bias in Bayesian state estimation.

For exampe, the OFCLs by (Tampier et al., 2015) (Alg. 2.1) uses the observation error in earlier time horizons to determine whether to increase or decrease the variance of the process noise.

if $t > t_{min}$ **then**
  $\mathrm{e}_{acum} = \mathrm{e}_{acum} + |\mathrm{e}_{obs}|$
  if $\mathrm{e}_{acum} \leq \mathrm{e}_{th}$ **then**
    $std(w_{\mathrm{i}}(t)) = max(p_{\mathrm{i}} \cdot std(w_{\mathrm{i}}(t)), std_{\mathrm{i}})$
  else
    $\mathrm{e}_{acum} = 0$
    $std(w_{\mathrm{i}}(t)) = q_{\mathrm{i}} \cdot std(w_{\mathrm{i}}(t))$
  end if
end if

Algorithm 2.1: Outer Feedback Correction Loop (OFCL) by (Tampier et al., 2015).

This particular OFCL is not based on short-term prediction results, but on the accumulated observation error. In this case, t_{min} corresponds to the instant in which the OFCL starts operating, e_{obs} is the observation error (the difference between the acquired measurement for the output and the one expected by the estimation algorithm), e_{acum} is a variable that accumulates the past observation errors with initial value of zero, and e_{th} is the decision threshold to modify the process noise. In other words, if it is lower than the threshold, the standard deviation of the process noise is reduced, but if it is larger than the threshold, it increases. Also p_1 and p_2 are constants with values between 0 and 1, while q_1 and q_2 are constants bigger than 1. Finally, std_1 and p_2 are the lower bounds which indicate the minimum standard deviation accepted value.

2.5 A Particle-filtering-based Prognosis Scheme for nonlinear Dynamic Systems

2.5.1 Particle Filter

Particle filtering (PF) is a sequential Monte Carlo method to sequential estimation of the posterior distribution of a nonlinear, non-Gaussian, dynamic system, using importance sampling techniques and the approximations of distributions with discrete random measures (Candy, 2009). PFs assume a state-space representation of the dynamic nonlinear system:

$$x_k = f(x_{k-1}, w_{k-1}) \tag{2.56}$$
$$y_k = g(x_k, v_k), \tag{2.57}$$

where x_k denote a n_x-dimensional system state vector with initial distribution $p(x_0)$ and transition probability $p(x_k|x_{k-1})$, y_k denote the n_y-dimensional conditionally independent noisy observations, and w_k and v_k denote independent non-Gaussian random variables.

The objective is to estimate the posterior distribution $p(x_k|y_{1:k})$. As this is a difficult task to achieve, estimators require the implementation of structures based on Bayes rule where, under Markovian assumptions, the filtering posterior distribution can be written as

$$p(x_k|y_{1:k}) = \frac{p(y_k|x_k)p(x_k|y_{1:k-1})}{p(y_k|y_{1:k-1})}. \tag{2.58}$$

The posterior distribution, $p(x_k|y_{1:k})$, is approximated by a collection of N_p weighted samples or particles $\{x_k^{(\mathrm{i})}, W_k^{(\mathrm{i})}\}_{\mathrm{i}=1}^{N_p}$, $\sum_{\mathrm{i}=1}^{N_p} W_k^{(\mathrm{i})} = 1$, such that:

$$\hat{p}(x_k|y_{1:k}) \approx \sum_{\mathrm{i}=1}^{N_p} W_k^{(\mathrm{i})} \delta_{x_k^{(\mathrm{i})}}(x_k) \tag{2.59}$$

The weighting process is performed by applying Sequential Importance Resampling (SIR) algorithms in two stages: Sequential Importance Sampling (SIS) and Resampling.

2.5.1.1 Sequential Importance Sampling

To mitigate difficulties with the inability to directly sample from a posterior distribution, Sequential Importance Sampling (SIS) draws samples from an alternative distribution called importance distribution, $\pi(\tilde{x}_k^{(\mathrm{i})}|\tilde{x}_{0:k-1}^{(\mathrm{i})}, y_{1:k})$, to be used to approximate a targeted (posterior) distribution by appropriate weighting (Candy, 2009). SIS proposes to update the weights of each particle as

$$w_k^{(\mathrm{i})} = W_{k-1}^{(\mathrm{i})} \frac{p(y_k|\tilde{x}_k^{(\mathrm{i})})p(\tilde{x}_k^{(\mathrm{i})}|\tilde{x}_{k-1}^{(\mathrm{i})})}{\pi(\tilde{x}_k^{(\mathrm{i})}|\tilde{x}_{0:k-1}^{(\mathrm{i})}, y_{1:k})} \tag{2.60}$$

where $\{\tilde{x}_k^{(\mathrm{i})}\}_{\mathrm{i}=1}^{N_p}$ is a set of N_p random samples drawn from $\pi(\cdot|\tilde{x}_{0:k-1}^{(\mathrm{i})}, y_{1:k})$. In addition, normalizing weights as follows

$$W_k^{(\mathrm{i})} = \frac{w_k^{(\mathrm{i})}}{\sum_{\mathrm{i}=1}^{N_p} w_k^{(\mathrm{i})}}, \tag{2.61}$$

the posterior distribution can be approximated by Eq. 2.59.

2.5.1.2 Resampling

Importance sampling algorithms have problems associated with the depletion of the particles. That is, the importance weights increases in time and most of the probability mass ends concentrating in only a few samples. This problem, known as sample degeneracy, is addressed by including a resampling step, leading to the Sequential Importance Resampling (SIR) algorithm. A measure of particle degeneracy is provided in terms of the effective particle sample size (Eq. 2.62).

$$\hat{N}_{eff}(k) = \frac{1}{\sum_{\mathrm{i}=1}^{N_p} (W_k^{(\mathrm{i})})^2} \tag{2.62}$$

Resampling involves sampling N_p-draws from the current population of particles using the normalized weights as selection probabilities. Particles of low probability are removed and those of high are retained and replicated (Candy, 2009). Resampling is applied if $\hat{N}_{eff} = N_{thres}$, with N_{thres} a fixed threshold.

2.5.2 Particle-filtering-based Prognostic

Prognosis schemes can be understood basically as the result of long-term predictions describing the evolution of a fault indicator, with the purpose of estimate the Remaining Useful Life (RUL) of a component or system, from the initial conditions given by the estimation step.

The prediction of critical events require the existence of at least one critical component that provides the severity of the studied condition. It is always possible to combine different characteristics to obtain one unique signal. Then, it is possible to describe the evolution in time of the dimension of the fault, which is associated to the observed degradation variable of the component, through non-linear state equations (Pola, 2014).

For the generation of long-term predictions, consider the τ-step prediction for the conditional state PDF $\hat{p}(x_{k+\tau}|y_{1:k})$ which describes the state distribution at the future instant $k+\tau$, $(\tau = 1, \ldots, m)$. With the assumption that the current particle population $\left\{x_k^{(\mathrm{i})}, w_k^{(\mathrm{i})}\right\}_{\mathrm{i}=1,\ldots,N}$ is a good representation of the state PDF at time k, then it is possible to approximate the predicted state PDF at time $k+\tau$, by sequentially applying the Chapman-Kolmogorov equation, as shown in Eq. (2.64), and then updating each particle by sampling from the transition kernel, where $u_{k+\tau}$ is the future exogenous input of the system at the τ-th prediction time.

$$p(x_{k+\tau}|y_{1:k}) \approx \hat{p}(x_{k+\tau}|y_{1:k}) \tag{2.63}$$

$$= \sum_{\mathrm{i}=1}^{N} p(x_{k+\tau}|x_{k+\tau-1}^{(\mathrm{i})}, u_{k+\tau-1})\hat{p}(x_{k+\tau-1}^{(\mathrm{i})}|y_{1:k}) \tag{2.64}$$

$$\approx \sum_{\mathrm{i}=1}^{N} w_k^{(\mathrm{i})} \delta_{x_{k+\tau}^{(\mathrm{i})}}(x_{k+\tau}). \tag{2.65}$$

In other words, a population of samples is obtained from the state posterior PDF at the beginning of prognostics. Then, each of them is used as initial condition for simulating state trajectories in "random walk" fashion iterating the state transition equation with random realizations of the process noise.

2.5.3 Probability of Failure in PF-based Prognostic Algorithms

In PF-based prognostic algorithms, the Time of Failure (ToF) (or EOD time for the case of BHM) estimates are computed using a set of N_p particles (each particle being a duple

$\{x_k^{(\mathrm{i})}, w_k^{(\mathrm{i})}\}$) such that

$$P(ToF \leq k) = \sum_{\mathrm{i}=1}^{N_p} w_k^{(\mathrm{i})} p(failure|X = x_k^{(\mathrm{i})}), \tag{2.66}$$

where $p(failure|X)$ corresponds to the probability of system failure, conditional to the value of the state vector $x \in \mathcal{R}^{n_x}$. Note that Eq. 2.66 is a particular case of

$$P(ToF \leq k) = \int_{\mathcal{R}^{n_x}} p(failure \mid x_k) p(x_k \mid y_{1:k_p}) \mathrm{d}x_k. \tag{2.67}$$

However, Acuña and Orchard (2017) state that this probability measure has been misinterpreted as a Cumulative Mass Function (CMF) and it is limited to cases of strictly degenerative systems. For the general case, Acuña and Orchard (2017), propose that this concept should be reinterpreted as a Probability Mass Function (PMF) as the probability measure for ToF is defined at discrete time instants.

According to Acuña and Orchard (2017), a failure event can be treated as a non-stationary Bernoulli stochastic process in which probabilities vary as the time evolves. Denoting healthy and faulty systems (at the $k-th$ time instant) by $\mathcal{F}_k$ and $\mathcal{H}_k$, respectively, it is possible to characterize the true Probability of Failure (PoF) at the $k-th$ time instant, $P(\mathcal{F}_k)$ as:

$$P(\mathcal{F}_k) = \frac{P(\mathcal{F}_k, \mathcal{H}_{k_p:k-1})}{P(\mathcal{H}_{k_p:k-1} \mid \mathcal{F}_k)}, \qquad \forall \quad k > k_p \tag{2.68}$$

since $P(\mathcal{H}_{k_p:k-1} \mid \mathcal{F}_k)$ corresponds to the probability of staying healthy until time $k-1$, given that the failure occurred at time k, it is important to note that $P(\mathcal{H}_{k_p:k-1} \mid \mathcal{F}_k) = 1$ (it is assumed that the system can only fail once).

Applying the definition of joint probability, Eq. 2.68 can be rewritten as:

$$P(\mathcal{F}_k) = P(\mathcal{F}_k|\mathcal{H}_{k_p:k-1}) P(\mathcal{H}_{k_p:k-1}), \qquad \forall \quad k > k_p \tag{2.69}$$

It is important to note that:

- $P(\mathcal{F}_k|\mathcal{H}_{k_p:k-1})$ corresponds to the failure probability measure that has been used in the literature so far, equivalent to the expression in Eq.2.70, i.e.,

$$P(\mathcal{F}_k|\mathcal{H}_{k_p:k-1}) = \int_{\mathcal{R}^{n_x}} p(failure \mid x_k) p(x_k \mid y_{1:k_p}) \mathrm{d}x_k \tag{2.70}$$

  Prognostic algorithms characterize $p(x_k|y_{1:k})$ by the propagation of uncertainty to future moments without considering any constraint other than the dynamics of the state. Indeed, when propagating the uncertainty one step ahead in the future, those algorithms implicitly assume that the system was healthy during the previous time instant.

- $P(\mathcal{H}_{k_p:k-1})$ is the probability that the system is healthy until the $(k-1)-th$ time instant. In consequence,

$$\begin{aligned} P(\mathcal{H}_{k_p:k-1}) &= P(\mathcal{H}_{k-1}|\mathcal{H}_{k_p:k-2})P(\mathcal{H}_{k_p:k-2}) \\ &= P(\mathcal{H}_{k-1}|\mathcal{H}_{k_p:k-2})P(\mathcal{H}_{k-2}|\mathcal{H}_{k_p:k-3})P(\mathcal{H}_{k_p:k-3}) \\ &\vdots \\ &= \prod_{j=k_p+1}^{k-1} P(\mathcal{H}_j|\mathcal{H}_{k_p:j-1}) \end{aligned} \tag{2.71}$$

  Then, as $P(\mathcal{H}_j|\mathcal{H}_{k_p:j-1}) = 1 - P(\mathcal{F}_j|\mathcal{H}_{k_p:j-1})$ and the failure is modelled through a Bernoulli stochastic process, it follows that:

$$P(\mathcal{H}_{k_p:k-1}) = \prod_{j=k_p+1}^{k-1} \big(1 - P(\mathcal{F}_j|\mathcal{H}_{k_p:j-1})\big) \tag{2.72}$$

Therefore, the failure probability described in Eq. 2.69 is defined as the product of $P(\mathcal{F}_k|\mathcal{H}_{k_p:k-1})$ and $P(\mathcal{H}_{k_p:k-1})$, where the first term corresponds to the likelihood of failure at $k-th$ time (assuming that the system was healthy for all previous moments). The second term indicates the probability that the system was actually healthy until the $(k-1)-th$ time instant.

2.6 Summary

From the literature review in this Chapter is important to highlight and conclude:

- BHM for rotary-wing UAVs arose as a little-explored research topic. Except for the work in (de Souza Candido et al., 2014) which is aimed at rotary-wing aircraft (although it is limited to numerical simulations and hovering flight), reported works in the literature on BMH for UAVs are aimed at fixed-wing aircraft.
- Although several battery models exist in literature at various levels of granularity and abstraction, such models are complex which might be impractical in real-time applications. Therefore, in BHM for electric UAVs, battery models at a high level of abstraction of the underlying physics has been used to predict the EOD event using a Bayesian framework. Considering the weight, size and cost constraints in small UAV, models at a high level of abstraction also seems suitable; however, efficiency might improve as the model is simplified.
- In recent years, there has been a growing interest in the use of Bayesian methods to estimate the SOC of Li-Ion batteries under randomly varying loading conditions, due to they can perform real-time estimations using online measurements. Particularly the family of sequential Monte Carlo (SMC) methods (also known as particle filters (PF)) have shown to be very effective in the process of incorporating model non-linearities, as well as complex forms of uncertainty in acquired measurements. Specifically, for the problem of BHM for UAV, particle filter-based method have been used with satisfactory results.

- A more sophisticated technique can improve the accuracy and precision of prediction. Therefore, the use of techniques that have arisen in the Bayesian prognostics framework, such as artificial evolution and Outer Feedback Correction Loops (OFCL) might provide improved prediction results for the EOD.
- A proper future load profile characterization leads to EOD predictions more accurate and more stable as well. Therefore, in the BHM problem for fixed-wing UAVs, the future load profile characterization has been addressed by establishing a mean current for each flight maneuver based on either historical data of typical flights or aerodynamic models. A PDF is defined around the current mean to characterize the uncertainty associated with unmodeled phenomena. However, previous works that addressing the flight time estimation problem in rotary-wing UAVs only use a characterization of the power required in hovering flight without considering other maneuvers, which is inaccurate and might cause a bias in the estimation of the flight time.
- The three major factors that affect the performance of rotary-wing UAVs are density altitude (air density in relation to altitude), weight, and wind. Therefore, a characterization of the power consumption in rotary-wing UAVs that incorporates these factors might provide improved prediction results for the EOD.
- In PF-based prognostic algorithms, the probability of failure measure has been misinterpreted as a Cumulative Mass Function (CMF), although it is not necessarily an increasing function of time (consider, for example, regenerative systems). Therefore, for the general case, a new definition of probability of failure has been recently proposed which states that a failure event can be treated as a non-stationary Bernoulli stochastic process.

With the above in mind, it has been proposed the prognostics framework for BHM systems in small-size electric multirotor that is described in Chapter 3.

Chapter 3

Prognostics Framework for BHM Systems in Small-size Electric Multirotors

3.1 Introduction

This study adopted a model-based prognostics architecture (Daigle and Goebel, 2013) where there is a system being monitored, and there is a model that describes how the system evolves in time in response to its inputs (Daigle, 2016a). The system model may generally be defined as

$$x(k+1) = f(k, x(k), \theta(k), u(k), v(k)), \tag{3.1}$$

$$y(k) = h(k, x(k), \theta(k), u(k), n(k)), \tag{3.2}$$

where k is the discrete time variable, $x(k) \in \mathbb{R}^{n_x}$ is the state vector, $\theta(k) \in \mathbb{R}^{n_\theta}$ is the unknown parameter vector, $u(k) \in \mathbb{R}^{n_u}$ is the input vector, $v(k) \in \mathbb{R}^{n_v}$ is the process noise vector, f is the state equation, $y(k) \in \mathbb{R}^{n_y}$ is the output vector, $n(k) \in \mathbb{R}^{n_n}$ is the measurement noise vector, and h is the output equation.

In prognostics, it is of interest to predict the occurrence of some event E that is defined concerning the states, parameters, and inputs of the system. The event is defined as the earliest instant that some event threshold T_E is reached. For batteries, it is of interest to predict the EOD, defined by a voltage threshold V_{EOD}. In this case, T_E is defined by $V < V_{EOD}$, that is, when the battery voltage is less than the cutoff voltage, EOD is reached.

The system model is used as the basis of two sequential problems, (i) the estimation problem, which requires determining a joint state-parameter estimate $p(x(k), \theta(k)|y(k_0 : k))$ based on the history of observations up to time k, $y(k_0 : k)$, and (ii) the prediction problem, which determines at k_P , using $p(x(k), \theta(k)|y(k_0 : k))$, a probability distribution $p(k_E(k_P)|y(k_0 : k_P))$. The distribution for Δk_E can be computed from $p(k_E(k_P)|y(k_0 : k_P))$ by subtracting k_P. The prognostics architecture is shown in Fig. 3.1. In discrete time k, the system is pro-

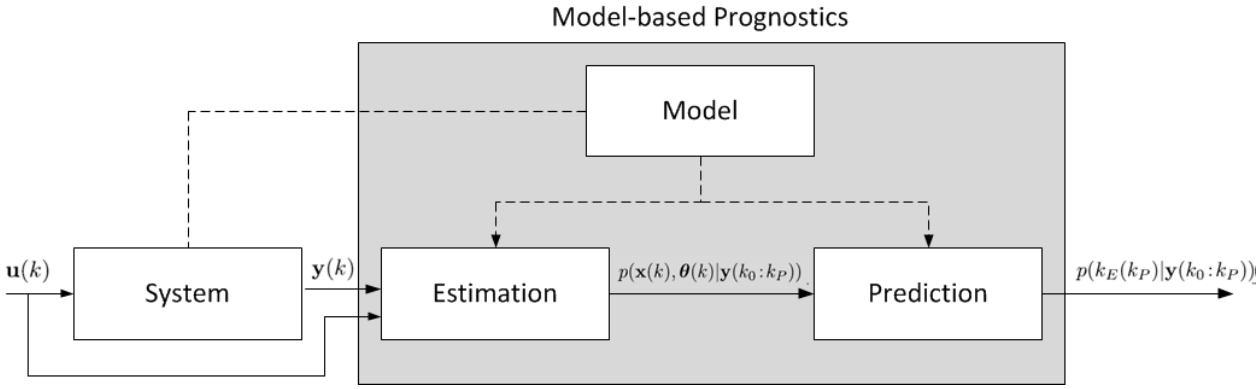

Figure 3.1: Model-based prognostics conceptual architecture.

vided with inputs u_k and provides measured outputs y_k. The estimation module uses this information, along with the system model, to compute an estimate $p(x(k), \theta(k)|y(k_0 : k))$. The prediction module uses the joint state-parameter distribution and the system model, along with hypothesized future inputs, to compute the probability distribution $p(k_E(k_P)|y(k_0 \colon k_P))$ at given prediction times k_P .

As indicated in the literature review, the problem of SOC estimation in Li-ion batteries has been typically solved by the implementation of Extended Kalman Filter (EKF), Unscented Kalman Filter (UKF), and Particle Filter (PF). The latter, mainly because these Bayesian processors are able to simultaneously perform real-time state and model parameter estimation when using the concept of artificial evolution (Liu and West, 2001; Orchard and Vachtsevanos, 2009). It should be mentioned that in theory, it is also possible to use Markov Chain Monte Carlo (MCMC) to determinate the joint state-parameter estimate (i.e., $p(x(k), \theta(k)|y(k_0 : k))$. However, MCMC is not well suited for real-time applications. Even for offline applications, MCMC may converge slowly if the model has strong dependencies or due to a strong correlation between θ and x (Fearnhead, 2008). In addition, because the distribution sampled in MCMC is invariant, MCMC methods are better suited to estimate the value of constant parameters.

From the literature review is also possible to conclude that in the prognostic and health management field, particularly PF has shown to be very effective in the process of incorporating model non-linearities, as well as complex forms of uncertainty in acquired measurements. Specifically, for the problem of BHM for UAV, in (de Souza Candido et al., 2014; Saha et al., 2011b, 2012), authors have used implementations of particle filter-based method with satisfactory results. Therefore, this study uses a Particle Filter as the estimation algorithm and a PF-based prognosis algorithm to propagate the particles until reaching the voltage threshold, V_{EOD}.

Also, several battery models with different levels of abstraction of the underlying phenomena were encountered from the literature review in the Chapter 2 about battery models for prognosis. For example, Daigle and Kulkarni (2013) developed an electrochemistry-based model of lithium-ion batteries that capture the significant electrochemical processes, while Pola et al. (2015) proposed an equivalent circuit model that incorporates most of the nonlinearities found in Li-Ion open-voltage discharge curves and captures battery internal resistance

drops without considering activation polarization nor concentration polarization phenomena. The use of both of them have shown to provide reasonable prognosis results; however, the first of them is computationally more complex than the second one, which is not suitable for small UAVs. Therefore, to reduce computational resources, in this study it is proposed:

1. A simplified equivalent circuit battery model that takes advantage of artificial evolution to estimate the battery internal resistance and the total energy delivered by the battery and that allows improving efficiency in prognostics. Such improvement of efficiency constitutes an advantage when it deals with constrained computing platforms that may encounter on small UAVs. Also, unlike previous research efforts (Pola et al., 2015), the parameterization proposed for the Open Circuit Voltage (OCV) curve provides a better curve fit for batteries of more than one cell.

When artificial evolution is used, the process noise should be large enough to allow finding the right value of the parameters. However, as process noise increases, the uncertainty on the state/parameter estimate increases as well, which affects the prediction results. Therefore, to take advantage of artificial evolution without losing accuracy in the prediction results, in this study it is proposed:

2. A novel Outer Feedback Correction Loop (OFCL) during the estimation stage which adjusts the variance of the process noise to diminish the bias in Bayesian state estimation. The proposed OFCL here is based on long-term results, but unlike previous OFCLs (Tampier et al., 2015), it implements a basic digital filter on the observation error instead of using the accumulated error to determine whether to increase or decrease the variance of the process noise, which solves the problems of previous OFCLs.

From the literature review presented in the Chapter 2, it is also possible to conclude that a proper future load profile characterization leads to EOD predictions more accurate and more stable. Also, density altitude (air density in relation to altitude) and weight were identified as the major factors that affect performance and power consumption in multirotors. Therefore, it is proposed:

3. A practical aerodynamic-based model of the power consumption in multirotors to define future power consumption profiles instead of using a large amount of flight data or flight simulations. The proposed model characterizes the power consumption in each stage of flight (unlike previous works (Gatti et al., 2015) that address the flight time estimation problem assuming that aircraft is in hovering flight condition during the entire flight), that is, climb, hovering flight, horizontal flight, and descent, as a function of the weight, air density, translational speed and disc actuator area.

Finally, in PF-based prognostic algorithms, the Time of Failure (ToF) (or EOD time for the case of BHM) estimates have been computed conventionally using a set of N_p particles (each particle being a duple $\{x_k^{(\mathrm{i})}, w_k^{(\mathrm{i})}\}$) such that

$$\mathcal{P}(ToF \leq k) = \sum_{\mathrm{i}=1}^{N_p} w_k^{(\mathrm{i})} p(failure | X = x_k^{(\mathrm{i})}), \tag{3.3}$$

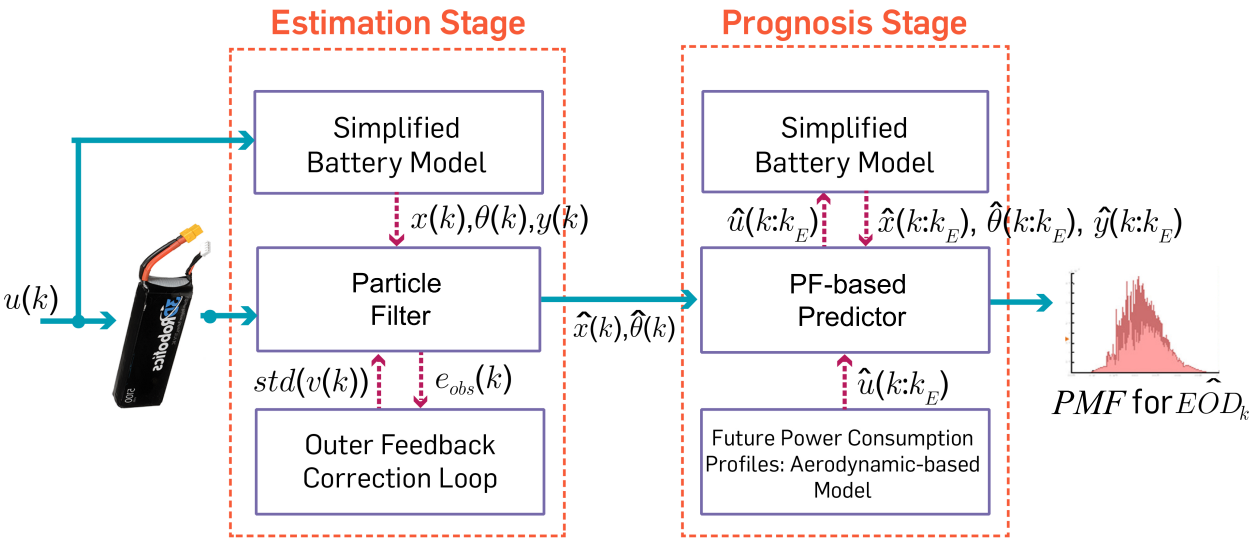

Figure 3.2: Framework outline

where $p(failure|X)$ corresponds to the probability of system failure, conditional to the value of the state vector $x \in \mathcal{R}^{n_x}$.

However, this probability measure has been misinterpreted as a Cumulative Mass Function (CMF), although it is not necessarily an increasing function of time (consider, for example, regenerative systems). PHM researchers have not detected this issue because simulations typically show that $\mathcal{P}(ToF \leq k)$ increases (apparently) monotonically in time. In contrast, the definition of Probability of Failure (PoF) by (Acuña and Orchard, 2017) is guaranteed to be a cumulative mass function. In addition, although both expressions represent the probability of failure in the future, the conventional expression (Eq. 3.3) accounts for the probability of failure conditional to the fact that the system did not undergo a catastrophic failure at time instants prior to $k > k_P$, whereas the expression by (Acuña and Orchard, 2017) characterizes the probability of experiencing a single catastrophic failure event either at the time instant k or previous to the time instant k (Acuña and Orchard, 2018). Also, the definition by (Acuña and Orchard, 2017) does not attempt to provide an estimate for the failure time (or EOD time in this case) but it accounts for the risk at the failure time, which is more suitable to make decisions about the flight. Therefore:

4. This thesis uses the definition of Probability of Failure (PoF) proposed by Acuña and Orchard (2017), which corrects the expression used for the computation of the Time-of-Failure (ToF) probability mass function in the context of online monitoring schemes. In addition, its effects on prediction results are evaluated concerning the use of the conventional definition of PoF. Also, it is proposed the use this new PoF as a method to mitigate the risk of the mission since the EOD PMF experiences a shift to the left (i.e., EOD characterization is more conservative) that is related to the uncertainty in the prediction of the SOC.

Finally, the framework outline of this thesis is shown in Fig. 3.2.

The remaining of this chapter is organized as follows. Section 3.2 presents the suggested

state-space model for batteries and its validation. Section 3.3 describes the novel OFCL. Section 3.4 deals with the problem of characterizing future power profiles using an aerodynamic-based model, and Section 3.5 describes the new definition of failure probability by (Acuña and Orchard, 2017) and its expected effects on probability mass function under different flight missions. Finally, in Section 3.6 a summary of the chapter is made.

3.2 State-Space Model For State-Of-Charge Estimation In Batteries

The proposed empirical state-space model is inspired by equivalent electric circuits for a battery cell. Previous research efforts have also used a state-space representation to describe the SOC evolution in time (Pola et al., 2015), although the parameterization that is proposed for the Open Circuit Voltage (OCV) curve is insufficient for batteries of more than one cell.

On the other hand, battery performance is strongly determined by characteristics such as temperature or current discharge rate, which affect battery internal impedance and the total energy that the battery can deliver. In addition, battery internal impedance varies as a function of the State of Charge (SOC) (Burgos-Mellado et al., 2016). Therefore, in order to incorporate the current load dependence, temperature dependence, and SOC dependence; the proposed model uses the concept of artificial evolution (Liu and West, 2001; Orchard and Vachtsevanos, 2009) to estimate the absolute value of the battery internal impedance and the total energy delivered by the battery. This concept is implemented by extending the dimension of the state vector and associating its first component with the value of this time-varying parameter.

The model (Eq.3.4- Eq.3.7) assumes a discrete characterization of the dynamics of the battery, and the availability (in real time) of voltage and current measurements. The model structure provides a modification to the observation equation that incorporates most of the nonlinearities found in OCV discharge curves, while simultaneously enabling the implementation of reliable off-line estimation procedures for the estimation of its parameters.

State transition model:

$$R_{int}(k+1) = R_{int}(k) + w_1(k) \tag{3.4}$$

$$SOC(k+1) = SOC(k) - P(k) \cdot \Delta t \cdot E_{crit}(k)^{-1} + w_2(k) \tag{3.5}$$

$$E_{crit}(k+1) = E_{crit}(k) + w_3(k) \tag{3.6}$$

Measurement equation:

$$V(k) = v_{oc}(k) - \mathrm{i}(k) \cdot R_{int}(k) + \eta(k), \tag{3.7}$$

where:

$$v_{oc}(k) = v_L + \lambda \cdot \mathrm{e}^{\gamma \cdot SOC(k)} - \mu \cdot \mathrm{e}^{-\beta\sqrt{SOC(k)}} \tag{3.8}$$

$$\mathrm{i}(k) = \frac{v_{oc}(k) - \sqrt{v_{oc}(k)^2 - 4 \cdot R_{int}(k) \cdot P(k)}}{2 \cdot R_{int}(k)}. \tag{3.9}$$

The power $P(k)$ (measured in Watts), and the sample time Δt (measured in seconds) are input variables (i.e., the input vector, $u(k)$), and the battery voltage $V(k)$ (measured in Volts) is the system output (i.e.,the output vector, $y(k)$). v_{oc} is the OCV (measured in Volts) and $\mathrm{i}(k)$ is the discharge current (measured in Amps), which is calculated by solving the quadratic equation:

$$\mathrm{i}(k) = \frac{P(k)}{v_{oc}(k) - \mathrm{i}(k) \cdot R_{\mathrm{int}}(k)} \tag{3.10}$$

$$0 = R_{\mathrm{int}}(k) \cdot \mathrm{i}(k)^2 - v_{oc}(k) \cdot \mathrm{i}(k) + P(k). \tag{3.11}$$

The parameters are defined as $R_{\mathrm{int}}(k)$, the internal resistance, and $E_{crit}(k)$, the expected total energy delivered by the battery (i.e., the unknown parameter vector, $\theta(k)$). The only state, $SOC(k)$, the State of Charge, is defined as the remaining battery energy normalized by E_{crit} (i.e., the state vector, $x(k)$). Process (w_1, w_2 and w_3) and measurement (η) noises (i.e., the process noise vector $v(k)$ and measurement noise vector $n(k)$) are assumed Gaussian. It is important to mention that process noise w_2 is correlated with η, the measurement noise, because the evolution in time of state $SOC(k)$ depends on voltage measurements. The quantities v_L, λ, γ, β, and μ are model parameters to be estimated off-line. The initial SOC, $SOC(k_0)$, is suggested to be estimated before starting the discharge by measuring the OCV and computing the inverse of the Eq. 3.8.

The procedure to estimate the parameters is a curve fitting between the measured voltage during discharge at a variable current and the voltage obtained with the model, as shown in Fig. 3.3. Since the internal resistance is assumed to be constant without considering SOC dependence, the curve fitting at the beginning of the discharge cycle (when the internal resistance should be larger) is less accurate. Nevertheless, the value estimated off-line provides an average value of the internal resistance for different values of load current. The parameters found are shown in Table 3.1 which correspond to a 3S 5100mAh Li-Po battery. The model is validated for 1C, 3C, and 4C rate discharges as shown in Fig. 3.4.

3.3 Outer Feedback Correction Loop

Using the concept of *artificial evolution* in conjunction with Bayesian methods provides the mechanism for generating new parameter (e.g., the battery internal impedance) values at each time step by adding additional random disturbances to sampled state vectors, which has proved to be efficient because it incorporates the effect of environmental factors (e.g., temperature, or battery degradation and age). In other words, artificial evolution allows incorporating effects on the battery performance that are not directly included in the model. However, the process noise should be large enough to allow finding the right value of the parameters. Nevertheless, as process noise increases, the uncertainty on the state/parameter estimate increases as well, which affects the prediction results. Therefore, an Outer Feedback Correction Loop (OFCL) is proposed to increase the process noise when detecting inconsistencies between measurements and estimations of the output (i.e., observation error), and

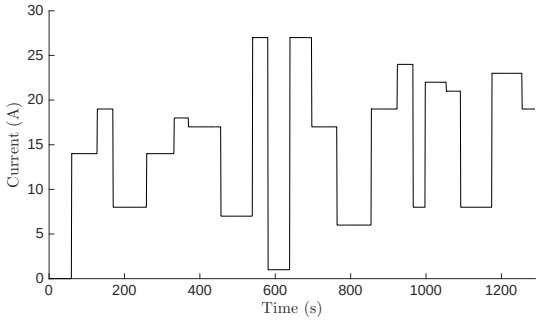

(a) Current

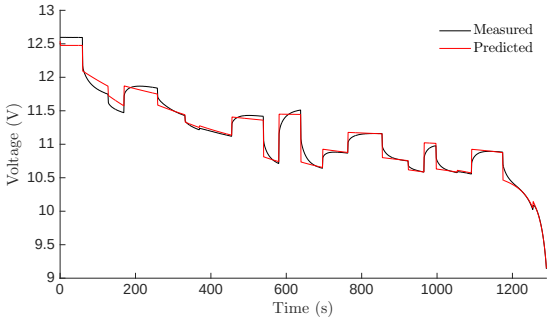

(b) Measured and predicted variable loading discharge curves.

Figure 3.3: Off-line estimation of the model parameters. Curve fitting for a variable current.

Table 3.1: Equivalent Circuit Model Parameters for a 3S 5100mAh Li-Po Battery.

Parameter	**Symbol**	**Value**
Battery model parameter	β	8.482
Battery model parameter	γ	3.355
Battery model parameter	λ	0.046
Battery model parameter	μ	2.759
Battery model parameter	v_L	11.148
Initial total energy (J)	$E_{crit}(k_0)$	202426.858
Initial Internal resistance (Ω)	$R_{int}(k_0)$	0.027
Sample time (s)	Δt	1
Process noise covariance matrix	R_{ww}	$\begin{bmatrix} 1.2 \cdot 10^{-7} & 0 & 0 \\ 0 & 1.163 \cdot 10^{-7} & 0 \\ 0 & 0 & 176.3 \end{bmatrix}$
Observation noise covariance	R_{vv}	1.1^{-3}

to decrease the process noise otherwise. That is, the process noise is increased when the parameters need to be re-estimated (e.g., during a drastic change in the load current) and it is decreased when the parameters have reached the new correct value.

Previous OFCLs (Tampier et al., 2015) use the observation error in earlier time horizons to determine whether to increase or decrease the variance of the process noise. However,

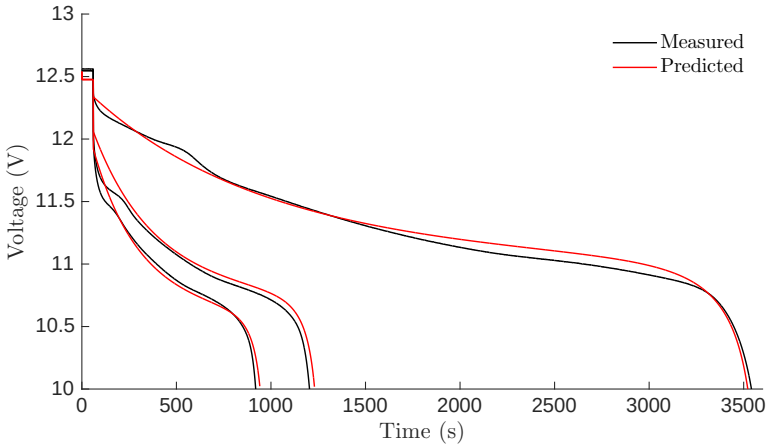

Figure 3.4: Model validation. Measured and predicted 1C, 3C and 4C rate discharge curves.

the voltage in the battery does not have considerable variations in small intervals of time (less than 30 seconds) during almost all the discharge cycle. Even more, the typical voltage drop that the battery undergoes during small time intervals, due to changes in the SOC, is comparable to the observation noise. In this regard, short-term predictions are not enough to evaluate the performance of the model and increasing the time horizon is not a practical answer to this issue, since this generates delays and requires more memory. The OFCL by (Tampier et al., 2015) (Alg. 3.1) uses the accumulated observation error to solve the problem related to the required memory space; but its effective increase of the variance is insufficient. Also, it makes unnecessary increases in the variance under large instantaneous observation errors.

1: **if** $t > t_{min}$ **then**
2: $\quad \mathrm{e}_{acum} = \mathrm{e}_{acum} + |\mathrm{e}_{obs}|$
3: $\quad$ **if** $\mathrm{e}_{acum} \leq \mathrm{e}_{th}$ **then**
4: $\quad\quad std(w_{\mathrm{i}}(t)) = max(p_{\mathrm{i}} \cdot std(w_{\mathrm{i}}(t)), std_{\mathrm{i}})$
5: $\quad$ **else**
6: $\quad\quad \mathrm{e}_{acum} = 0$
7: $\quad\quad std(w_{\mathrm{i}}(t)) = q_{\mathrm{i}} \cdot std(w_{\mathrm{i}}(t))$
8: $\quad$ **end if**
9: **end if**

Algorithm 3.1: Outer Feedback Correction Loop (OFCL) by (Tampier et al., 2015).

Therefore, the proposed OFCL here is based on long-term results, but instead of using the accumulated error, it uses a metric inspired by congestion control and Active Queue Management (AQM) techniques for IP networks. Similar to the problem we are dealing with here, it is not convenient in IP networks to make decisions about packet drop based on short-term behaviour of the queue size in the server, because the queue size is fluctuating and is subject to several sources of uncertainties, such as the occurrence of packet arrivals to the queue, the number of traffic sources, the type of traffic (continuous or burst), among others.

In particular, this new OFCL uses the metric defined in (Cisco Systems, Inc, 2014) for *Cisco Systems* equipments as shown in Alg. 3.2, where n is the exponential weight factor, a

user-configurable value. For high values of n, the previous average becomes more important. If the value of n gets too high, the OFCL will not react to large observation errors. The standard deviation of the process noise will be affected only in decreasing order. For low values of n, the average error closely tracks the current observation error. If the value of n gets too low, the OFCL will overreact to large instantaneous observation errors and unnecessarily will increase the standard deviation of the process noise. In other words, this algorithm implements a basic digital filter on the observation error. See Fig. 3.5.

$\mathrm{e}_{avg} = \mathrm{e}_{avg} \cdot \left(1 - \frac{1}{2^n}\right) + |\mathrm{e}_{obs}| \cdot \frac{1}{2^n}$
if $\mathrm{e}_{avg} \leq \mathrm{e}_{thr}$ **then**
    $std(w_{\mathrm{i}}(k)) = max(p_{\mathrm{i}} \cdot std(w_{\mathrm{i}}(k)), \mathrm{std}_{min_{\mathrm{i}}})$
else
    $std(w_{\mathrm{i}}(k)) = min(q_{\mathrm{i}} \cdot std(w_{\mathrm{i}}(k)), \mathrm{std}_{max_{\mathrm{i}}})$
end if

Algorithm 3.2: Novel Outer Feedback Correction Loop (OFCL).

e_{obs} is the observation error (the difference between the acquired measurement for the output and the one expected by the estimation algorithm), e_{avg} is a weighted average of the previous observation errors, with initial value of zero, e_{th} is the decision threshold to modify the process noise. If average error is lower than the threshold, the standard deviation of the process noise is reduced, but if it is larger than the threshold, it increases. Also p_{i} are constants with values between 0 and 1 for the i^{th} state/parameter, while q_{i} are constants bigger than 1. Finally, $\mathrm{std}_{min_{\mathrm{i}}}$ are the lower bounds which indicate the minimum standard deviation value accepted, and $\mathrm{std}_{max_{\mathrm{i}}}$ are the upper bounds which indicate the maximum standard deviation value accepted.

This OFCL does not require additional memory space, neither a minimum time for starting to operate (unlike the OFCL by Tampier et al. (2015)), since the standard deviation of the process noise only is decremented if the average error is less than the decision threshold. In the case of wrong initializations of the states, the average observation error will be above the threshold, and consequently, the standard deviation of the process noise will be increased. This latter allows the states converge to the right value. If the initialization is right, the initial average error does not exceed the threshold, and the standard deviation begins to decrease. An OFCL operating from the beginning of the estimation process allows earlier corrections than an OFCL that requires a minimum time for starting running.

On the other hand, the OFCL by (Tampier et al., 2015) makes unnecessary increases in the standard deviation of the process noise. The accumulated observation error frequently reaches the threshold, causing an increase in the standard deviation of the process noise, even when the observation error remains at acceptable values. The OFCL proposed solves this problem and also avoids overreacting to large instantaneous observation errors if the value of n is correctly configured.

In addition, The OFCL by (Tampier et al., 2015) increases the standard deviation of the process noise only at the instant when the accumulated error reaches the threshold. When this happens, the accumulated error is set to zero, which means that in the next time step the accumulated error could be less than the threshold and the standard deviation could

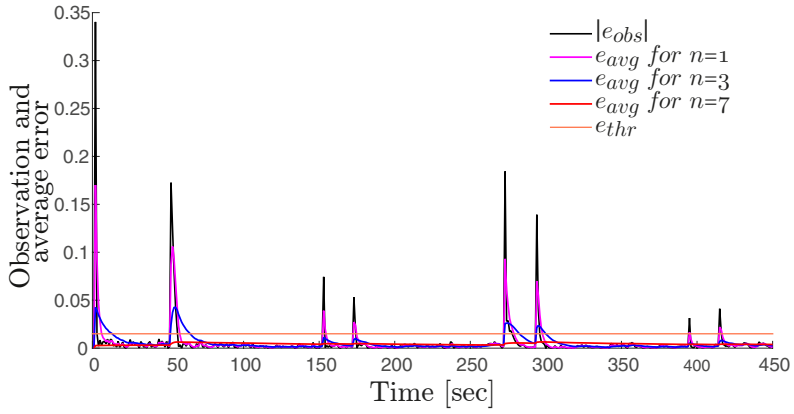

(a)

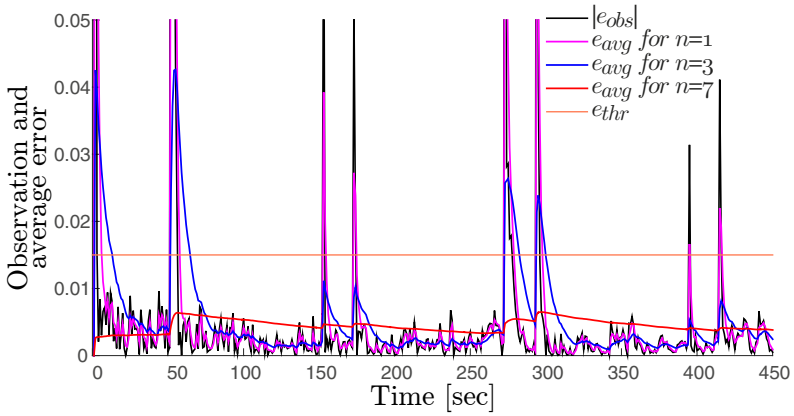

(b)

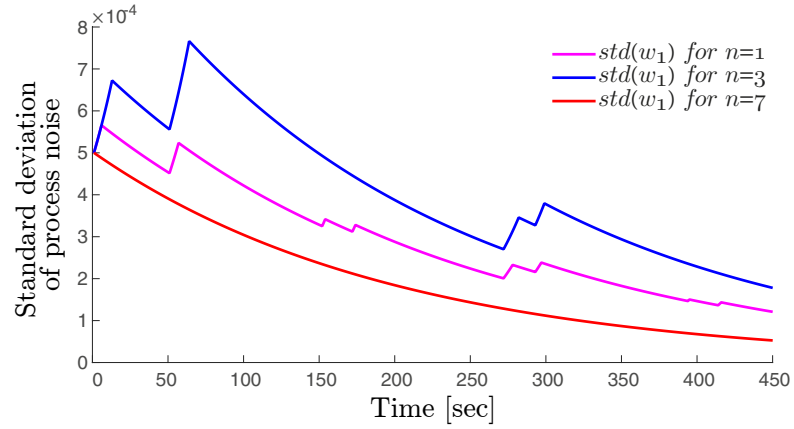

(c)

Figure 3.5: Exemplification of the dynamics of the new OFCL for different values of n. (a) Absolute value of the current observation error and average observation error. (b) Wider view of the absolute value of the current observation error and average observation error. (c) Evolution of the standard deviation of the process noise over time.

Figure 3.6: Multi-rotor platform used for validation. 3DR IRIS+ Quadcopter (3DR, 2013)

decline quickly again. Namely, the effective increase of the deviation may not be sufficient. The proposed OFCL solves this problem as well. Note that the longer the period where the observation error is above the threshold, the higher the increase in the process noise. This latter seeks that the effective increase of the deviation is sufficient to ensure convergence.

Finally, with the proposed OFCL, the decision threshold can be defined to be equal to or less than the standard deviation of the observation noise.

3.4 Approximate Power Consumption Model for Rotary-wing Aircraft

The ideal power consumption is characterized through a rough model based on aerodynamic equations for each flight maneuver (climb, hover, horizontal flight and descent). The aerodynamic-based model determined in this work is based on momentum theory (Stepniewski, 1979), which uses the simplest model of thrust generation (See Appendix A). Therefore, it is an approximate model that provides a practical way to calculate the ideal power consumption for a flight plan previously known, as a function of the weight, disc actuator area, air density, translational speed and the type of maneuver. The temperature effects are indirectly included in the air density, the humidity effects are not considered, and also it is assumed that the wind speed is moderate.

According to (Stepniewski, 1979), the ideal power required by a rotary-wing aircraft with a single rotor (helicopter) in hovering, is given by:

$$P_{\mathrm{id}_h} = \frac{W^{3/2}}{\sqrt{2A\rho}}, \tag{3.12}$$

where ρ is air density, W is the total weight of the aircraft equal to the empty-operative weight W_0 plus the payload weight W_p,A is the total actuator disc area; namely, πR^2, where R is the rotor or slipstream radius. The parameter values for the multi-rotor platform used for validation, namely, a 3DR IRIS+ quadcopter (Fig. 3.6) are summarized in the Table 3.2.

To extend the Eq. 3.12 to n-rotors, (Gatti et al., 2015) assumes that the total weight is equally distributed on n-rotors, and that A_t is the sum of the n-disc areas. Taking the preceding assumptions, and based on the equations in (Stepniewski, 1979), this work here

Table 3.2: Multi-rotor Parameters.

Parameter	**Symbol**	**Value**	**Units**
Number of rotors	n	4	
Propeller diameter	D_p	0.2413	m
Total disc area	A_t	0.1829	m^2
Empty mass	m_0	1.357	kg
Maximum payload mass	m_{pmax}	0.3	kg
Empty weight	W_0	13.2986	N
Maximum payload weight	W_{pmax}	2.94	N
Air density	ρ	1.15	kg/m^3

proposes the following equations for the power required by rotary-wing aircraft with n-rotors, in hovering P_h flight, climb P_c, and descent P_d:

$$P_h = \frac{W^{3/2}}{\eta_h \cdot \sqrt{2\rho A_t}}, \tag{3.13}$$

$$P_c = \frac{W}{\eta_c(V_c)} \left(\frac{V_c}{2} + \sqrt{\frac{V_c^2}{4} + \frac{W}{2\rho A_t}} \right), \tag{3.14}$$

$$P_\mathrm{d} = \frac{W}{\eta_\mathrm{d}(V_\mathrm{d})} \left(\frac{-V_\mathrm{d}}{2} + \sqrt{\frac{V_\mathrm{d}^2}{4} + \frac{W}{2\rho A_t}} \right), \tag{3.15}$$

where V_c is the vertical climb speed, V_d is the vertical descent speed, and η is the efficiency factor of the propulsion system (electric speed controller (ESC), motors, propellers), which slowly varies as a function of the rotor thrust, among other factors. This work defines η_c, the efficiency factor in climb, and η_d, the efficiency factor in descent, as functions of the climb speed and descent speed respectively. The following curves for the efficiency factors are proposed:

$$\eta_c(V_c) = c_0 + c_1 \cdot \cos(V_c \cdot c_2) + c_3 \cdot \sin(V_c \cdot c_2) \tag{3.16}$$

$$\eta_\mathrm{d}(V_\mathrm{d}) = \mathrm{d}_0 \cdot \exp(V_\mathrm{d} \cdot \mathrm{d}_1) + \mathrm{d}_2 \cdot \exp(V_\mathrm{d} \cdot \mathrm{d}_3). \tag{3.17}$$

The parameters of the above curves (see Table 3.3) are computed by a curve fitting with the power consumed in climb and descent by the quadcopter without payload at different speeds. Then, equations 3.13, 3.14, 3.15 are validated for $m_p = 100gr$ and $m_p = 200gr$ as shown in Fig. 3.7 and Fig. 3.8.

For the horizontal flight case, another assumption is made for simplification: The rotor tilt, a_v, required in steady flight at low velocities is assumed to be negligible such that $a_v \approx 0$

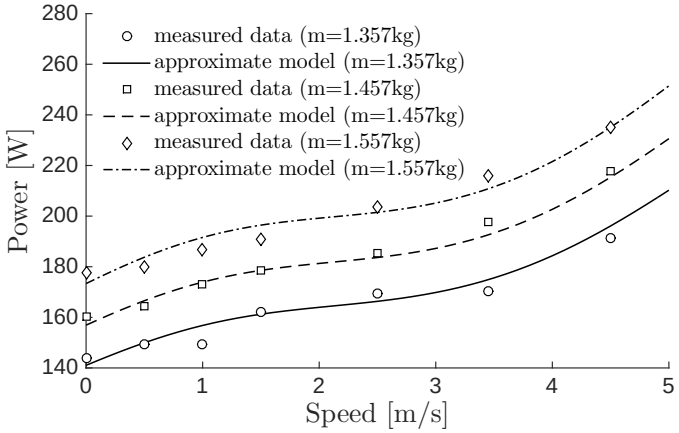

Figure 3.7: Power required in climb.

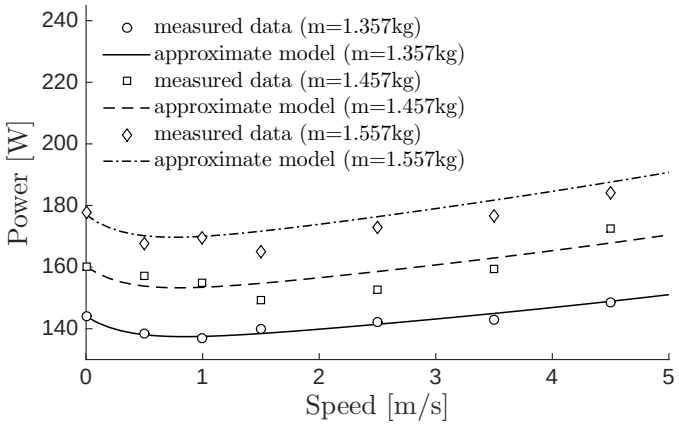

Figure 3.8: Power required in descent.

and $T \approx W$ (See Fig. A.3). The average maximum speed of a small-size multirotor is about $15m/s$, and several applications just need speeds up to $5m/s$. For example, in land surveys, the usual speed in forward flight is set to $3m/s$ so that the aerial photos taken are not blurry. With this in mind, the assumptions above are sufficient.

Since $T \approx W$, the power required in horizontal flight, P_{hor}, where $a_v = a \approx 0$, for a rotary-wing aircraft moving in the gravitational coordinate system at a velocity of flight V_{hor}, is roughly given by:

$$P_{hor} = \frac{W}{\eta_{hor}(V_{hor})} \left(V_{hor} \sin(a_v(V_{hor})) + v_{hor} \right), \tag{3.18}$$

where v_{hor}, the induced velocity in horizontal flight, is given by:

$$v_{hor} = \sqrt{-\frac{V_{hor}^2}{2} + \sqrt{\frac{V_{hor}^4}{4} + \left(\frac{W}{2\rho A_t} \right)^2}}. \tag{3.19}$$

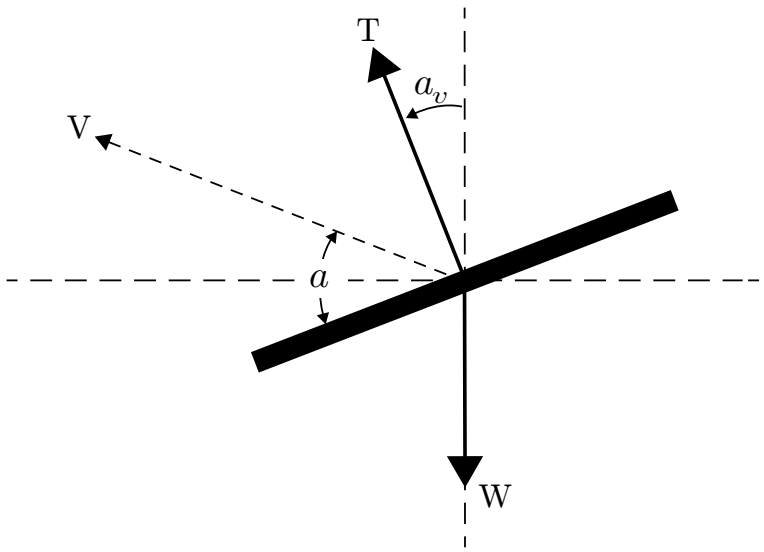

Figure 3.9: Rotary-wing aircraft in forward flight.

Table 3.3: Parameters of fitted curves.

i	a_i	b_i	c_i	$\mathrm{d_i}$
0	0.07842	0.5	0.5493	0.5591
1	1.189	0.02347	−0.01917	−0.1106
2	−0.06359	0.4004	1.127	−0.03985
3	0.004595	0.0136	−0.02208	−2.577

The angle-of-attack, a_v, and the efficiency factor in horizontal flight, η_{hor}, are proposed to be modeled as a function of the translational speed as described by Eq. 3.20 and Eq. 3.21, respectively. The parameters of the curves proposed (see Table 3.3) for horizontal flight are estimated by a curve fitting (Fig. 3.10 and Fig. 3.11) using the measured angle-of-attack and the measured values of the power consumed by the quadcopter without payload at different speeds. Then, Eq. 3.18 is validated for $m_p = 100gr$ and $m_p = 200gr$ as shown in Fig. 3.12.

$$a_v(V_{hor}) = a_0 + a_1 \cdot V_{hor} + a_2 \cdot V_{hor}^2 + a_3 \cdot V_{hor}^3 \tag{3.20}$$

$$\eta_{hor}(V_{hor}) = b_0 + b_1 \cdot \cos(V_{hor} \cdot b_2) + b_3 \cdot \sin(V_{hor} \cdot b_2) \tag{3.21}$$

3.5 Definition of Probability of Failure as Risk Mitigation Method

According to (Acuña and Orchard, 2017), a failure event can be treated as a non-stationary Bernoulli stochastic process in which probabilities vary as the time evolves. Denoting healthy and faulty systems (at the $k-th$ time instant) by $\mathcal{F}_k$ and $\mathcal{H}_k$, respectively, it is possible to

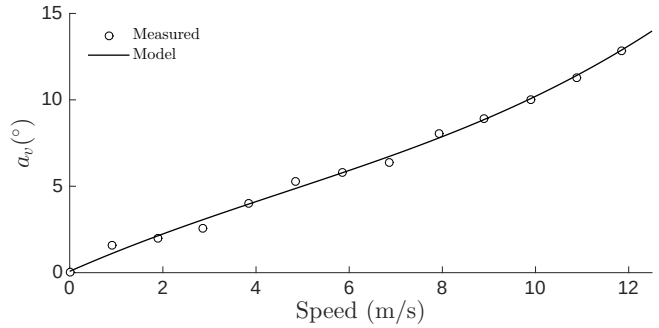

Figure 3.10: Angle-of-attack in horizontal flight.

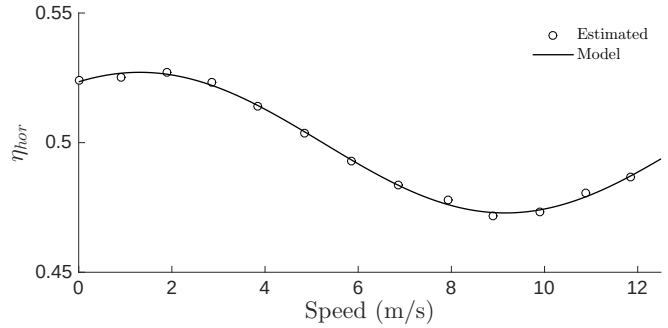

Figure 3.11: Efficiency factor in horizontal flight.

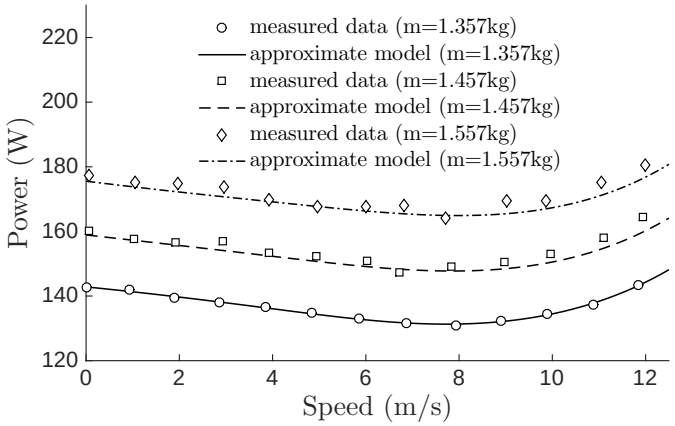

Figure 3.12: Power required in horizontal flight.

characterize the true Probability of Failure (PoF) at the $k-th$ time instant, $P(\mathcal{F}_k)$ as:

$$P(\mathcal{F}_k) = \frac{P(\mathcal{F}_k, \mathcal{H}_{k_p:k-1})}{P(\mathcal{H}_{k_p:k-1} \mid \mathcal{F}_k)}, \qquad \forall \quad k > k_p. \tag{3.22}$$

Since $P(\mathcal{H}_{k_p:k-1} \mid \mathcal{F}_k)$ corresponds to the probability of staying healthy until time $k-1$, given that the failure occurred at time k, it is important to note that $P(\mathcal{H}_{k_p:k-1} \mid \mathcal{F}_k) = 1$ (it is assumed that the system can only fail once).

Applying the definition of joint probability, Eq. 3.22 can be rewritten as:

$$P(\mathcal{F}_k) = P(\mathcal{F}_k|\mathcal{H}_{k_p:k-1})P(\mathcal{H}_{k_p:k-1}), \qquad \forall \quad k > k_p. \tag{3.23}$$

It is important to note that:

- $P(\mathcal{F}_k|\mathcal{H}_{k_p:k-1})$ corresponds to the failure probability measure that has been used in the literature so far, equivalent to the expression in Eq.3.24, i.e.,

$$P(\mathcal{F}_k|\mathcal{H}_{k_p:k-1}) = \int_{\mathcal{R}^{n_x}} p(failure \mid x_k)p(x_k \mid y_{1:k_p})\mathrm{d}x_k. \tag{3.24}$$

  Prognostic algorithms characterize $p(x_k|y_{1:k})$ by the propagation of uncertainty to future moments without considering any constraint other than the dynamics of the state. Indeed, when propagating the uncertainty one step ahead in the future, those algorithms implicitly assume that the system was healthy during the previous time instant.
- $P(\mathcal{H}_{k_p:k-1})$ is the probability that the system is healthy until the $(k-1)-th$ time instant. In consequence,

$$\begin{aligned} P(\mathcal{H}_{k_p:k-1}) &= P(\mathcal{H}_{k-1}|\mathcal{H}_{k_p:k-2})P(\mathcal{H}_{k_p:k-2}) \\ &= P(\mathcal{H}_{k-1}|\mathcal{H}_{k_p:k-2})P(\mathcal{H}_{k-2}|\mathcal{H}_{k_p:k-3})P(\mathcal{H}_{k_p:k-3}) \\ &\vdots \\ &= \prod_{j=k_p+1}^{k-1} P(\mathcal{H}_j|\mathcal{H}_{k_p:j-1}). \end{aligned} \tag{3.25}$$

  Then, as $P(\mathcal{H}_j|\mathcal{H}_{k_p:j-1}) = 1 - P(\mathcal{F}_j|\mathcal{H}_{k_p:j-1})$ and the failure is modelled through a Bernoulli stochastic process, it follows that:

$$P(\mathcal{H}_{k_p:k-1}) = \prod_{j=k_p+1}^{k-1} \left(1 - P(\mathcal{F}_j|\mathcal{H}_{k_p:j-1})\right). \tag{3.26}$$

Therefore, the failure probability described in Eq. 3.23 is defined as the product of $P(\mathcal{F}_k|\mathcal{H}_{k_p:k-1})$ and $P(\mathcal{H}_{k_p:k-1})$, where the first term corresponds to the likelihood of failure at $k-th$ time (assuming that the system was healthy for all previous moments). The second term indicates the probability that the system was actually healthy until the $(k-1)-th$ time instant.

In particular, for batteries we are interested in predicting the EOD time, that is, the time instant when the battery voltage is less than the voltage threshold, V_{EOD}. Conventionally, the probability of failure at any future time instant $k = \mathrm{eod}$ (namely the EOD probability distribution) is given by the expression in Eq. 2.66, that is:

$$P(\mathcal{F}_{\mathrm{eod}}|\mathcal{H}_{k_p:\mathrm{eod}-1}) = \sum_{\mathrm{i}=1}^{N_p} w_{\mathrm{eod}}^{(\mathrm{i})} p(failure|X = x_{\mathrm{eod}}^{(\mathrm{i})}). \tag{3.27}$$

However, since the definition of PoF by (Acuña and Orchard, 2017) provides a correction to the conventional expression (Eq. 2.66), the expression in Eq. 3.23 is used instead, namely:

$$P(\mathcal{F}_{\text{eod}}) = P(\mathcal{F}_{\text{eod}}|\mathcal{H}_{k_p:\text{eod}-1})P(\mathcal{H}_{k_p:\text{eod}-1}), \tag{3.28}$$

where it is assumed that each particle represents a fault condition when its realization for the output voltage is lower than the voltage threshold, V_{EOD}. The first term corresponds to Eq. 3.27, while the second term follows the expression in Eq. 3.26, that is:

$$P(\mathcal{H}_{k_p:\text{eod}-1}) = \prod_{j=k_p+1}^{\text{eod}-1} \left(1 - P(\mathcal{F}_j|\mathcal{H}_{k_p:j-1})\right). \tag{3.29}$$

The second term decreases from one to zero as particles reach the voltage threshold. Consequently, when it is multiplied by the conventional definition of failure probability, $P(\mathcal{F}_k|\mathcal{H}_{k_p:k-1})$, the EOD PMF experiments a shift to the left (i.e., to an earlier time). However, the magnitude of this shift has not been evaluated for different prediction horizons. Therefore, in Chapter 4, the shift experimented by the predicted mean EOD is measured as the time of prediction approaches the time of failure.

In addition, this work states that the definition by (Acuña and Orchard, 2017) provides a mechanism to mitigate the risk since the magnitude of the shift is related to the magnitude of the uncertainty involved in the mission (as shown in Chapter 4). The greater the uncertainty on the predicted EOD, the larger the shift to the left. Namely, the predicted EOD time is shown to be more conservative when the risk is higher. To demonstrate the above, in Chapter 4 the magnitude of such a shift is also evaluated for different levels of uncertainty on the future inputs.

3.6 Summary

In this Chapter, the prognostics framework for BHM systems in small-size electric multirotors has been introduced. With this purpose, the model-based prognostics architecture adopted for the development of this study is described. Then, a simplified equivalent circuit model is proposed as the base of the prognostics architecture in order to reduce computational resources. The proposed battery model takes advantage of the concept of artificial evolution to estimate the battery internal resistance and the total energy delivered by the battery.

In addition, in order to take advantage of artificial evolution without losing accuracy in the prediction results, a novel Outer Feedback Correction Loop (OFCL) during the estimation stage is proposed which adjusts the variance of the process noise to diminish the bias in Bayesian state estimation.

Besides, since prediction results depend on the estimated states because they are the initial states of the prediction stage, but they also depend on the future profile of discharge, a practical aerodynamic-based model of the power consumption in multirotors is proposed and validated to define future power consumption profiles used during the prediction stage.

Finally, considering the catastrophic consequences that may result from accidental battery run-down during the flight, it is proposed to use the new definition of probability of failure by Acuña and Orchard (2017) as a method to better mitigate the risk of the mission.

Chapter 4

Case Study: Delivery Missions

4.1 Introduction

In this Chapter, the proposed prognostic framework is applied to discharge cycles of a Li-Po battery of a small-size quadcopter that perform delivery missions. That is, flights mission where the quadcopter initially carries a payload that has to be delivered to a certain location. Once the payload is delivered, the quadcopter has to fly back to the starting point. With the aim of illustrating each of the contributions of this work, several scenarios are considered and evaluated. Section 4.2 describes the delivery missions used. In section 4.3, indicators for prognostics used in this analysis are introduced. Section 4.4 presents a performance analysis in terms of effectiveness and efficiency of the proposed battery model and the proposed OFCL. In section 4.5, prediction results without and with using the proposed power consumption model are presented and discussed. Section 4.6 evaluates the effects on prediction results of using the new Probability of Failure (PoF) definition concerning the conventional definition. Finally, Section 4.7 exposes a summary of the chapter.

4.2 Missions Description

The discharges cycle data used corresponds to delivery missions performed by a 3DR IRIS+ quadcopter (Fig. 3.6), whose parameters are summarized in Table 3.2 and that uses a 3S 5100mAh Li-Po battery. Two flight plans are utilized for the analysis developed in this Chapter. The plans are described in Table 4.1 and Table 4.2. Phase 8 in each flight consists in discharge of the battery at a similar power to that observed during phase 6 to safely obtain an approximate measurement for the amount of flight time that would have been supported by the battery if the multicopter had continued to be flown at the approximately same speed as it was going in phase 6. This measurement allows comparison between battery EOD predictions made at various points over the sample mission, and the EOD time observed experimentally. For a voltage threshold (V_{EOD}) equal to 10.3 volts, the observed EOD time is 1274 seconds for the flight plan No. 1 and 1173 seconds for the flight plan No. 2.

Table 4.1: Flight Plan No. 1.

No.	Maneuver	Payload (kg)	Translational speed (m/s)	Duration (s)
1	Take off & Climb (to 120 m)	0.3	1.5	80
2	Horizontal flight	0.3	6.0	210
3	Descent & land	0.3	0.5	240
4	Delivering payload	0.3	0.0	60
5	Take off & Climb (to 120 m)	0.0	1.5	80
6	Horizontal flight	0.0	6.0	210
7	Descent & land	0.0	0.5	240
8	Fully deplete battery	–	–	Until reaching the voltage threshold

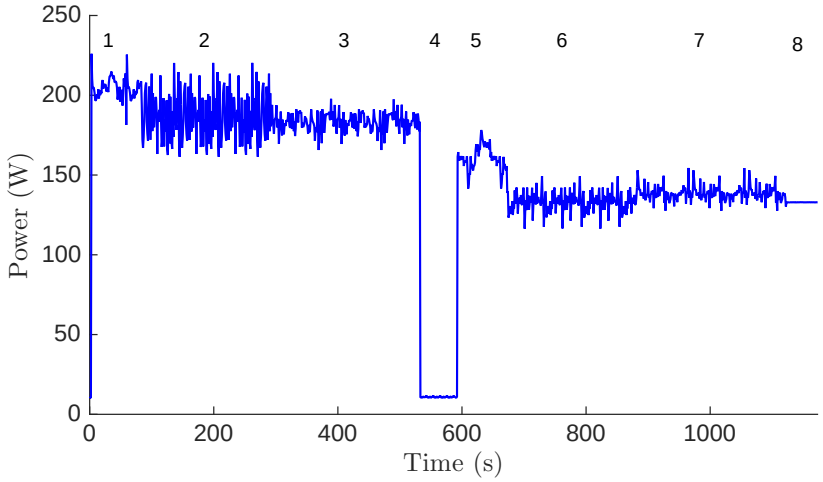

Figure 4.1: Power profile for flight plan No 1.

Table 4.2: Flight Plan No. 2.

No.	Maneuver	Payload (kg)	Translational speed (m/s)	Duration (s)
1	Take off & Climb (to 120 m)	0.3	2.5	48
2	Horizontal flight	0.3	12.0	360
3	Descent & land	0.3	1.5	80
4	Delivering payload	–	0.0	60
5	Take off & Climb (to 120 m)	0.0	2.5	48
6	Horizontal flight	0.0	12.0	360
7	Descent & land	0.0	1.5	80
8	Fully deplete battery	–	–	Until reaching the voltage threshold

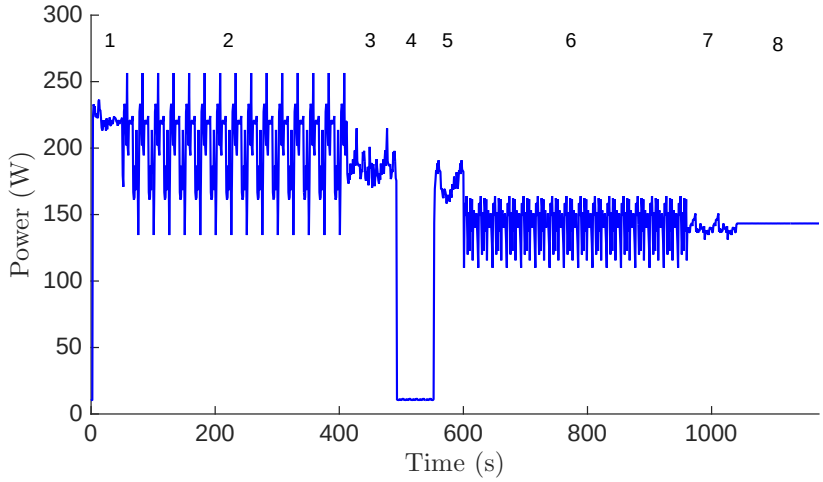

Figure 4.2: Power profile for flight plan No 2.

A quadcopter can achieve six Degrees of Freedom (DOF) by planning maneuvers that make use of its four controllable degrees of freedom: thrust, pitch, yaw, and roll. Namely, a quadcopter has the ability to fly in any direction. Nevertheless, it may have mobility constraints that arise naturally due to physical limits of the actuators. For example, the quadcopter might have difficulties in tracking a curve when it flies at high speeds. To avoid this kind of constraints, the path followed by the quadcopter did not include any curvature. That is, once the quadcopter climbs vertically up to reach the desired altitude, the path followed by the multirotor consisted of a straight line between the take-off point and the point where the payload is delivered. In this latter point, the quadcopter descents vertically and lands. Note that during vertical climb and vertical descent only the thrust needs to be controlled, and during the horizontal flight in a straight line, besides the thrust, only the pitch needs to be controlled.

4.3 Performance Indicators

Performance indicators for prognostics used in this analysis incorporate information from EOD expectations, which correspond to the instant k when the expectation of the battery voltage reaches the threshold, the Just-In-Time Point value which incorporates the concept of risk, specifying the cycle of operation where the probability of failure reaches a specified threshold γ ($JITP_{\gamma\%}$) (Engel et al., 2000), and the $\alpha - \lambda$ performance with the β criterion (Saxena et al., 2008, 2009):

$$\widehat{EOD} \triangleq E\{k|E\{V(k)\} = V_{EOD}\}, \tag{4.1}$$

$$JITP_{\gamma\%} = \arg\min_{\text{eod}}(Pr\{EOD \leq \text{eod}\} \geq \gamma\%), \tag{4.2}$$

Table 4.3: Scenarios to illustrate contributions 1 and 2

	Scenario 1	**Scenario 2**	**Scenario 3**
System model	Equivalent Circuit Model	Equivalent Circuit Model	Electrochemistry-based Model
Estimation algorithm	PF (100 Particles)	PF (100 Particles)+OFCL	PF (100 Particles)
Prediction algorithm	PF-based (100 Samples)	PF-based (100 Samples)	PF-based (100 Samples)
Future inputs	Actual inputs	Actual inputs	Actual inputs

$$\pi[r(k)]|_{\alpha^-}^{\alpha^+} = \sum_{\alpha^-}^{\alpha^+} \phi(x), \tag{4.3}$$

where $r(k)$ is the probability distribution of the predicted RUL at time index k, ϕ is the non-parameterized probability distribution, and π is the total probability mass within $[\alpha^-, \alpha^+]$, being $\alpha^- = RUL^*(1-\alpha)$, $\alpha^+ = RUL^*(1+\alpha)$ and RUL^* the ground truth RUL. RUL distribution satisfies β criterion when $\pi[r(k)]|_{\alpha^-}^{\alpha^+} \geq \beta$.

4.4 Simplified Battery Model Along with the Novel OFCL During Estimation Stage

To evaluate the performance of the proposed solution, SOC estimation and EOD predictions are performed under the scenarios described in Table 4.3.

It has been postulated that the novel Feedback Correction Loop (OFCL) during the estimation stage can adjust the variance of the process noise to diminish the bias in Bayesian state estimation. Thus, unlike scenario 1, scenario 2 incorporate the proposed OFCL during the estimation stage to evaluate its effectiveness by comparing with predictions results obtained under the scenario 1, namely, when the OFCL is not used during the estimation stage.

Also, it is postulated that the simplified equivalent circuit battery model proposed allows reducing computational resources and providing accurate prediction results when used along with the OFCL during the estimation stage. Therefore, in order to evaluate the accuracy and efficiency of the proposed solution, scenario 3 uses a high fidelity battery model. The model used is an Electrochemistry-based model (Daigle and Kulkarni, 2013) of lithium-ion batteries that captures the significant electrochemical processes.

The parameters of the equivalent circuit battery model used are summarized in Table 3.1 and the OFCL parameters are summarized in Table 4.4.

For flight plan No. 1, SOC estimation and EOD prediction results without OFCL (scenario 1) and with OFCL (scenario 2) are shown in Fig. 4.3 and Fig. 4.4 correspondingly, and results with the Electrochemistry-based Model (scenario 3) are shown in Fig. 4.5. The average results of 50 realizations in terms of the metrics described in section 4.3 are summarized in Table 4.5.

Table 4.4: OFCL parameters

Parameter	**Value**
n	3
e_{thr}	0.0329
$\mathbf{p}$	$\begin{bmatrix}0.995 & 0.99 & 0.995\end{bmatrix}$
$\mathbf{q}$	$\begin{bmatrix}1.025 & 1.01 & 1.025\end{bmatrix}$

For flight plan No. 2, SOC estimation and EOD prediction results without OFCL (scenario 1) and with OFCL (scenario 2) are shown in Fig. 4.6 and Fig. 4.7 correspondingly, and results with the Electrochemistry-based Model (scenario 3) are shown in Fig. 4.8. The average results of 50 realizations in terms of the metrics described in section 4.3 are summarized in Table 4.6.

EOD estimates presented in Table 4.5 and Table 4.6, show that the EOD expectation is, indeed, a random variable. Furthermore, it may happen that some realizations of this random variable underestimate (or overestimate) the ground truth EOD. Nevertheless, the obtained estimates when the equivalent circuit model is used, are sufficiently accurate. More importantly, they tend to underestimate the EOD, thus minimizing the probability of unexpected failure (conservative approach).

For flight plan No. 1, the maximum error in the expected EOD time value is 28 seconds for the first case without OFCL, and 19 seconds for the second case with OFCL, when the prediction horizon was 315 seconds. Considering the length of the long-term prediction windows, the maximum error between the ground truth and the expected EOD correspond to only 8.88% and 6.3% respectively. Regarding Just-In-Time Point estimates, the values obtained for the $JITP_{5\%}$ when the equivalent circuit model is used are always smaller than the ground truth EOD, thus ensuring a safe utilisation of the asset. In terms of the $\alpha - \lambda$ performance, the average of the probability mass, π, is 86.6% for the first case, while in the second case it is 100%.

For flight plan No. 2, the maximum error in the expected EOD time value is 28 seconds for the first case without OFCL when the prediction horizon was 264 seconds and 21 for the second case with OFCL when the prediction horizon was 610 seconds. Considering the length of the long-term prediction windows, the maximum error between the ground truth and the expected EOD correspond to only 10.61% and 3.44% respectively. Regarding Just-In-Time Point estimates, the values obtained for the $JITP_{5\%}$ when the equivalent circuit model is used tend to be smaller than the ground truth EOD, thus ensuring a safe utilization of the asset. In terms of the $\alpha - \lambda$ performance, the average of the probability mass, π, is 82.4% for the first case, while in the second case it is 100%.

In general, reasonable results were obtained in the first scenario without OFCL and improved results in the second case with the proposed OFCL that implements a digital filter on observation error instead of using the accumulated error. This result supports the idea that an OFCL helps to diminish the bias in Bayesian state estimation, which results in more accurate prediction results since the states/parameters estimated correspond to the initial

Table 4.5: Average prediction results of 50 realizations for flight plan No. 1. True EOD at 1274 s

	Equivalent Circuit Model, PF estimator and PF-based predictor			Equivalent Circuit Model, PF+OFCL estimator and PF-based predictor			Electrochemistry-based Model, PF estimator and PF-based predictor		
SOC	$\widehat{EOD}$	$JITP_{5\%}$	$\pi[r(k)]\|_{\alpha^-}^{\alpha^+}$	$\widehat{EOD}$	$JITP_{5\%}$	$\pi[r(k)]\|_{\alpha^-}^{\alpha^+}$	$\widehat{EOD}$	$JITP_{5\%}$	$\pi[r(k)]\|_{\alpha^-}^{\alpha^+}$
75% ($t = 267$ s)	1271.301 s	1242.380 s	100.00%	1276.178 s	1248.960 s	100.00%	1302.814 s	1238.160 s	99.78%
50% ($t = 598$ s)	1262.072 s	1247.560 s	100.00%	1270.857 s	1255.960 s	100.00%	1306.470 s	1254.740 s	94.80%
25% ($t = 959$ s)	1245.874 s	1229.580 s	60.00%	1263.704 s	1256.800 s	100.00%	1316.338 s	1281.600 s	22.84%

Table 4.6: Average prediction results of 50 realizations for flight plan No. 2. True EOD at 1173 s

	Equivalent Circuit Model, PF estimator and PF-based predictor			Equivalent Circuit Model, PF+OFCL estimator and PF-based predictor			Electrochemistry-based Model, PF estimator and PF-based predictor		
SOC	$\widehat{EOD}$	$JITP_{5\%}$	$\pi[r(k)]\|_{\alpha^-}^{\alpha^+}$	$\widehat{EOD}$	$JITP_{5\%}$	$\pi[r(k)]\|_{\alpha^-}^{\alpha^+}$	$\widehat{EOD}$	$JITP_{5\%}$	$\pi[r(k)]\|_{\alpha^-}^{\alpha^+}$
75% ($t = 248$ s)	1189.704 s	1165.240 s	100.00%	1193.016 s	1168.100 s	100.00%	1204.408 s	1145.820 s	99.60%
50% ($t = 563$ s)	1175.030 s	1162.000 s	100.00%	1194.085 s	1171.200 s	100.00%	1208.719 s	1162.940 s	89.06%
25% ($t = 909$ s)	1145.095 s	1131.460 s	47.22%	1179.845 s	1172.980 s	100.00%	1217.866 s	1187.100 s	12.72%

states/parameters of the prediction stage.

Results with the electrochemistry-based model tend to overestimate the EOD as reported by (Daigle and Kulkarni, 2013) for variable loading discharges. In this case, for flight plan No. 1, the maximum error in expected EOD time value is 42 seconds, that occurs when the prediction horizon is 315 seconds. For flight plan No. 2, the maximum error in expected EOD time value is 44 seconds when the prediction horizon is 264 seconds. Considering the length of the long-term prediction window, the maximum error between the ground truth and the expected EOD correspond to 13.3% and 16.67% respectively. Regarding Just-In-Time Point estimates, the values obtained for the $JITP_{5\%}$ are not always smaller than the ground truth EOD, which does not provide a safe utilization of the asset because the actual EOD time might be before the end of the mission. In terms of the $\alpha - \lambda$ performance, the average of the probability mass, π, is 72.47% for flight plan No. 1 and 67.12% for flight plan No. 2.

Although the electrochemistry-based model provides a more detailed characterization of the underlying battery phenomena, its use results in reasonable but less accurate results compared to the results obtained using the equivalent circuit model. This is attributed to the difficulty associated with proper estimation of model parameters that meet the constraints of the model. In particular, the electrochemical-based model requires 27 parameters that have to be estimated through several stages using different discharges. In contrast, the equivalent circuit model requires only 7 parameters which are estimated through a single stage using a single discharge.

Table 4.7: Average estimation processing time per iteration.

Algorithm	**Equivalent Circuit Model**	**Electrochemistry-based Model**
UKF	$1.309\text{e}-3$ s	$1.993\text{e}-3$ s
PF ($N = 100$)	$6.508\text{e}-4$ s	$2.450\text{e}-3$ s

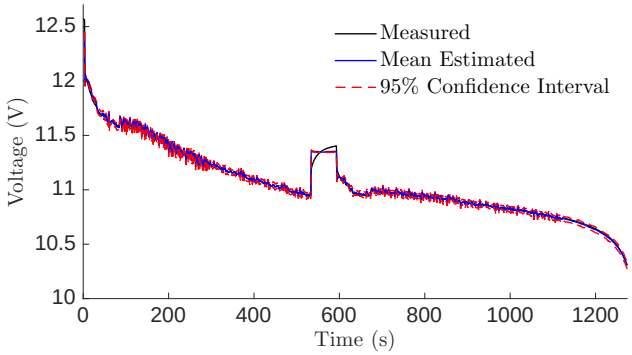

(a) Estimated Voltage

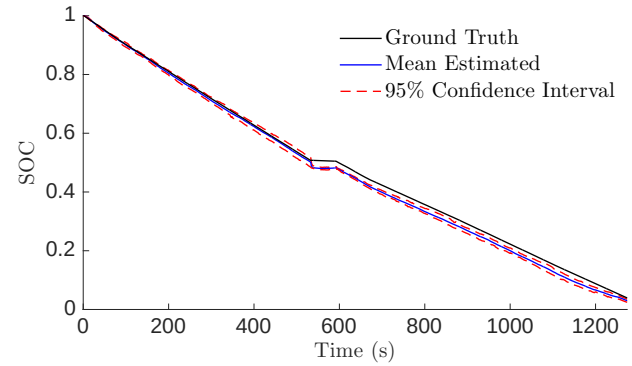

(b) Estimated SOC

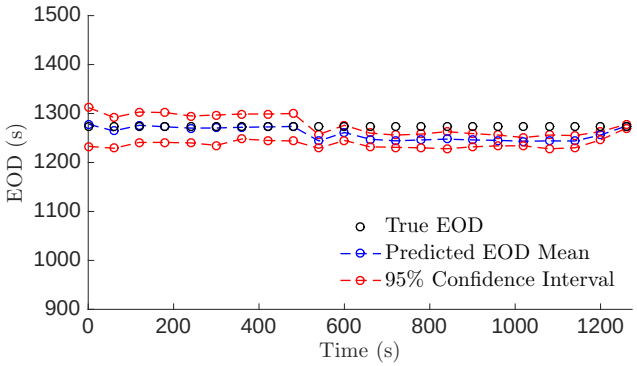

(c) Predicted EOD

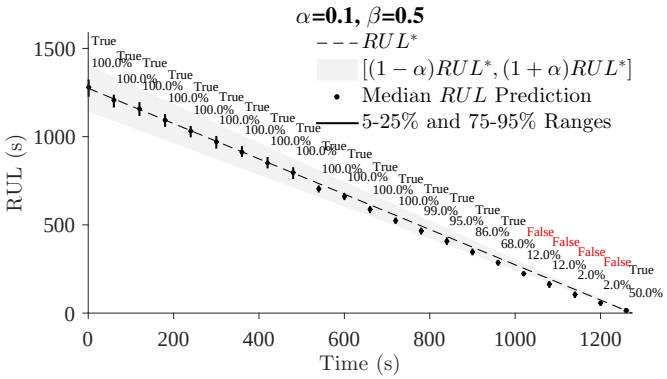

(d) $\alpha - \lambda$ performance

Figure 4.3: Equivalent Circuit Model, SOC estimation with PF and EOD prediction for flight plan No. 1.

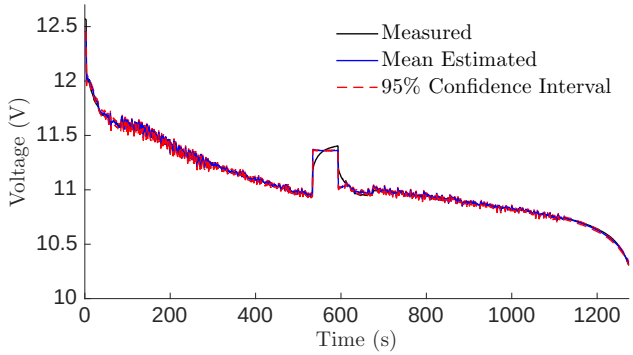

(a) Estimated Voltage

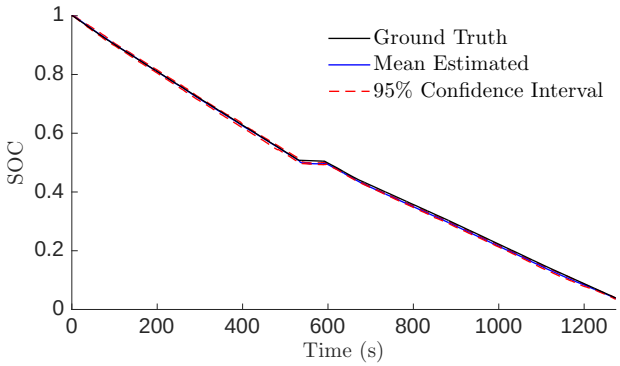

(b) Estimated SOC

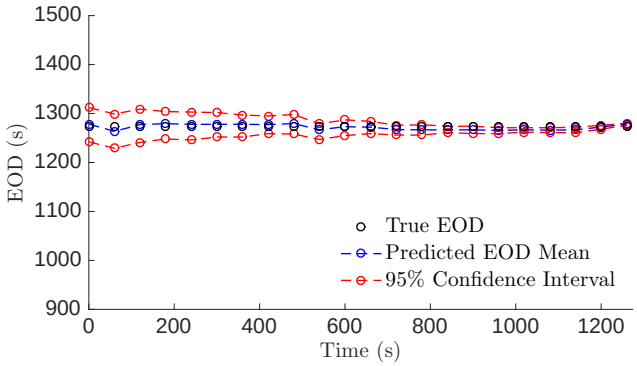

(c) Predicted EOD

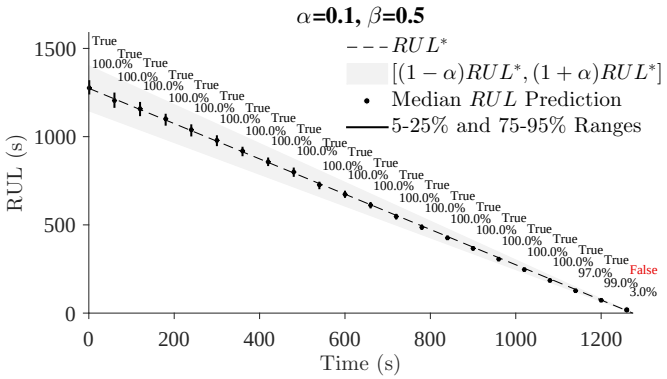

(d) $\alpha - \lambda$ performance

Figure 4.4: Equivalent Circuit Model, SOC estimation with PF+OFCL and EOD prediction for flight plan No. 1.

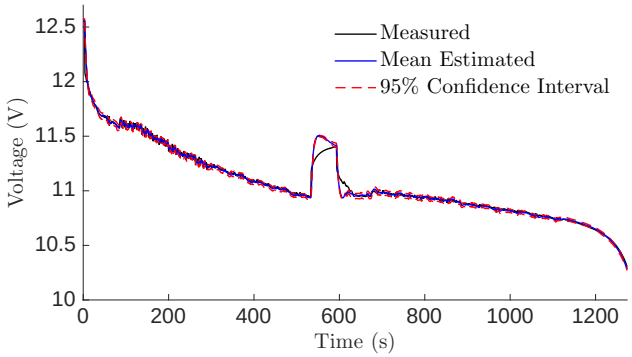

(a) Estimated Voltage

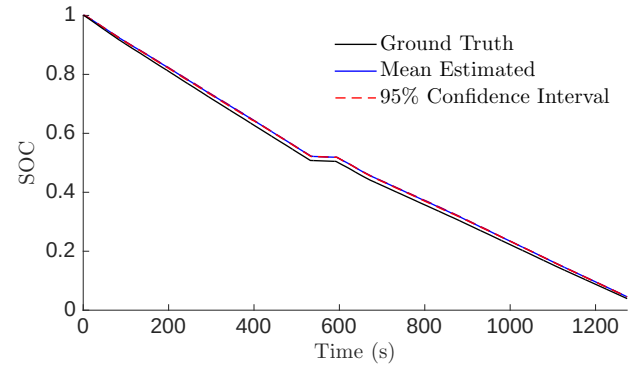

(b) Estimated SOC

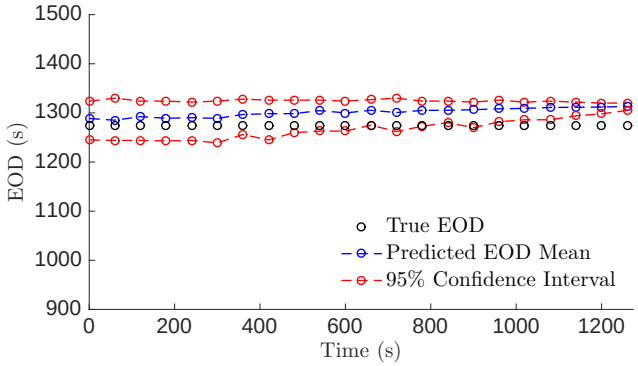

(c) Predicted EOD

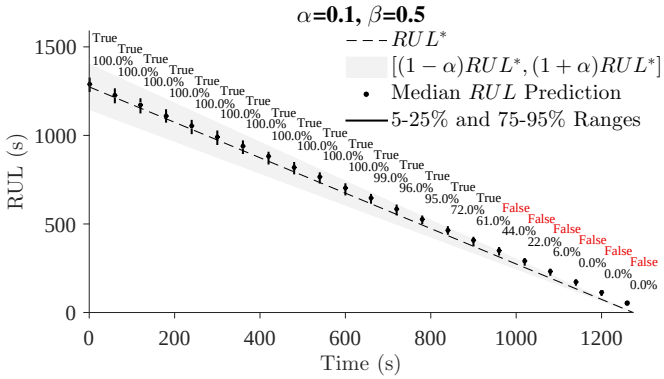

(d) $\alpha - \lambda$ performance

Figure 4.5: Electrochemistry-based model, SOC estimation with PF and EOD prediction for flight plan No. 1.

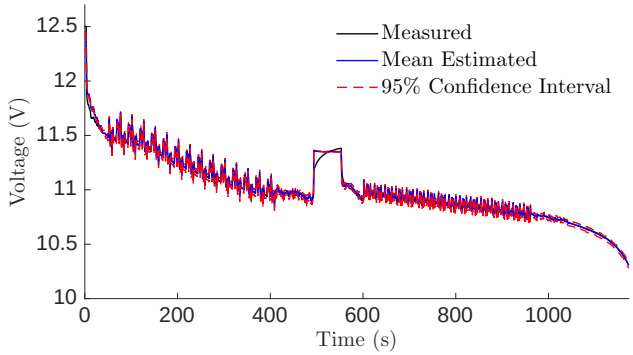

(a) Estimated Voltage

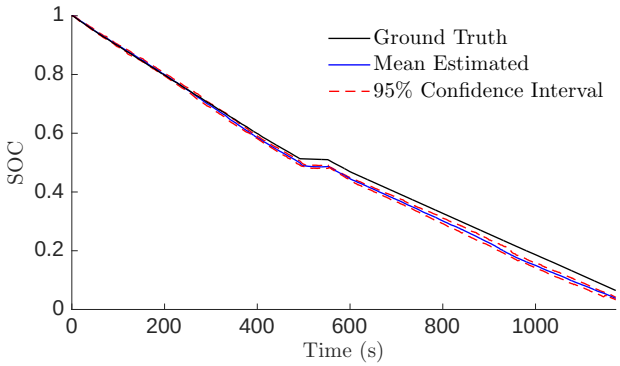

(b) Estimated SOC

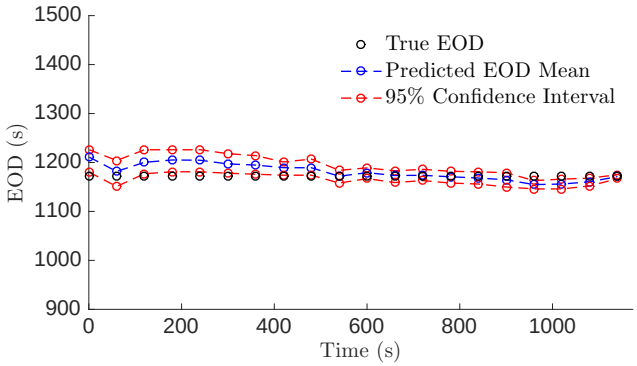

(c) Predicted EOD

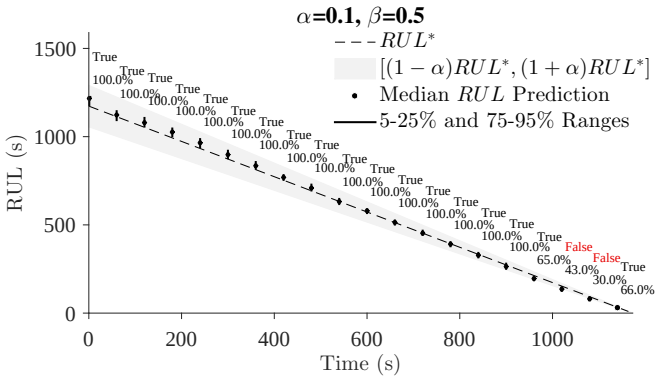

(d) $\alpha - \lambda$ performance

Figure 4.6: Equivalent Circuit Model, SOC estimation with PF and EOD prediction for flight plan No. 2.

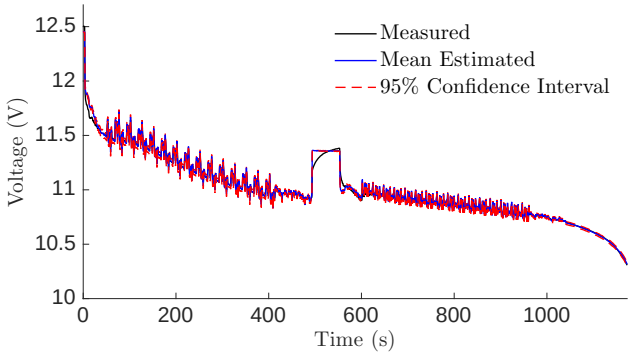

(a) Estimated Voltage

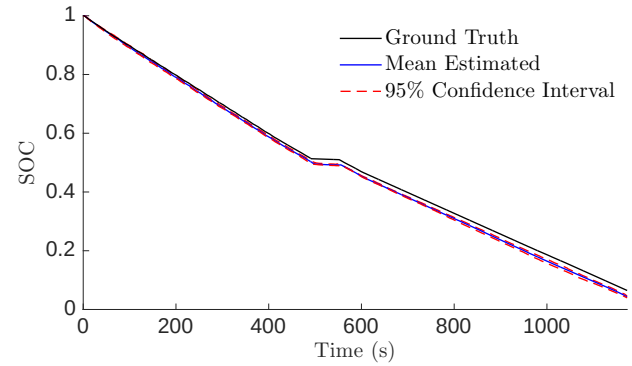

(b) Estimated SOC

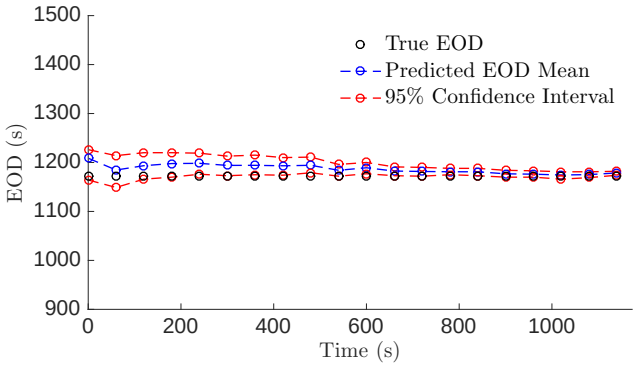

(c) Predicted EOD

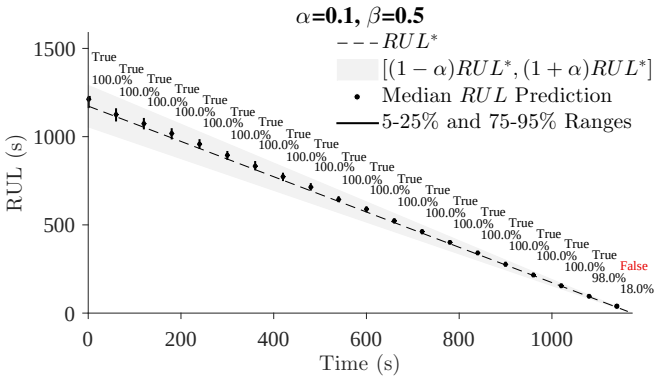

(d) $\alpha - \lambda$ performance

Figure 4.7: Equivalent Circuit Model, SOC estimation with PF+OFCL and EOD prediction for flight plan No. 2.

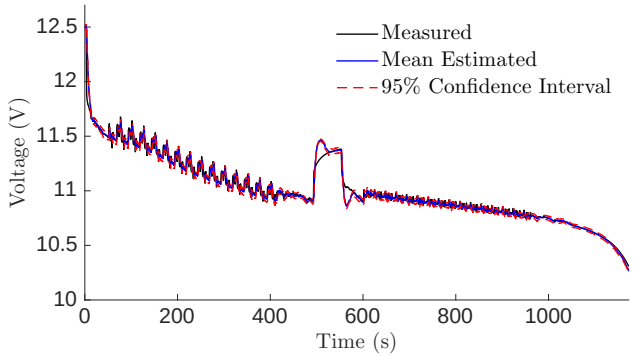

(a) Estimated Voltage

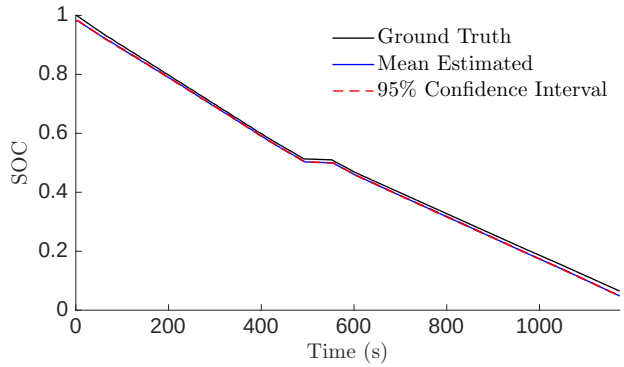

(b) Estimated SOC

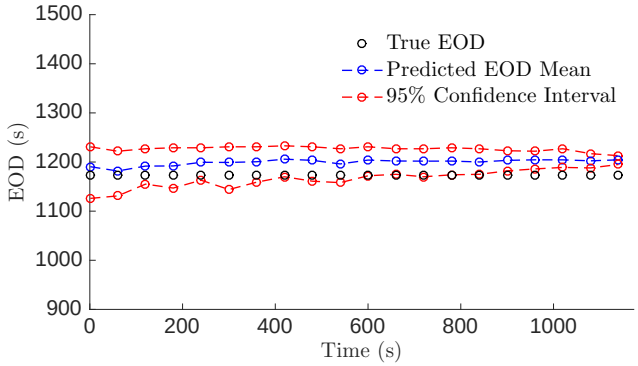

(c) Predicted EOD

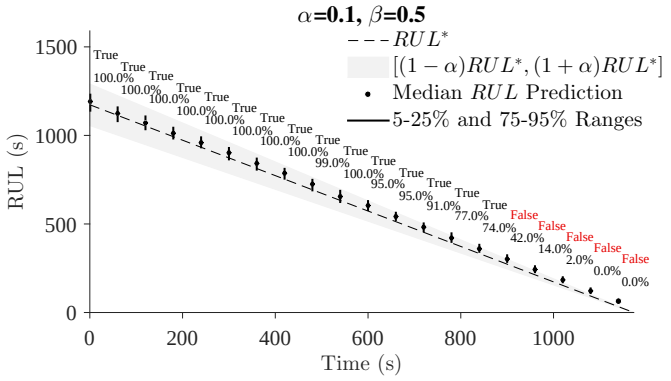

(d) $\alpha - \lambda$ performance

Figure 4.8: Electrochemistry-based model, SOC estimation with PF and EOD prediction for flight plan No. 2.

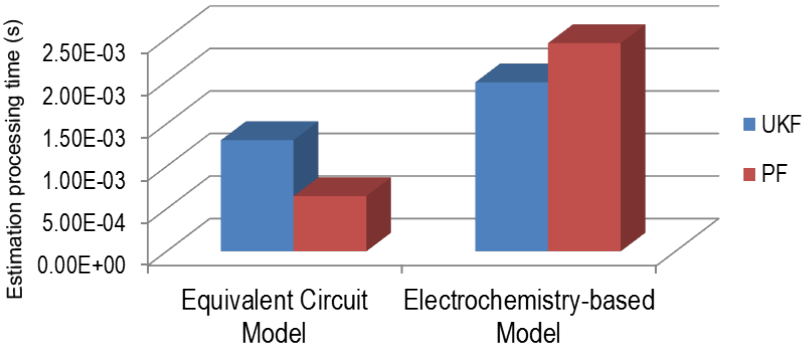

Figure 4.9: Average estimation processing time per iteration.

Table 4.8: Average prediction processing time for a time windows of 1274 seconds.

Samples	**Equivalent Circuit Model**	**Electrochemistry-based Model**
10	0.464 s	0.811 s
50	0.483 s	1.570 s
100	0.496 s	2.510 s
500	0.637 s	10.155 s
1000	0.821 s	18.656 s
5000	1.994 s	42.208 s
10000	3.279 s	67.313 s
50000	16.584 s	306.517 s
100000	32.558 s	609.249 s

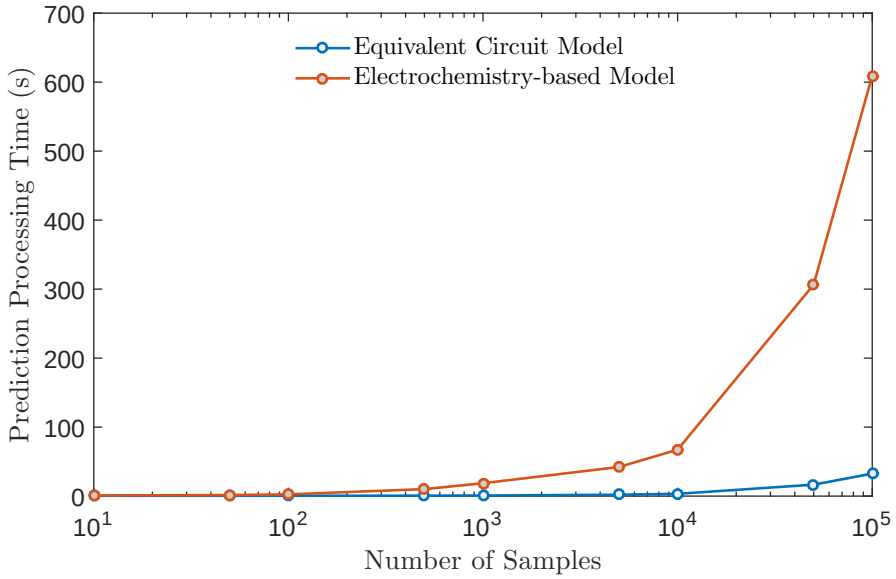

Figure 4.10: Average prediction processing time for a time windows of 1274 second.

Besides, the average estimation processing time per iteration was measured for both models using Unscented Kalman Filter (UKF) and Particle Filter (PF) as estimation algorithms. See Table 4.7 and Fig. 4.9. Similarly, the prediction processing time for a time window of 1274 seconds using both models was measured for a different number of samples. The length of the prediction window used to measure the processing time was set at a similar value to the length of the prediction window when a prediction is made at the beginning of the mission. Thus, the measured processing time approximately corresponds to the longest prediction processing time that may result during the mission.

The results are summarized in Table 4.8 and Fig. 4.10. For implementation, models and algorithms of the Prognostics Model Library (Daigle, 2016b) and the Prognostics Algorithm Library (Daigle, 2016a) by NASA Ames Research Center were used for the development of this study. MATLAB R2015b running on a Intel Core i7-2860QM CPU @ 2.50Ghz with 8GB of RAM was used to measure the processing times, making sure no other application was running at the same time.

The estimation processing time per iteration (see Table 4.7) using the equivalent circuit model is 65% of the time per iteration using the electrochemistry-based model when UKF is used as estimation algorithm, and it is 26.5% of the time per iteration using the electrochemistry-based model when PF with 100 particles is used as estimation algorithm. Considering that PF is shown to be more accurate than UKF (Walker et al., 2015), the possibility of using PF without increasing the processing times constitutes an advantage when one deals with constrained processing power, which may be encountered on small UAVs.

The prediction processing times are also shown significantly lower when the equivalent circuit model is used, in particular when the number of samples increases. As can be seen in Table 4.8 and Fig. 4.10, the prediction processing times with 10^2 and 10^5 samples using the equivalent circuit model is 19.76% and 5.34%, respectively, of the prediction processing time using the electrochemistry-based model. This could be attributed to the number of states of the model. The equivalent circuit model has 3 states in contrast to the electrochemistry-based model that has 7 states. Also, the electrochemistry-based model contains complex mathematical operations, such as logarithmic and inverse hyperbolic functions, that require higher computational resources.

4.5 Power Consumption Model as Future Inputs in Prediction Stage

In the above section, the actual power profile is used as future input during the prediction stage to insulate the sources of uncertainty from the uncertainty associated with the future inputs. However, to make evident the effects on prediction results of using the proposed power consumption model to define the future inputs, SOC estimation and EOD predictions are also performed under the scenarios described in Table 4.9. Scenario 4 uses only the hover equation to generate the future power consumption profiles, while scenario 5 uses the proposed power consumption model to generate the future power consumption profiles.

Table 4.9: Scenarios to illustrate contribution 3.

	Scenario 4	**Scenario 5**
System model	Equivalent Circuit Model	Equivalent Circuit Model
Estimation algorithm	PF (100 Particles)+OFCL	PF (100 Particles)+OFCL
Prediction algorithm	PF-based (100 Samples)	PF-based (100 Samples)
Future inputs	Hover equation ±20%	Power consumption model ±20%

(Gatti et al., 2015) proposes an analytical framework for addressing the flight time estimation of rotary-wing aircraft by imposing the balance between required and available power where hover equation, Eq. 3.13, is used to describe the power required. That assumes that the aircraft is in hovering flight condition during the entire flight, which is inaccurate and might cause a bias in the estimation of the flight time. By using the power consumption model proposed in the work described herein (Eq.3.13, Eq.3.14, Eq.3.15 and Eq.3.18) it is expected to get more accurate EOD predictions given a flight plan. Prediction results under scenario 5 in contrast with prediction results under scenario 4 allow illustrating this.

Prediction results are shown in Fig. 4.11, Fig. 4.12 and Table 4.10 for flight plan No. 1, and in Fig. 4.13, Fig. 4.14 and Table 4.11 for flight plan No. 2.

For flight plan No. 1, the maximum error in the expected EOD time value is 42 seconds for scenario 4 and 10 seconds for scenario 5. Regarding Just-In-Time Point estimates, the values obtained for the $JITP_{5\%}$ are always smaller than the ground truth EOD. In terms of the $\alpha - \lambda$ performance, the average of the probability mass, π, is 80.34% for scenario 4, while in the scenario 5 it is 98.06%.

For flight plan No. 2, the maximum error in the expected EOD time value is 37 seconds for scenario 4 and 21 seconds for scenario 5. Regarding Just-In-Time Point estimates, the values obtained for the $JITP_{5\%}$ are always smaller than the ground truth EOD. In terms of the $\alpha - \lambda$ performance, the average of the probability mass, π, is 91.33% for scenario 4, while in scenario 5 it is 95.93%.

In light of these results, when the aerodynamic-based model is used to define the future inputs, the prediction results are more accurate and stable. In addition, the bias in the expected EOD is lower and the confidence intervals are narrower, which causes the $\alpha - \lambda$ performance values improve relative to the prediction results obtained when only the hover equation is implemented. Depending on the flight plan, using only the hover equation to define the future inputs might cause underestimates of the EOD as seen for flight plan No. 1, or overestimates of the EOD as seen for flight plan No. 2.

It is worth mentioning that during the flight plan No. 2, the particular quadcopter used in this study tends to be more unstable because it carries its maximum payload at its maximum speed, which causes unexpected power peaks that are not considered in the definition of the future inputs. Because of this reason, improvements in results are more evident with the flight plan No.1. Nevertheless, results are shown improved in both flight plans when the power consumption model is used.

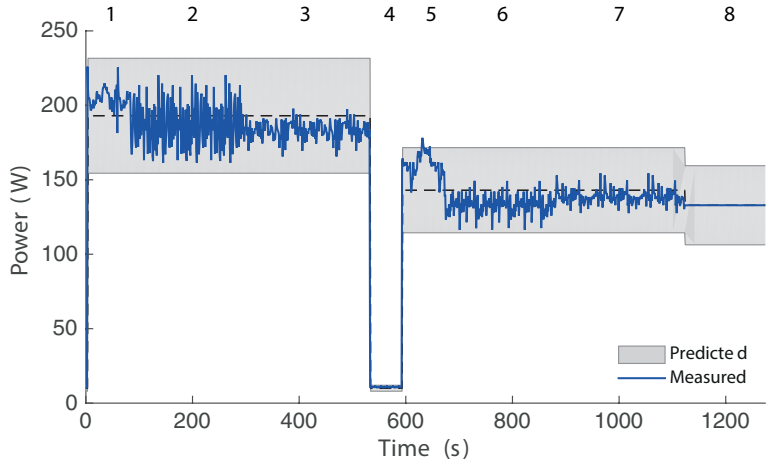

(a) Power profile for flight plan No. 1. Measured and predicted.

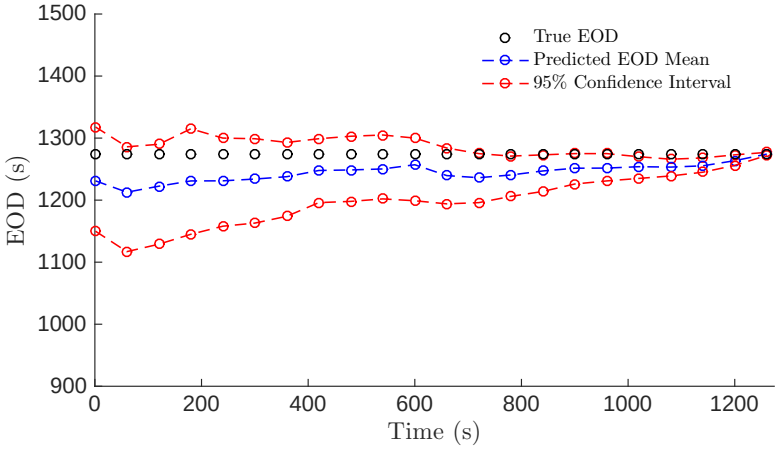

(b) Predicted EOD

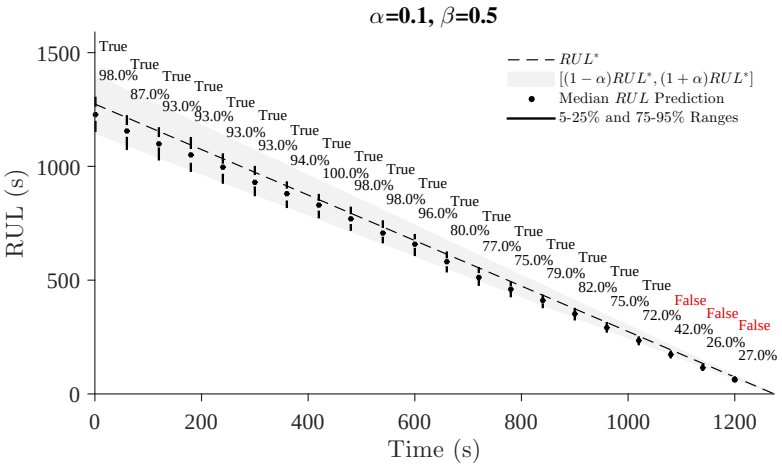

(c) $\alpha - \lambda$ performance

Figure 4.11: Equivalent circuit battery model, estimation with PF+OFCL and prediction with future inputs for flight plan No. 1 defined by the hover equation plus ±20%.

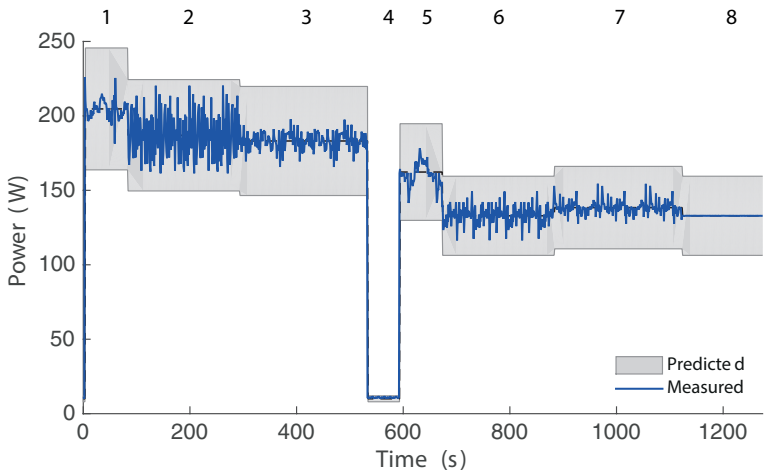

(a) Power profile for flight plan No. 1. Measured and predicted.

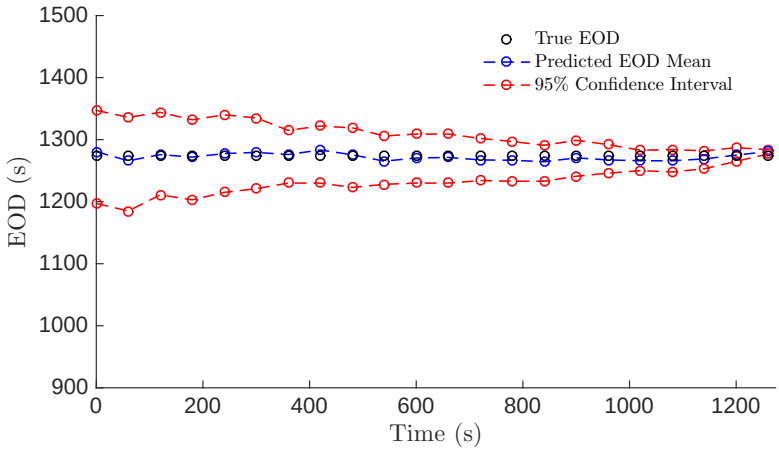

(b) Predicted EOD

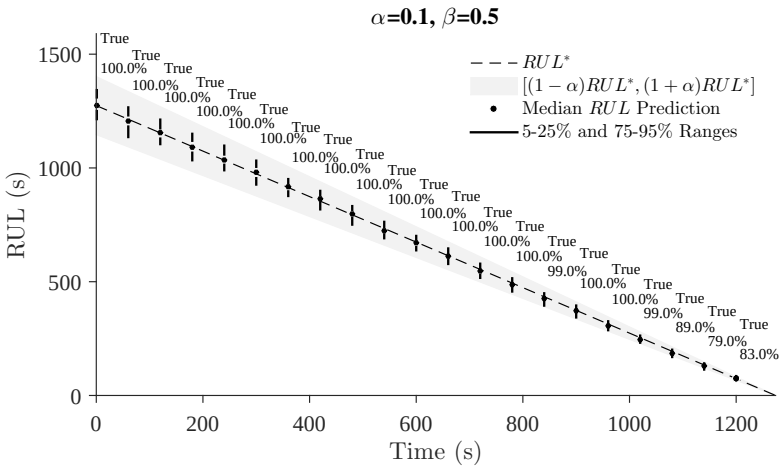

(c) $\alpha - \lambda$ performance

Figure 4.12: Equivalent circuit battery model, estimation with PF+OFCL and prediction with future inputs for flight plan No. 1 defined by the power consumption model plus ±20%.

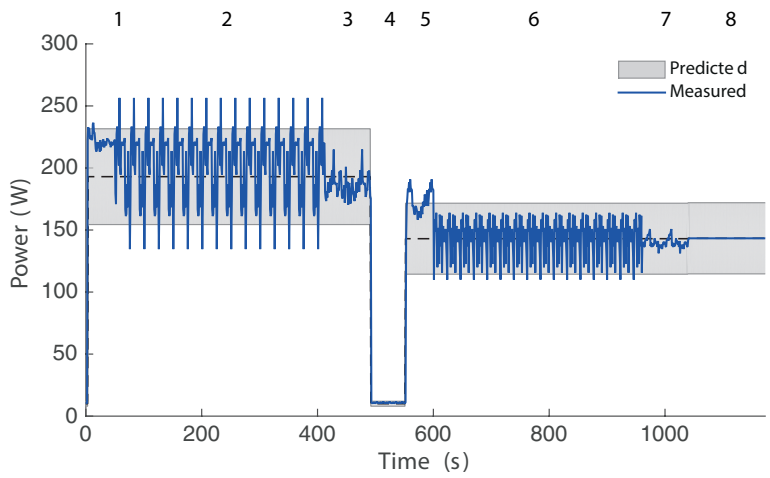

(a) Power profile for flight plan No. 2. Measured and predicted

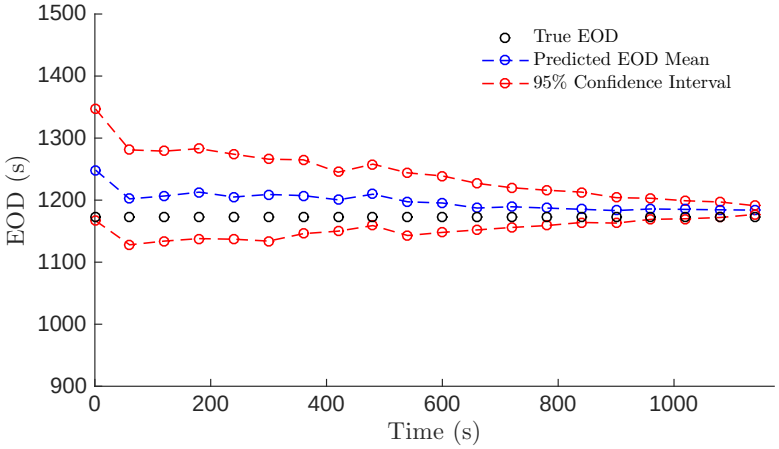

(b) Predicted EOD

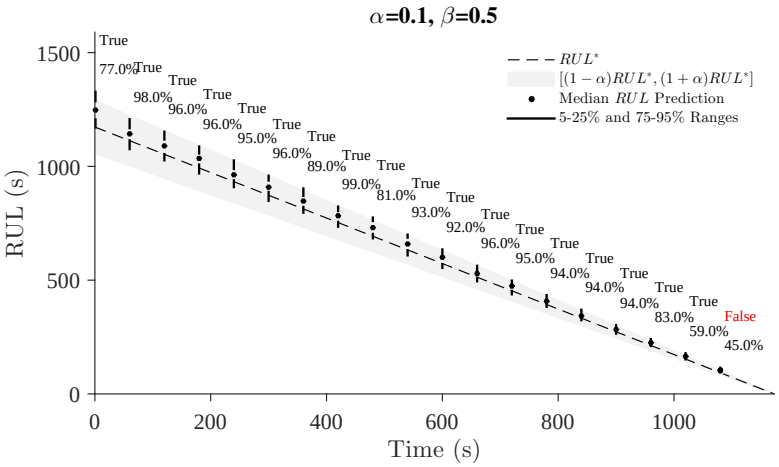

(c) $\alpha - \lambda$ performance

Figure 4.13: Equivalent circuit battery model, estimation with PF+OFCL and prediction with future inputs for flight plan No. 2 defined by the hover equation plus ±20%.

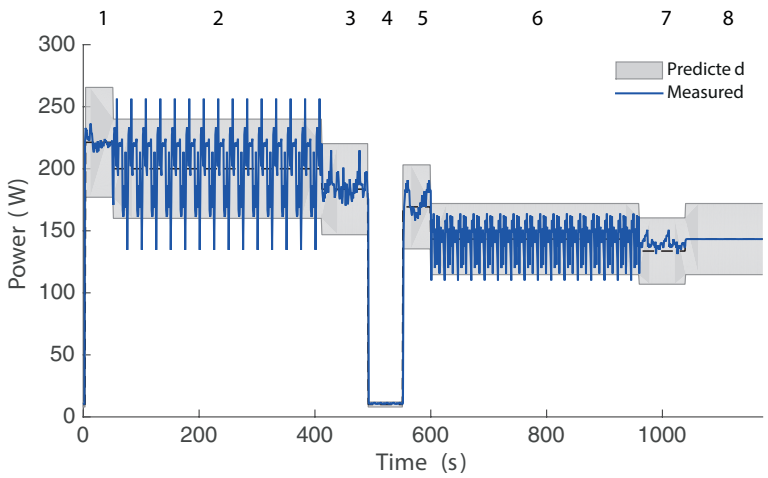

(a) Power profile for flight plan No. 2. Measured and predicted

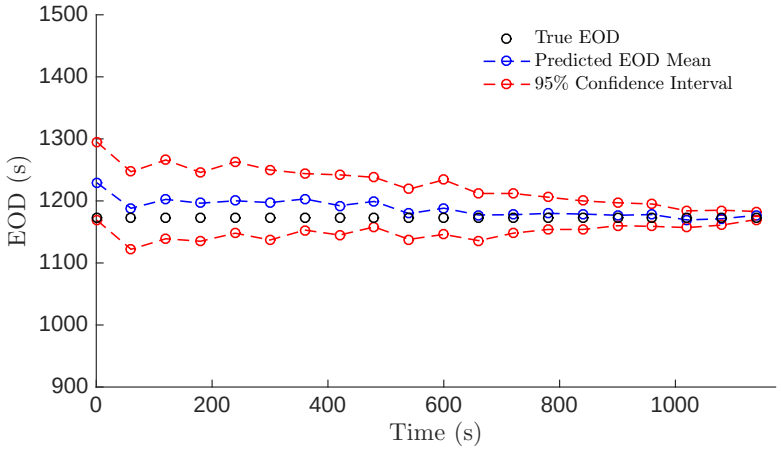

(b) Predicted EOD

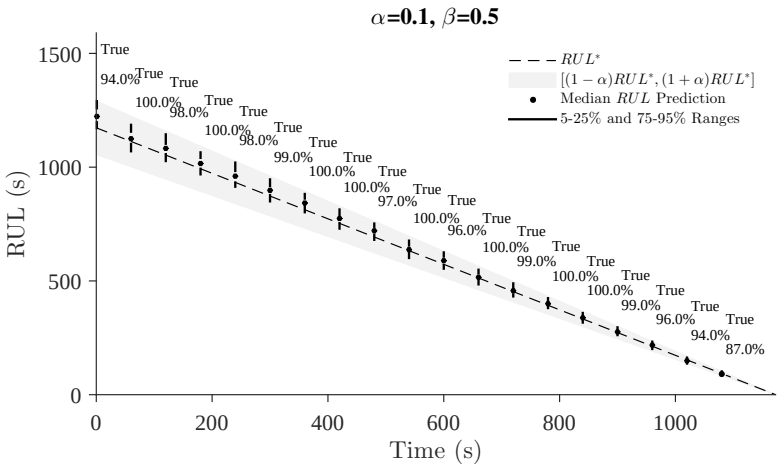

(c) $\alpha - \lambda$ performance

Figure 4.14: Equivalent circuit battery model, estimation with PF+OFCL and prediction with future inputs for flight plan No. 2 defined by the power consumption model plus ±20%.

Table 4.10: Average prediction results of 50 realizations for flight plan No. 1 with $P_h \pm 20\%$ and $P_{h,c,\mathrm{d},hor} \pm 20\%$ as future inputs. True EOD at 1274 s

	Equivalent Circuit Model, PF+OFCL estimator and PF-based predictor, $P_h \pm 20\%$ as future inputs			Equivalent Circuit Model, PF+OFCL estimator and PF-based predictor, $P_{h,c,\mathrm{d},hor} \pm 20\%$ as future inputs		
SOC	$\widehat{EOD}$	$JITP_{5\%}$	$\pi[r(k)]\|_{\alpha^-}^{\alpha^+}$	$\widehat{EOD}$	$JITP_{5\%}$	$\pi[r(k)]\|_{\alpha^-}^{\alpha^+}$
75% ($t = 267$ s)	1232.256 s	1160.940 s	93.82%	1276.300 s	1215.580 s	99.94%
50% ($t = 598$ s)	1245.166 s	1192.760 s	87.98%	1270.011 s	1229.280 s	99.90%
25% ($t = 959$ s)	1246.083 s	1224.600 s	59.22%	1264.698 s	1241.220 s	94.36%

Table 4.11: Average prediction results of 50 realizations for flight plan No. 2 with $P_h \pm 20\%$ and $P_{h,c,\mathrm{d},hor} \pm 20\%$ as future inputs. True EOD at 1173 s

	Equivalent Circuit Model, PF+OFCL estimator and PF-based predictor, $P_h \pm 20\%$ as future inputs			Equivalent Circuit Model, PF+OFCL estimator and PF-based predictor, $P_{h,c,\mathrm{d},hor} \pm 20\%$ as future inputs		
SOC	$\widehat{EOD}$	$JITP_{5\%}$	$\pi[r(k)]\|_{\alpha^-}^{\alpha^+}$	$\widehat{EOD}$	$JITP_{5\%}$	$\pi[r(k)]\|_{\alpha^-}^{\alpha^+}$
75% ($t = 248$ s)	1210.058 s	1142.520 s	94.30%	1194.522 s	1150.800 s	98.72%
50% ($t = 563$ s)	1200.132 s	1150.520 s	87.04%	1188.735 s	1145.420 s	97.38%
25% ($t = 909$ s)	1180.592 s	1159.660 s	92.66%	1175.705 s	1161.440 s	91.70%

4.6 Mitigating the Risk

Since EOD characterization is used as a base to make decisions about the flight plan and ensure that mission ends before battery energy is exhausted, this work proposes that the definition of Probability of Failure (PoF) by (Acuña and Orchard, 2017) applied to EOD time prognostics may mitigate the risk of suffering a catastrophe.

To illustrate and evaluate this, EOD PMF has been computed in the conventional way and using the new definition by (Acuña and Orchard, 2017) using $P_{h,c,\mathrm{d},hor} \pm 10\%$, $P_{h,c,\mathrm{d},hor} \pm 20\%$ and $P_{h,c,\mathrm{d},hor} \pm 30\%$ as future inputs, that is, for different levels of uncertainty in the future inputs. Results for flight plan No. 1 and flight plan No. 2 of a single realization at several times of prediction are shown in Fig. 4.15 and Fig. 4.16 correspondingly. In addition, Table 4.12 and Table 4.13 present the average mean EOD times of 50 realizations for flight plan No. 1 and flight plan No. 2 when predictions are performed at 75%, 50% and 25% of the SOC. Mean EOD time computed using the conventional definition is notated as $\widehat{EOD}$ and mean EOD time computed using the new definition is notated as $\widehat{EOD}'$.

As can be seen from Fig. 4.15, Fig. 4.16, Table 4.12 and Table 4.13, concerning the conventional way to compute the EOD PMF, the mean EOD experiment a shift to the left (i.e., to an earlier time). Hence, the use of the new definition of PoF provides more conservative characterizations of the EOD time, which mitigates the risk as the predicted EOD time is used in the making-decision process.

Table 4.12: Average prediction results of 50 realizations using the conventional PoF and new PoF for different future inputs and flight plan No. 1. True EOD at 1274 s

	Equivalent Circuit Model, PF+OFCL estimator and PF-based predictor $P_{h,c,\mathrm{d},hor} \pm 10\%$ as future inputs			Equivalent Circuit Model, PF+OFCL estimator and PF-based predictor $P_{h,c,\mathrm{d},hor} \pm 20\%$ as future inputs			Equivalent Circuit Model, PF+OFCL estimator and PF-based predictor $P_{h,c,\mathrm{d},hor} \pm 30\%$ as future inputs		
SOC	$\widehat{EOD}$	$\widehat{EOD}'$	$\widehat{EOD} - \widehat{EOD}'$	$\widehat{EOD}$	$\widehat{EOD}'$	$\widehat{EOD} - \widehat{EOD}'$	$\widehat{EOD}$	$\widehat{EOD}'$	$\widehat{EOD} - \widehat{EOD}'$
75% ($t = 267$ s)	1276.732 s	1245.007 s	31.724 s	1276.340 s	1227.243 s	49.096 s	1275.447 s	1200.111 s	75.336 s
50% ($t = 598$ s)	1270.847 s	1253.243 s	17.603 s	1271.068 s	1239.341 s	31.726 s	1268.833 s	1221.917 s	46.915 s
25% ($t = 959$ s)	1263.799 s	1256.155 s	7.643 s	1264.990 s	1249.628 s	15.362 s	1263.289 s	1239.686 s	23.603 s

Table 4.13: Average prediction results of 50 realizations using the conventional PoF and new PoF for different future inputs and flight plan No. 2. True EOD at 1173 s

	Equivalent Circuit Model, PF+OFCL estimator and PF-based predictor $P_{h,c,\mathrm{d},hor} \pm 10\%$ as future inputs			Equivalent Circuit Model, PF+OFCL estimator and PF-based predictor $P_{h,c,\mathrm{d},hor} \pm 20\%$ as future inputs			Equivalent Circuit Model, PF+OFCL estimator and PF-based predictor $P_{h,c,\mathrm{d},hor} \pm 30\%$ as future inputs		
SOC	$\widehat{EOD}$	$\widehat{EOD}'$	$\widehat{EOD} - \widehat{EOD}'$	$\widehat{EOD}$	$\widehat{EOD}'$	$\widehat{EOD} - \widehat{EOD}'$	$\widehat{EOD}$	$\widehat{EOD}'$	$\widehat{EOD} - \widehat{EOD}'$
75% ($t = 248$ s)	1203.636 s	1176.202 s	27.433 s	1204.522 s	1158.725 s	45.796	1200.765 s	1135.098 s	65.666
50% ($t = 563$ s)	1198.420 s	1181.692 s	16.727 s	1198.735 s	1167.376 s	31.359	1197.556 s	1148.930 s	48.625
25% ($t = 909$ s)	1184.930 s	1179.075 s	5.854 s	1185.705 s	1174.336 s	11.369	1185.324 s	1167.746 s	17.577

From Table 4.12, the minimum average shift to the left is 7.643 seconds which occurs when future inputs are defined to be $P_{h,c,\mathrm{d},hor} \pm 10\%$ and the SOC is 25%. The maximum average shift is 75.336 seconds which occurs when future inputs are defined to be $P_{h,c,\mathrm{d},hor} \pm 30\%$ and the SOC is 75%. Similarly, from Table 4.13, the average minimum shift is 5.854 seconds which occurs when future inputs are defined to be $P_{h,c,\mathrm{d},hor} \pm 10\%$ and the SOC is 25%, and the maximum average shift is 65.666 seconds which occurs when future inputs are defined to be $P_{h,c,\mathrm{d},hor} \pm 30\%$ and the SOC is 75%.

Overall, in contrast to the conventional way to compute the EOD PMF, the shift to the left of the mean EOD when the new definition of PoF is used, is larger when prediction horizon is longer and when uncertainty in the future inputs is greater. Namely, EOD characterization is more conservative when the risk is higher. Also, as can be seen in Fig. 4.15 and Fig. 4.16, the confidence intervals are narrower when the new definition of PoF is used.

This new PoF provides a way to mitigate the risk, which is more evident in the flight plan No. 2. During flight plan No. 2, the particular quadcopter used in this study tends to be more unstable because it carries its maximum payload at its maximum speed which causes unexpected power peaks that are not considered in the definition of the future inputs. As a result, predicted mean EOD time using the conventional definition of PoF are slightly overestimated, which could cause a catastrophe when this measure is used as a base in the decision-making process. However, using the new definition of PoF, mean EOD times tend to be before the true EOD time, mitigating so the risk of suffering a catastrophe. It should be mentioned that unexpected wind conditions might lead to similar situations where the EOD might be overestimated. The random behavior of the wind and the fact that the power consumption in multirotors is strongly determinate by wind speed and wind direction (Federal Aviation Administration, 2013), make the new definition of PoF a more suitable base to make decisions in applications with electric UAVs.

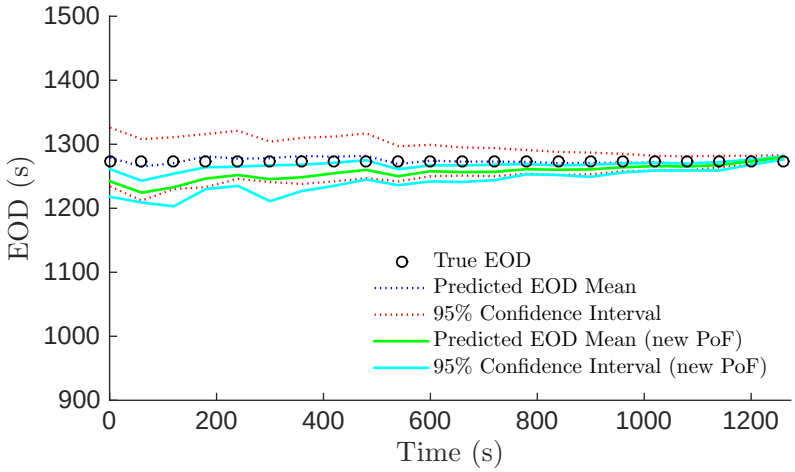

(a) EOD predicted with $P_{h,c,\mathrm{d},hor} \pm 10\%$ as future inputs

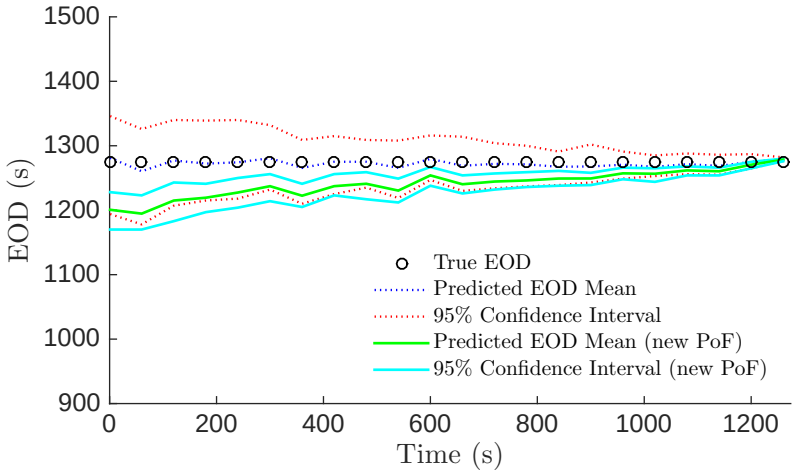

(b) EOD predicted with $P_{h,c,\mathrm{d},hor} \pm 20\%$ as future inputs

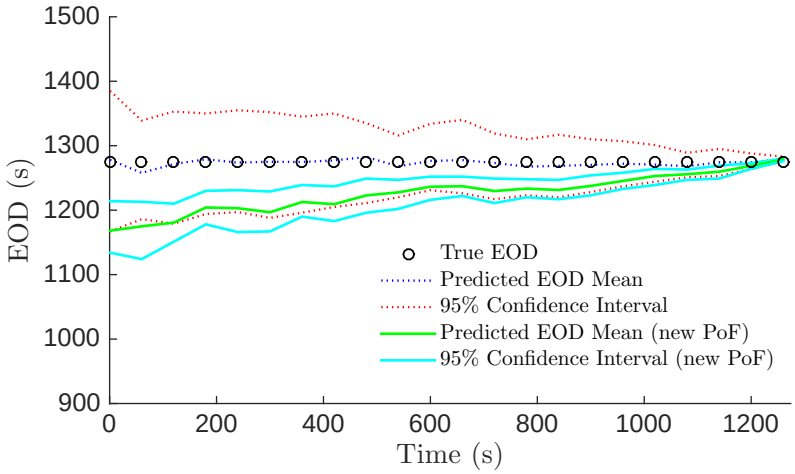

(c) EOD predicted with $P_{h,c,\mathrm{d},hor} \pm 30\%$ as future inputs

Figure 4.15: EOD PMF computed in the conventional way and using the new definition of PoF for different levels of uncertainty in the future inputs of flight plan No. 1.

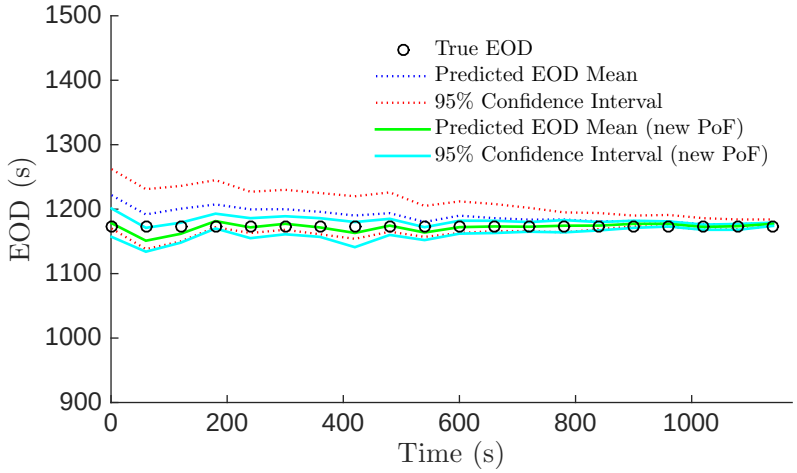

(a) EOD predicted with $P_{h,c,\mathrm{d},hor} \pm 10\%$ as future inputs

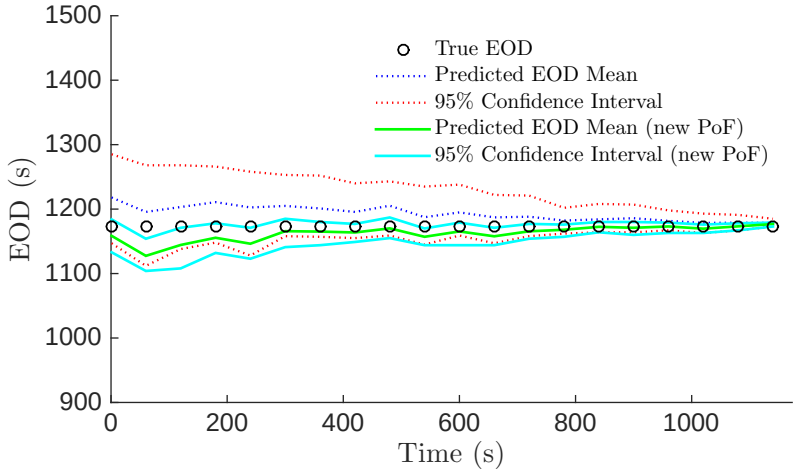

(b) EOD predicted with $P_{h,c,\mathrm{d},hor} \pm 20\%$ as future inputs

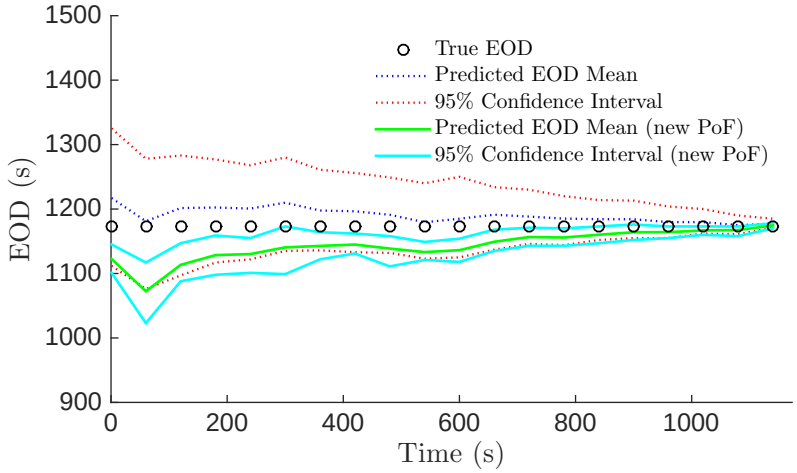

(c) EOD predicted with $P_{h,c,\mathrm{d},hor} \pm 30\%$ as future inputs

Figure 4.16: EOD PMF computed in the conventional way and using the new definition of PoF for different levels of uncertainty in the future inputs of flight plan No. 2.

4.7 Summary

In this Chapter, the proposed prognostic framework was used to estimate the SOC and predict the EOD time of a 3S 5100mAh Li-Po battery used by a 3DR IRIS+ quadcopter that performs delivery missions. To illustrate and evaluate the advantages of the proposed framework, each contribution of this thesis was introduced gradually into the framework, and prediction results were evaluated in terms of the EOD expectations, the Just-In-Time Point, and the $\alpha - \lambda$ performance. Also, estimation and prediction processing times were measured in order to evaluate the efficiency.

Initially, it is assumed that the future inputs are known, so the only uncertainty present in the prediction is that related to the model. Under this condition, SOC estimation and EOD predictions were performed (*i*) using the proposed simplified battery model without OFCL in the estimation stage, (*ii*) using the proposed simplified battery model with the novel OFCL in the estimation stage, and (*iii*) using an electrochemistry-based battery model.

Reasonable results were obtained in the first scenario without OFCL and improved results in the second case with the proposed OFCL (validating hypothesis 2). In addition, the use of the electrochemistry-based model results in reasonable but less accurate results compared to the results obtained using the equivalent circuit model, and estimation and prediction processing times were shown significantly lower when the equivalent circuit model is used. This latter validates hypothesis 1.

Secondly, in order to evaluate the proposed aerodynamic-based model to define future inputs profiles in the prediction stage, SOC estimation and EOD predictions were performed (*i*) using only the hover equation to generate future power consumption profiles, and (*ii*) using the proposed power consumption model to generate future power consumption profiles.

From the two above scenarios, prediction results are shown to be more accurate and stable when the aerodynamic-based model is used to define the future inputs, which validates hypothesis 3.

Finally, SOC estimation and EOD predictions were performed for different levels of uncertainty in the future inputs and the probability of failure was calculated using the definition by (Acuña and Orchard, 2017). The expected EOD using this new definition is compared with the expected EOD obtained using the conventional definition of probability of failure. Results show that concerning the conventional definition, there is a shift to the left of the mean EOD when the new definition is used, which is larger when prediction horizon is longer and when uncertainty in the future inputs is greater. Namely, EOD characterization using the definition by (Acuña and Orchard, 2017) is more conservative when the risk is higher (validating the hypothesis 4), which mitigates the risk of suffering a catastrophe as EOD time is used to make decisions about the flight plan.

Chapter 5

Concluding Remarks and Future Research

This thesis addresses a gap in BHM systems for rotatory-wing UAVs that have constraints associated with weight, size, and cost. Considering the aforementioned constraints that may be encountered on small UAVs, this work addressed the battery SOC estimation and EOD prediction problem with an efficient approach that allows reducing computational resources while providing very accurate EOD predictions. Also, this is the first research effort towards BHM for small-size rotary-wing UAVs validated beyond numerical simulations.

The thesis begins with a literature review about BHM for electric UAVs. From this literature review, BHM for rotary-wing UAVs arose as a little-explored research topic. With the exception of (de Souza Candido et al., 2014) which is aimed at rotary-wing aircraft (although it is limited to numerical simulations and hovering flight), reported works in the literature on BMH for UAVs are aimed at fixed-wing aircraft. In addition, these works focused their efforts on the accuracy of the EOD prediction while computational cost was not considered.

The literature review was completed by reviewing the literature relating SOC estimation and prognosis methods for batteries, and considerations on the performance of electric multirotors. As a consequence of such review, it was possible to conclude that a model-based prognostics architecture that utilizes Particle Filter during the estimation stage and a PF-based prognosis algorithm during the prediction stage, is suitable as a base for the development of this thesis; however, the architecture had to be adjusted considering the particular challenges of the problem.

Therefore, in order to reduce computational resources, an equivalent circuit battery model of reduced complexity has been proposed as the base of the prognostics architecture. The proposed model takes advantage of the concept of artificial evolution to incorporate the electric load dependence, the temperature dependence, and the SOC dependence into the model through on-line estimation of the absolute value of the battery internal impedance and the total energy that the battery is able to deliver. This model not only is simpler than previous models reported in the literature but also provides a better curve fit for batteries of

more than one cell.

Artificial evolution allows incorporating effects on the battery performance that are not directly included in the model. However, the process noise should be large enough to allow finding the right value of the parameters. Nevertheless, as process noise increases, the uncertainty on the state/parameter estimate increases as well, which affects the accuracy of the prediction results. Therefore, with the purpose of not losing accuracy in EOD predictions, a novel OFCL that utilizes a basic digital filter on the observation error was proposed to increase the process noise when the parameters need to be re-estimated (e.g., during a drastic change in the load current) and to decrease it when the parameters have reached the new correct value. The proposed OFCL solves the problems of previous OFCLs, and improves the effectiveness of the filtering process by diminishing the bias in Bayesian state estimation, which allows providing more accurate EOD time predictions.

Because the amount of useful remaining charge not only depends on the current SOC value but also on the future profile of discharge, it is known that a proper future load profile characterization leads to EOD predictions more accurate and more stable as well. Therefore, an approximate power consumption model to define the future inputs used during the prediction stage has been proposed and validated. The proposed consumption model characterizes the required power in each flight stage (i.e., climb, hovering flight, horizontal flight and descent), unlike previous works that address the flight time estimation of multirotors using only the characterization for hovering flight without considering other flight stages.

In addition, taking into consideration the catastrophic consequences that may occur as a result of an inaccurate EOD prediction, this work also proposes the use of the new definition of probability of failure by Acuña and Orchard (2017) to calculate the EOD PMF as a method to better mitigate the risk.

The proposed prognostic framework was used to estimate the SOC and predict the EOD time of a 3S 5100mAh Li-Po battery used by a 3DR IRIS+ quadcopter that performs delivery missions. Each contribution of this thesis was introduced gradually into the framework in order to illustrate and evaluate the advantages of each proposal. Prediction results were shown improved with the inclusion of each contribution. Overall, results show that the proposed framework is able to track the voltage well and provides very accurate EOD predictions while being computationally efficient. In addition, using the definition of probability of failure by Acuña and Orchard (2017), EOD time characterizations are shown to be more conservatives when the risk is higher, mitigating thus the risk of suffering catastrophic consequences. This validates the relevance of the proposed prognostic framework for Li-Po batteries in small-size multirotors.

5.1 Future work

According to the Federal Aviation Administration, the three broad factors that affect the performance of rotary-wing aircraft are density altitude (air density regarding altitude, pressure, and temperature), weight, and wind direction and velocity (Federal Aviation Administration,

2013). While air density and weight were considered in the power consumption model proposed in this thesis, the wind speed was assumed to be moderate, and its effects were not included directly in the model. Thus, the uncertainty on power consumption associated with the wind random behavior was characterized by a uniform distribution around the values given by the proposed consumption model.

However, under non-moderate wind condition, wind direction and velocity affect the power consumption significantly. Depending on the wind direction, it may affect positively or negatively. Headwinds are the most desirable as they contribute to the greatest increase in performance and decrease in required power. Therefore, to get accurate EOD predictions under higher wind conditions, future work should include more detailed characterization of the uncertainty associated with wind speed and wind direction over future inputs.

Considering the random nature of the wind, a stochastic characterization that incorporates prior and posterior information of the wind behavior could help to deal with this problem. Initial characterization of the uncertainty associated with wind behavior might be defined using historical data of daily wind cycle according to the season (which is usually available in wind maps). Once operation begins, the initial characterization could be updated as measurements are taken during the flight.

Appendix

Appendix A

Rotary-Wing Aerodynamics: Momentum Theory (Stepniewski, 1979)

Without going into any details regarding either geometric characteristics or the modus operandi of the thrust-generator itself, it is simply assumed that under static conditions as well as in translation at velocity $\vec{V}$ with respect to the ideal (frictionless and incompressible) fluid of density ρ and pressure p_o, the as-yet-undefined device is somehow capable of imparting linear momentum to the medium. For the sake of convenience, it is usually postulated that the thrust generator remains stationary while a very large mass of fluid moves past it at a uniform velocity $(-\vec{V})$, (Fig. A.1). It will also be assumed that the thrust coincides with the positive axis of a coordinate system having its origin at the "center" of the thrust generator.

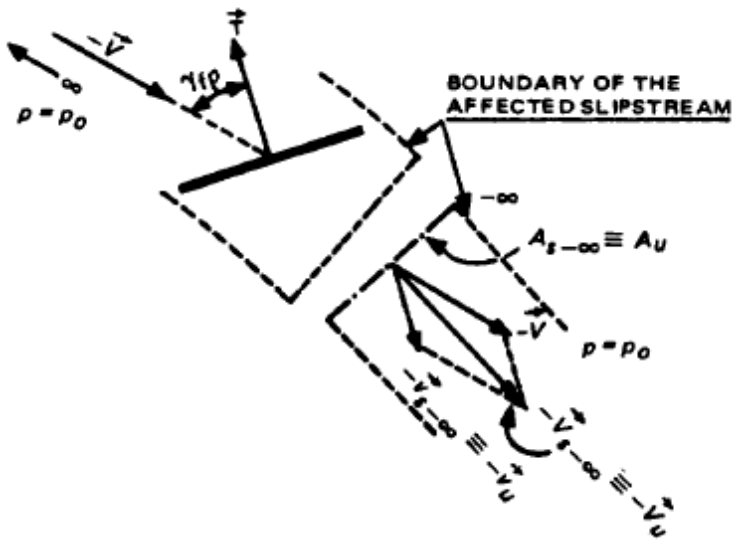

Figure A.1: Simplest physicomathematical model of a thrust generator (Stepniewski, 1979).

The thrust generator interacts with the fluid by imparting uniformly distributed linear momentum to a distinct streamtube bound by a surface through which the mass cannot be exchanged. This means that by the law of continuity, the mass flow within the tube is the same at every section, while both velocity and pressure of the fluid alter. However, at some point far downstream, the pressure returns p_o, and the incremental velocity variation reaches its ultimate value of $-\vec{v_u}$ uniformly distributed over the final tube cross-section area, A_u.

Knowledge of $-\vec{v_u}$ and A_u in addition to the already known $\vec{V}$ and ρ represents all the necessary information for determining the thrust $\vec{T}$ generated by this very simple physico-mathematical model, as well as for computing the power required in that process.

According to the laws of classical mechanics, the direction of the generated thrust($\vec{T}$) will be opposite to that of $\vec{v_u}$, while its magnitude will be equal to the rate of momentum change within the streamtube between its final and initial values. Denoting the rate of mass flow by $\dot{m}$, force $\vec{T}$ becomes

$$\vec{T} = -\dot{m} \cdot (\vec{V_u} - \vec{V}), \tag{A.1}$$

where the resultant velocity of flow far downstream ($\vec{V_u}$) is $\vec{V_u} = \vec{V} + \vec{v}_u$. Consequently, Eq. A.1 becomes

$$\vec{T} = -\dot{m}\vec{v}_u. \tag{A.2}$$

Furthermore, since $\dot{m} = V_u A_u \rho$, the above equation can be rewritten as

$$\vec{T} = -|\vec{V} + \vec{v}_u| A_u \rho \vec{v}_u, \tag{A.3}$$

where $||$ denotes the absolute (scalar) value of the resultant vector, $\vec{V_u}$; while $\vec{v}_u$ from now on will be known as the ***fully-developed induced velocity***.

It is also necessary to consider the power (P) required in the process. This can be done by examining the difference in the rate of flow of kinetic energy through a cross-section of the streamtube far downstream in the ultimate wake ($\dot{E}_u$) and far upstream ($\dot{E}_{up}$).

$$P = \dot{E}_u - \dot{E}_{up} = \tfrac{1}{2}\dot{m}(\vec{V}_u^2 - \vec{V}^2). \tag{A.4}$$

Remembering that $\vec{V_u} = \vec{V} + \vec{v}_u$, and performing subtraction as indicated in Eq. A.4, one obtains

$$P = \tfrac{1}{2}\dot{m} v_u (2V + v_u), \tag{A.5}$$

but $\dot{m}\vec{v}_u = -\vec{T}$; hence, Eq. A.5 can be rewritten as follows:

$$P = -(\vec{T}\vec{V} + \tfrac{1}{2}\vec{T}\vec{v}_u). \tag{A.6}$$

For the case of actual flight, Eq. A.6 can be rewritten in nonvectorial notations:

$$P = TV\cos\gamma_{fp} + \tfrac{1}{2}T v_u. \tag{A.7}$$

A.1 Induced Velocity and Thrust in Axial Translation

A.1.1 Vertical Climb and Hovering

Axial translation in climb can obviously be either in the thrust'direction as in vertical climb of a rotorcraft, or in the opposite direction as in vertical descent. In the first case let us consider a rotor or propeller moving in the thrust direction (climbing) at a constant velocity V_c, while developing thrust T. Here, an equivalent motion is substituted when the thrust generator remains stationary while the air flows past it in the axial direction (far from the rotor) at a speed of $-V_c$ (Fig. A.2)

Similar to the simple model, a single axis coordinate system is selected with its positive direction coinciding with that of the thrust T. Air particles approaching the actuator disc acquire some additional velocity that reaches a $-v_c$ value at the disc itself.

After passing through the disc, the speed of flow increases still further until, far downstream, the induced velocity reaches its ultimate value of $-v_u$ while the resultant velocity of flow becomes $V_u = -V_c - v_u$, and pressure returns to that of the surrounding air; i.e., it becomes p_o. Remembering that the mass flow within the streamtube is constant, its shape will probably resemble that shown in Fig. A.2.

On the other hand, according to Eq. A.2, the total thrust T can be expressed in this case as

$$T = \pi R^2 \rho (V_c + v_c) v_u. \tag{A.8}$$

In this case, $v_u = 2v_c$; so, substitution of this new value of v_u into Eq. A.8 results in

$$T = 2\pi R^2 \rho (V_c + v_c) v_c, \tag{A.9}$$

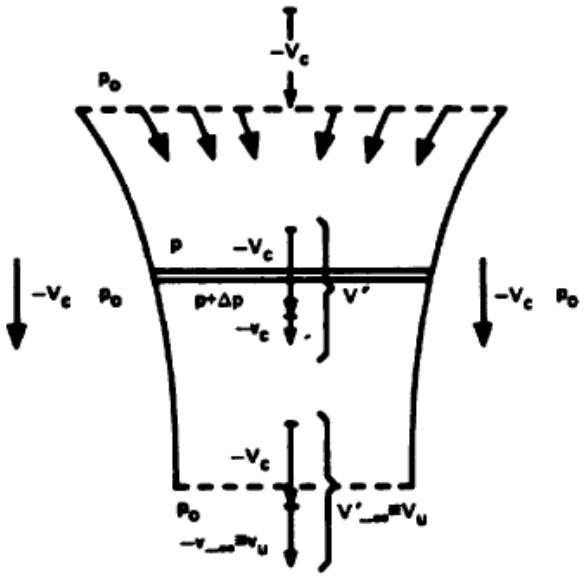

Figure A.2: Scheme of flow corresponding to vertical climb (Stepniewski, 1979).

or denoting the total thrust generating area of any actuator disc-like device as A, Eq A.9 may be rewritten more generally as

$$T = 2A\rho(V_c + v_c)v_c. \tag{A.10}$$

Eq. A.10 can be solved for v_c, thus obtaining an expression for induced velocity at the disc

$$v_c = -\frac{V_c}{2} + \sqrt{\frac{V_c^2}{4} + \frac{T}{2A\rho}}. \tag{A.11}$$

Remembering that $T/A \equiv w$ is the disc loading or, in more general terms, the thrust area loading, it can be rewritten as follows:

$$v_c = -\frac{V_c}{2} + \sqrt{\frac{V_c^2}{4} + \frac{w}{2\rho}} \tag{A.12}$$

In hover or under any static conditions at a speed $V_c = 0$;

$$T = 2A\rho v_h^2, \tag{A.13}$$

while the induced velocity (v_h) becomes

$$v_h = \sqrt{\frac{w}{2\rho}}. \tag{A.14}$$

Eq. A.11 can then be written as follow:

$$v_c = -\frac{V_c}{2} + \sqrt{\frac{V_c^2}{4} + v_h^2}. \tag{A.15}$$

A.1.2 Vertical Descent

Eq. A.11 which establish relationships between thrust and induced velocity in vertical climb can be modified for vertical descent. This can be simply done by changing the sign of V_c However, in order to clearly indicate that the considered case now refers to vertical descent, the symbol $V_\mathrm{d} \equiv -V_c$ is used, while the corresponding induced velocity will be symbolized as v_d. Thus,

$$v_\mathrm{d} = \frac{V_\mathrm{d}}{2} + \sqrt{\frac{V_\mathrm{d}^2}{4} + v_h^2}. \tag{A.16}$$

A.2 Power in Axial Translation

A.2.1 Ideal Power in Climb and Hovering

As in the case of the simplest thrust generator model, power required by the actuator disc either for climb or hover may again be called the ideal power. This is justified by the

previously made assumptions that (a) there are no friction or form drag losses, (b) the whole disc up to the limit of its geometric dimensions is participating in thrust generation, and (c) the downwash velocity is uniform at any slipstream cross-section.

Expressions for the ideal power in vertical climb (P_{id_c}) can readily be obtained from the relationship previously established in Eq. A.7. When a proper value of the fully developed downwash velocity ($v_u = 2v_c$) and $\cos\gamma_{fp} = 1.0$ are introduced into Eq. A.7), then P_{id_c} becomes

$$P_{\mathrm{id}_c} = T \cdot (V_c + v_c). \tag{A.17}$$

In the case of a steady vertical ascent with no download when $T = W$ (W being the weight of the aircraft in Newton or pounds), the total ideal power needed to climb is equal to the power required to overcome gravity ($W \cdot V_c$) plus the ideal induced power ($W \cdot v_c$).

By substituting the expression for v_c from Eq. A.11 into Eq. A.17, the following explicit relationship between P_{id_c} required and rate of climb V_c (for $T = W$) is obtained:

$$P_{\mathrm{id}_c} = W \cdot \left(\frac{V_c}{2} + \sqrt{\frac{V_c^2}{4} + v_h^2} \right). \tag{A.18}$$

In hovering $Vc = 0$:

$$P_{\mathrm{id}_h} = W \cdot v_h \tag{A.19}$$

$$P_{\mathrm{id}_h} = W \cdot \sqrt{\frac{W}{2A\rho}} \tag{A.20}$$

$$P_{\mathrm{id}_h} = \frac{W^{3/2}}{\sqrt{2A\rho}} \tag{A.21}$$

A.2.2 Ideal Power in Descent

For the $|V_\mathrm{d}/v_\mathrm{d}| < 1.0$ case; namely, at low descent speeds, the general flow is still down and, according to the previously developed rules, the ideal power required for this process- according to Eq. A.7 with $\vec{T}\vec{V}_\mathrm{d}$ being negative, will be as follows:

$$P_{\mathrm{id}_\mathrm{d}} = T \cdot (v_\mathrm{d} - V_\mathrm{d}) \tag{A.22}$$

Substituting the v_d value from Eq. A.16 into Eq. A.22, relationships similar to those given by Eq. A.18 can be obtained:

$$P_{\mathrm{id}_\mathrm{d}} = W \cdot \left(\frac{-V_\mathrm{d}}{2} + \sqrt{\frac{V_\mathrm{d}^2}{4} + v_h^2} \right) \tag{A.23}$$

A.3 Induced Velocity and Thrust in Nonaxial Translation

In nonaxial translation, the resultant speed of flow through the disc should always be interpreted as the vectorial sum of the distant flow velocity ($-\vec{V}_f$) and induced velocity in forward flight ($\vec{v}_f$). Denoting the scalar value of the resultant speed of flow at the disc by V', Eq. A.9, giving thrust in axial translation, can now be generalized into the following expression by substituting V' for $|\vec{V}_f + \vec{v}_f|$:

$$T = 2\pi R^2 \rho V' v_f \tag{A.24}$$

Analogous with Eq. A.9, it is postulated that far downstream, the induced velocity v_f is doubled; i.e., $v_u = 2v_f$. In making this assumption,$\pi R^2 \rho V'$ becomes the mass flow through the streamtube (affected by action of the rotor), whose cross-section is πR^2. The induced velocity in forward flight can readily be expressed as

$$v_f = \frac{T}{2\pi R^2 \rho V'} \tag{A.25}$$

It should be noted, however, that the above expression in its present form does not permit determination of the v_f value since V' is also dependent on v_f ($\vec{V}' = \vec{V}_f + \vec{v}_f$). In order to solve Eq. A.24 for v_f, V' must be first expressed in terms of V_f and v_f. With the same notations as those in Fig. A.3, V' becomes:

$$V' = \sqrt{(v_f - V_f \sin a)^2 + (V_f \cos a)^2} \tag{A.26}$$

Substituting the above value into Eq. A.24 and performing the necessary manipulation-

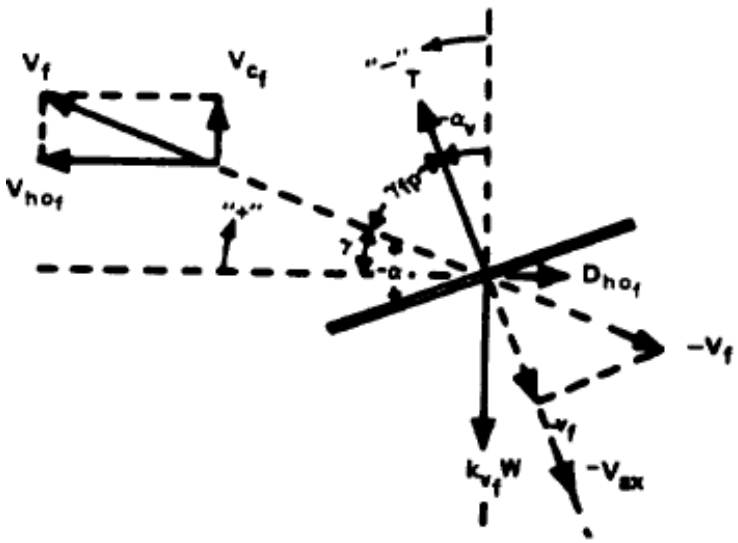

Figure A.3: Rotary-wing aircraft in forward flight (Stepniewski, 1979).

remembering that $T/\pi R \equiv w$ is the disc loading-the following fourth-degree equation for v_f is obtained:

$$v_f^4 - 2V_f v_f^3 \sin a + V_f^2 v_f^2 - (w/2\rho)^2 = 0. \tag{A.27}$$

When $a = 0$, Eq. A.27 is reduced to a biquadratic form and the solution for v_f; can also be easily obtained:

$$(v_f)_{a=0} = \sqrt{-\frac{V_f^2}{2} + \sqrt{\frac{V_f^4}{4} + \left(\frac{W}{2\rho A}\right)^2}} \tag{A.28}$$

A.4 Power in Nonaxial Translation

Using the notations in Fig. A.3, and substituting the proper quantities for $\vec{T}\vec{V}$ and $\frac{1}{2}\vec{T}\vec{v}_u$ into Eq. A.6, the ideal power required in nonaxial translation P_{id_f} (forward flight) for a helicopter moving in the gravitational coordinate system at velocity of flight V_f, can be obtained:

$$P_{\mathrm{id}_f} = -T(V_f \cos\gamma_{fp} - v_f) \tag{A.29}$$

However, $\gamma_{fp} = 90^\circ - (\gamma + a_v)$, and Eq. A.29 can be presented in the following form:

$$P_{\mathrm{id}_f} = (V_f \sin\gamma)(T\cos a_v) + (V_f \cos\gamma)(T \sin a_v) + Tv_f. \tag{A.30}$$

It should be realized that

$$V_f \sin\gamma \equiv V_{cf} \qquad \text{rate of climb in forward flight} \tag{A.31}$$

$$V_f \cos\gamma \equiv V_{ho} \qquad \text{horizontal component of the speed of flight} \tag{A.32}$$

and in steady-state flight:

$$T\cos a_v = k_{vf}W \qquad \text{vertical thrust component} \tag{A.33}$$

$$T\sin a_v = D_{ho} \qquad \text{horizontal thrust component} \tag{A.34}$$

Taking the above relationships into consideration, the idea] power required in forward flight can be expressed as follows:

$$P_{\mathrm{id}_f} = V_{ho}D_{ho} + V_{cf}k_{vf}W + Tv_f \tag{A.35}$$

For those cases when $k_{vf} \approx 1.0$ and D_{ho}/W are considered small, it may be assumed that $T \approx W$, and Eq. A.35 may be written as follows:

$$P_{\mathrm{id}_f} = W[(D_{ho}/W)V_{ho} + V_{cf} + v_{ho}] \tag{A.36}$$

Appendix B

Causes of Battery Degradation and Failures

There are a number of ways to exceed the thermal stability limits of a lithium-ion cell and cause an energetic failure. Energetic lithium-ion battery failures may be induced by external forces such as exposure to fire or severe mechanical damage, or they may be the result of problems involving charge, discharge, and/or battery protection circuitry design and implementation, or they may be caused by internal cell faults that result from rare and/or subtle manufacturing problems. Generally, the root causes of energetic cell and battery failures can be classified into (Mikolajczak et al., 2011):

B.1 Electrical Abuse

B.1.1 Overcharge

Overcharge of a lithium-ion cell can cause significant degradation of both anode and cathode. On the anode, overcharge can cause plating rather than intercalation of lithium. Plated lithium forms dendrites that can grow over time and then cause internal shorting. Plated lithium also interacts exothermically with electrolyte. On the cathode, overcharge can cause excess removal of lithium from cathode material structures, such that their crystalline structure becomes unstable, resulting in an exothermic reaction. Reactions at both the anode and cathode, as well as lithium dendrite shorting can push a cell out of its thermal stability limits and result in a thermal runaway reaction. The more severe the degree of overcharge, the more likely the cell is to experience thermal runaway.

There are a few ways in which overcharge can occur. The most obvious overcharge mode is charging a cell to too high of a voltage (over voltage overcharge). For example, charging a 4.2V rated cell above 5V will likely cause an immediate, energetic failure. Charging at excessive currents, but not excessive voltages, can also cause an overcharge failure; in this case, localized regions of high current density within a cell will become overcharged, while

other regions within the cell will remain within appropriate voltage limits.

B.1.2 Over-Discharge

Simply over-discharging a lithium-ion cell to 0V will not cause a thermal runaway reaction. However, such over-discharge can cause internal damage to electrodes and current collectors (i.e., dissolution of copper), can lead to lithium plating if the cell is recharged (particularly, if the cell is repeatedly over-discharged), and can ultimately result in thermal runaway.

Most consumer electronics devices set specific discharge voltage limits for their lithium-ion battery packs, at which point an electrical switch will disconnect the electrical load from the battery pack to prevent over-discharge. However, such a mechanism cannot completely prevent over-discharge. For example, a battery pack may be discharged to the low voltage cutoff and then stored for an extended period of time during which self-discharge of the cell ultimately results in over-discharge.

B.1.3 External Short Circuit

High rate discharging (or charging) can cause resistive heating within cells at points of high impedance. Such internal heating could cause cells to exceed thermal stability limits. Points of high impedance could include weld points within a cell (internal tab attachment) or electrode surfaces. As cell size and capacity increases, the likelihood of internal impedance heating leading to thermal runaway also increases. Larger cells exhibit slower heat transfer to their exteriors, and they usually have higher capacities. Thus, they have the potential to convert more electrical energy to internal heat. Investigation of a number of thermal runaway failures that have occurred during transport has revealed that improper packaging, particularly a failure to prevent short circuits is a common cause of these incidents.

B.2 Thermal Abuse

The most direct way to exceed the thermal stability limits of a lithium-ion cell is to subject it to external heating. Very few energetic field failures of consumer electronic devices have been attributed to long-term storage of cells at temperatures just above the self-heating point of 70 to 90C (158 to 194F). Such failures require not only elevated temperature, but an adiabatic (highly insulated) environment, and extended times to reach a self-sustaining thermal runaway condition. Although possible, these sorts of conditions are seldom achieved with consumer electronic devices in the field. Failure via this mode may also occur under certain extreme storage scenarios. Some examples might include lithium-ion batteries stored on high racks in non-climate controlled warehouses during summer months, or lithium-ion batteries stored adjacent to heaters.

B.3 Mechanical Abuse

Mechanical abuse of cells can cause shorting between cell electrodes, leading to localized cell heating that propagates to the entire cell and initiates thermal runaway. The mechanical abuse can be severe and result in immediate failure, or it can be subtle, and create a flaw in the cell that results in an internal cell fault much later (i.e., after the cell has undergone numerous cycles). Mechanical damage (crush or penetration) that occurs at electrode edges is significantly more likely to cause cell thermal runaway than damage perpendicular to electrode surfaces.

Appendix C

Dissemination of the Results

C.1 Journal and Conference Papers

1. Sierra, G., Orchard, M., Goebel, K., & Kulkarni, C. "Battery Health Management for Small-size Rotary-wing Electric Unmanned Aerial Vehicles: An Efficient Approach for Constrained Computing Platforms", Reliability Engineering & System Safety, Accepted for publication.
    - This paper was highlighted in the May 2018 battery engineering literature review and featured in the '10 Ionizing Papers for May' blog of Research Interfaces.
2. Sierra, G., Orchard, M., Goebel, K., & Kulkarni, C."A Hybrid Battery Model for Prognostics in Small-size Electric UAVs", Annual Conference of Prognostics and Health Management Society, PHM Society, 2018, Accepted for publication.
3. Sierra, G., Acuña, D.,Orchard, M., Goebel, K., & Kulkarni, C. "Exploring Probability Mass Function in Battery Prognostics for Electric UAVs", Expert Systems with Applications, In preparation for submission.

C.2 Presentations at Symposiums

1. This thesis was one of the 10 selected globally by the Prognostics and Health Management Society (PHM Society) to participate in the Doctoral Symposium of The Annual Conference of the PHM Society 2016 (PHM16); the most important conference associated with the PHM discipline.

C.3 Doctoral Internships

1. Visiting Scientist, Prognostics Center of Excellence (PCoE), NASA Ames Research Center, San Francisco Bay Area, CA. September 2017 to December 2017.
2. Doctoral intern, Reliability Team, Prime Air, Amazon Corporate LLC, Seattle, WA. June 2017 to August 2017.

Bibliography

3DR (2013). Announcing iris, a totally ready-to-fly uav quadcopter with our next-gen autopilot. https://3dr.com/blog/announcing-iris-a-totally-ready-to-fly-uav-quadcopter-with-our-next-gen-autopilot-53ac9d20558d/.

Acuña, D. and Orchard, M. (2018). A theoretically rigorous approach to failure prognosis. In *Annual Conference of Prognostics and Health Management Society*. PHM Society.

Acuña, D. E. and Orchard, M. E. (2017). Particle-filtering-based failure prognosis via sigma-points: Application to lithium-ion battery state-of-charge monitoring. *Mechanical Systems and Signal Processing*, 85:827 – 848.

Amazon, Inc (2015). Amazon prime air. https://www.amazon.com/b?ie=UTF8&node=8037720011.

Asari, V. K., editor (2014). *Wide Area Surveillance:Real-time Motion Detection Systems*, volume 6. Springer Berlin Heidelberg.

Banerjee, A. and Roychoudhury, A. (2017). Future of mobile software for smartphones and drones: Energy and performance. In *2017 IEEE/ACM 4th International Conference on Mobile Software Engineering and Systems (MOBILESoft)*, pages 1–12.

Barbarisi, O., Vasca, F., and Glielmo, L. (2006). State of charge kalman filter estimator for automotive batteries. *Control Engineering Practice*, 14(3):267 – 275. Advances in Automotive Control (AC'04)Advances in Automotive Control (AC'04).

Bole, B., Daigle, M., and Gorospe, G. (2014a). Online prediction of battery discharge and estimation of parasitic loads for an electric aircraft. In *Annual Conference of the Prognostics and Health Management Society 2014*.

Bole, B., Teubert, C., Chi, Q. C., Edward, H., Vazquez, S., Goebel, K., and George, V. (2014b). SIL/HIL replication of electric aircraft powertrain dynamics and inner-loop control for V&V of system health management routines. In *Annual Conference of the Prognostics and Health Management Society 2014*.

Bouabdallah, S. (2007). *Design and Control of Quadrotors with Application to Autonomous Flying*. PhD thesis, École Polytechnique Fédérale de Lausanne.

Bundy, K., Karlsson, M., Lindbergh, G., and Lundqvist, A. (1998). An electrochemical

impedance spectroscopy method for prediction of the state of charge of a nickel-metal hydride battery at open circuit and during discharge. *Journal of Power Sources*, 72(2):118 – 125.

Burgos-Mellado, C., Orchard, M. E., Kazerani, M., Cárdenas, R., and Sáez, D. (2016). Particle-filtering-based estimation of maximum available power state in lithium-ion batteries. *Applied Energy*, 161:349 – 363.

Candy, J. V. (2009). *Bayesian Signal Processing: Classica, Modern, and Particle Filtering Methods*. John Wiley & Sons, Inc., 1 edition.

Cessford, J. and Barwood, M. (2015). The effects of hot and cold environments on drone component performance and drone pilot performance. Report 2, Northumbria University, United Kingdom.

Chang, W. (2012). State of charge estimation for lifepo4 battery using artificial neural network. *International Review of Electrical Engineering*, 7(5):5874–5880.

Chang, W.-Y. (2013). The state of charge estimating methods for battery: A review. *ISRN Applied Mathematics*, 2013.

Charkhgard, M. and Farrokhi, M. (2010). State-of-charge estimation for lithium-ion batteries using neural networks and ekf. *IEEE Transactions on Industrial Electronics*, 57(12):4178–4187.

Cisco Systems, Inc (2014). Congestion avoidance overview, cisco IOS quality of service solutions configuration guide. http://www.cisco.com/c/en/us/td/docs/ios/12_2/qos/configuration/guide/fqos_c/qcfconav.html.

Cuong, Q., Bole, B., Hogge, E., Vazquez, S., Daigle, M., Celaya, J., Weber, A., and Goebel, K. (2013). Battery charge depletion prediction on an electric aircraft. In *Annual Conference of the Prognostics and Health Management Society 2013*.

Daigle, M. (2016a). Prognostics algorithm library [computer software]. https://github.com/nasa/PrognosticsAlgorithmLibrary.

Daigle, M. (2016b). Prognostics model library [computer software]. https://github.com/nasa/PrognosticsModelLibrary.

Daigle, M. and Kulkarni, C. (2013). Electrochemistry-based battery modeling for prognostics. In *2009 International Conference on Prognostics and Health Management*.

Daigle, M. J. and Goebel, K. (2013). Model-based prognostics with concurrent damage progression processes. *IEEE Transactions on Systems, Man, and Cybernetics: Systems*, 43(3):535–546.

Dalamagkidis, K. (2015). *Handbook of Unmanned Aerial Vehicles*, chapter Definitions and Terminology, pages 43–55. Springer Netherlands.

de Souza Candido, A., Kawakami Harrop Galvao, R., and Yoneyama, T. (2014). Control and energy management for quadrotor. In *Control (CONTROL), 2014 UKACC International Conference on*, pages 343–348.

Diaz, T. (2015). Lights, drone... action. *Spectrum, IEEE*, 52(7):36–41.

DJI (2016). Phantom 3 professional. http://www.dji.com/product/phantom-3-pro/info.

Editec, G. E. (2015). Gobierno endurece la lucha contra el robo de agua e incorpora drones. http://www.sustentare.cl/2015/12/09/gobierno-endurece-la-lucha-contra-el-robo-de-agua-e-incorpora-drones/.

EFE (2015). Chile presenta primera normativa para uso civil de drones en latinoamérica. http://www.latercera.com/noticia/tendencias/2015/04/659-624901-9-chile-presenta-primera-normativa-para-uso-civil-de-drones-en-latinoamerica.shtml.

Elsen, C. (2014). 3dr iris with 4s batteries. https://www.cloud-surfer.net/2014/07/14/3dr-iris-with-4s-batteries/.

Engel, S. J., Gilmartin, B. J., Bongort, K., and Hess, A. (2000). Prognostics, the real issues involved with predicting life remaining. In *2000 IEEE Aerospace Conference. Proceedings (Cat. No.00TH8484)*, volume 6, pages 457–469 vol.6.

Fearnhead, P. (2008). Computational methods for complex stochastic systems: A review of some alternatives to mcmc. *tatistics and Computing*, 18(2):151–171. ISSN 0960-3174.

Federal Aviation Administration (2013). *Helicopter Flying Handbook*, chapter Helicopter Performance. Skyhorse Publishing.

Gao, L., Liu, S., and Dougal, R. (2002). Dynamic lithium-ion battery model for system simulation. *Components and Packaging Technologies, IEEE Transactions on*, 25(3):495–505.

Gatti, M., Giulietti, F., and Turci, M. (2015). Maximum endurance for battery-powered rotary-wing aircraft. *Aerospace Science and Technology*, 45:174 – 179.

Goebel, K., Saha, B., Saxena, A., Celaya, J., and Christophersen, J. (2008). Prognostics in battery health management. *Instrumentation Measurement Magazine, IEEE*, 11(4):33–40.

Habis, C. (2015). Weather considerations for drones. http://www.motion-iq.com/blog-1/2015/11/29/weather-considerations-for-drones.

Hartmann, R. (2008). *An Aging Model for Lithium-ion Cells*. PhD thesis, The University of Akron.

Hogge, E. F., Bole, B. M., Vazquez, S. L., Celaya, J. R., Strom, T. H., Hill, B. L., Smalling, K. M., and Quach, C. C. (2015). Verification of a remaining flying time prediction system for small electric aircraft. In *Annual Conference of the Prognostics and Health Management*

Society 2013.

Hu, C., Youn, B. D., and Chung, J. (2012). A multiscale framework with extended kalman filter for lithium-ion battery {SOC} and capacity estimation. *Applied Energy*, 92:694 – 704.

Lee, S., Kim, J., Lee, J., and Cho, B. (2008). State-of-charge and capacity estimation of lithium-ion battery using a new open-circuit voltage versus state-of-charge. *Journal of Power Sources*, 185(2):1367 – 1373.

Liu, J. and West, M. (2001). *Sequential Monte Carlo Methods in Practice*, chapter Combined Parameter and State Estimation in Simulation-Based Filtering, pages 197–223. Springer New York.

Marcos E. Orchard, Felipe A. Tobar, G. J. V. (2009). Outer feedback correction loops in particle filtering-based prognostic algorithms: Statistical performance comparison. *Studies in Informatics and Control*, 18(4):295–304.

Martinez, C. (2015). El nuevo dron de DJI busca granjero geek. http://es.engadget.com/2015/11/27/dron-dji-busca-granjero-geek/.

Meyer, J., du Plessis, F., and Clarke, W. (2009). *Aerial Vehicles*, chapter Design Considerations for Long Endurance Unmanned Aerial Vehicles, pages 443–497. InTech, Chapters published, University Johannesburg, South Africa.

Mikolajczak, C., Kahn, M., White, K., and Long, R. T. (2011). Lithium-ion batteries hazard and use assessment. Technical report, The Fire Protection Research Foundation.

Mueller, M. (2016). Calculador de multicopteros. http://www.ecalc.ch/xcoptercalc.php?ecalc&lang=es.

Ng, K. S., Moo, C. S., Chen, Y.-P., and Hsieh, Y. C. (2008). State-of-charge estimation for lead-acid batteries based on dynamic open-circuit voltage. In *Power and Energy Conference, 2008. PECon 2008. IEEE 2nd International*, pages 972–976.

Ng, K. S., Moo, C.-S., Chen, Y.-P., and Hsieh, Y.-C. (2009). Enhanced coulomb counting method for estimating state-of-charge and state-of-health of lithium-ion batteries. *Applied Energy*, 86(9):1506 – 1511.

Orchard, M. E. and Vachtsevanos, G. J. (2009). A particle-filtering approach for on-line fault diagnosis and failure prognosis. *Transactions of the Institute of Measurement and Control*, 31(3/4):221–246.

Pola, D. (2014). An improved prognosis strategy with temperature dependent state-space model for the analysis of the state-of-health and state-of-charge in lithium-ion batteries. Master thesis, University of Chile, Santiago, Chile.

Pola, D., Navarrete, H., Orchard, M., Rabie, R., Cerda, M., Olivares, B., Silva, J., Espinoza, P., and Perez, A. (2015). Particle-filtering-based discharge time prognosis for lithium-ion

batteries with a statistical characterization of use profiles. *Reliability, IEEE Transactions on*, 64(2):710–720.

Quadcopter Flight School (2014). Power efficiency hover vs. forward flight. http://quadcopter101.blogspot.cl/2014/02/flight-school-5-power-efficiency-hover.html.

Ran, L., Junfeng, W., Haiying, W., and Gechen, L. (2010). Prediction of state of charge of lithium-ion rechargeable battery with electrochemical impedance spectroscopy theory. In *2010 5th IEEE Conference on Industrial Electronics and Applications*, pages 684–688.

Saha, B., Goebel, K., Poll, S., and Christophersen, J. (2009). Prognostics methods for battery health monitoring using a bayesian framework. *Instrumentation and Measurement, IEEE Transactions on*, 58(2):291–296.

Saha, B., Koshimoto, E., Quach, C., Hogge, E., Strom, T., Hill, B., Vazquez, S., and Goebel, K. (2011a). Battery health management system for electric UAVs. In *Aerospace Conference, 2011 IEEE*, pages 1–9.

Saha, B., Quach, C., and Goebel, K. (2012). Optimizing battery life for electric UAVs using a bayesian framework. In *Aerospace Conference, 2012 IEEE*, pages 1–7.

Saha, B., Quach, P., and Goebel, K. (2011b). Exploring the model design space for battery health management. In *Proceedings of the Annual Conference of the Prognostics and Health Management Society*, Montreal, Canada.

Salkind, A. J., Fennie, C., Singh, P., Atwater, T., and Reisner, D. E. (1999). Determination of state-of-charge and state-of-health of batteries by fuzzy logic methodology. *Journal of Power Sources*, 80(1-2):293 – 300.

Santhanagopalan, S., Zhang, Q., Kumaresan, K., and White, R. E. (2008). Parameter estimation and life modeling of lithium-ion cells. *Journal of The Electrochemical Society*, 155(4):A345–A353.

Saxena, A., Celaya, J., Balaban, E., Goebel, K., Saha, B., Saha, S., and Schwabacher, M. (2008). Metrics for evaluating performance of prognostic techniques. In *2008 International Conference on Prognostics and Health Management*, pages 1–17.

Saxena, A., Celaya, J., Saha, B., Saha, S., and Goebel, K. (2009). On applying the prognostic performance metrics. In *2009 International Conference on Prognostics and Health Management*.

Saxena, A., Celaya, J. R., Roychoudhury, I., Saha, S., Saha, B., and Goebel, K. (2012). Designing data-driven battery prognostic approaches for variable loading profiles: Some lessons learned. In *European Conference of Prognostics and Health Management Society*. PHM Society.

Sebbane, Y. B. (2014). *Planning and Decision Making for Aerial Robots*, volume 71 of *Intelligent Systems, Control and Automation: Science and Engineering*. Springer International Publishing.

Singh, P., Vinjamuri, R., Wang, X., and Reisner, D. (2006). Design and implementation of a fuzzy logic-based state-of-charge meter for li-ion batteries used in portable defibrillators. *Journal of Power Sources*, 162(2):829 – 836. Special issue including selected papers from the International Power Sources Symposium 2005 together with regular papers.

Stelter, B. (2015). New amazon drone video, brought to you by jeremy clarkson. http://money.cnn.com/2015/11/29/media/amazon-drone-video-prime-air/index.html.

Stepniewski, W. Z. (1979). *Rotary-wing Aerodynamics. Volume I: Basic Theories of Rotor Aerodynamics with Application to Helicopters*, volume I, chapter Momentum Theory, pages 44–90. National Aeronautics and Space Administration NASA, Scientific and Technical Information Office, Washington, United States.

Sun, F., Hu, X., Zou, Y., and Li, S. (2011). Adaptive unscented kalman filtering for state of charge estimation of a lithium-ion battery for electric vehicles. *Energy*, 36(5):3531 – 3540.

Tampier, C., Pérez, A., Jaramillo, F., Quintero, V., Orchard, M., and Silva, J. (2015). Lithium-ion battery end-of-discharge time estimation and prognosis based on bayesian algorithms and outer feedback correction loops: A comparative analysis. In *Annual Conference of Prognostics and Health Management Society*. PHM Society.

Valavanis, K. P. and Vachtsevanos, G. J., editors (2015a). *Handbook of Unmanned Aerial Vehicles*. Springer Netherlands, 1 edition.

Valavanis, K. P. and Vachtsevanos, G. J. (2015b). *Handbook of Unmanned Aerial Vehicles*, chapter UAV Applications: Introduction, pages 2639–2641. Springer Netherlands.

Walker, E., Rayman, S., and White, R. E. (2015). Comparison of a particle filter and other state estimation methods for prognostics of lithium-ion batteries. *Journal of Power Sources*, 287:1 – 12.

Wang, C.-Y., Zhang, G., Ge, S., Xu, T., Ji, Y., Yang, X.-G., and Leng, Y. (2016). Lithium-ion battery structure that self-heats at low temperatures. *Nature - International Weekly Journal of Science*, 529(7587):515–518.

Weigert, T., Tian, Q., and Lian, K. (2011). State-of-charge prediction of batteries and battery-supercapacitor hybrids using artificial neural networks. *Journal of Power Sources*, 196(8):4061 – 4066.

Zang, M., Xie, J., Ouyang, J., Wang, S., and Wu, X. (2014). Investigation of temperature performance of lithium-ion batteries for electric vehicles. In *Transportation Electrification Asia-Pacific (ITEC Asia-Pacific), 2014 IEEE Conference and Expo*, pages 1–8.

Zhang, J. and Xia, C. (2011). State-of-charge estimation of valve regulated lead acid battery based on multi-state unscented kalman filter. *International Journal of Electrical Power & Energy Systems*, 33(3):472 – 476.

Zhu, G., Wen, K., Lv, W., Zhou, X., Liang, Y., Yang, F., Chen, Z., Zou, M., Li, J., Zhang, Y., and He, W. (2015). Materials insights into low-temperature performances of lithium-ion

batteries. *Journal of Power Sources*, 300:29 – 40.